ANALYSIS OF ELASTIC AND VISCOELASTIC SMART FLEXIBLE AND FOLDABLE SYSTEMS

A Dissertation

by

VAHID TAJEDDINI

Submitted to the Office of Graduate and Professional Studies of
Texas A&M University
in partial fulfillment of the requirements for the degree of

DOCTOR OF PHILOSOPHY

Committee Chair,	Anastasia H. Muliana
Committee Members,	Sevan Gonezen
	Stefan Hurlebaus
	Miladin Radovic
Head of Department,	Andreas A. Polycarpou

August 2016

Major Subject: Mechanical Engineering

ABSTRACT

Smart or adaptive structures that use multifunctional materials to control the response of a structure have been of considerable interest in recent years. Some examples are foldable and flexible structures that can be actuated by non-mechanical stimuli (thermal, electrical, magnetic, solvent, light, etc.). This study presents analyses of smart flexible and foldable structures, such as slender beams and thin plates/shells integrated with distributed polarized piezoelectric patches. The studied smart flexible and foldable structures are undergoing large rotations and relatively small strains that are triggered by electro-mechanical actuations. The electric actuation is done by stimulating the bonded patches with electric voltages, while the mechanical actuation is in the form of prescribed external surface- and/or body forces. Both elastic and viscoelastic material responses are considered for the foldable and flexible host structures. For the behavior of piezoelectric material, a nonlinear electro-mechanical constitutive equation is taken into account to incorporate large electric field inputs. Two types of piezoelectric patches are considered, namely piezoelectric wafer and active fiber composites. The governing equation of the Reissner's beam theory is first adopted in order to describe the large deformations of the flexible and foldable systems, and modified for the electro-active beams to derive analytical solutions. This study is then extended to 3-D deformation of plates and shells with considering bending and membrane stiffness subjected to large rotation and displacements. Co-rotational finite element method is used to numerically solve the governing equation of the smart flexible plates. Simulations of various shape changes in smart flexible and foldable systems are presented and parametric studies are also conducted in order to examine the effects of material and geometrical parameters on the overall performance of smart systems.

TABLE OF CONTENTS

Page

LIST OF FIGURES

Page

LIST OF TABLES

Page

1. INTRODUCTION

1-1 Literature review

Recent development of smart or adaptive foldable (flexible) structures allows for controllable reconfiguration into various shapes, which have many engineering applications, e.g. artificial skins, morphing aircraft, flexible robots for use in hazardous environments, deployable space structures, etc. Various designs of compliant mechanisms have been developed for flexible wings, i.e., tensegrity structures [1, 2], corrugated composite systems [3], or using compliant cellular trusses underneath the wing' panels [4]. Limited designs have also been considered for compliant structures activated with non-mechanical actuators such as piezoelectric, soft electro-active materials, and shape memory actuators [5]. Another type of compliant structures is in the form of a thin polymeric sheet whose microstructure comprises of arrangements of active materials [6-8]. One of widely used active flexible polymeric systems comprises of piezoelectric ceramics dispersed in homogeneous polymeric thin plates, termed as electro-active composites, which form lightweight flexible (compliant) active materials, allowing for large bending and twisting deformation while maintaining small strains. The use of piezoceramics based materials has an advantage, for actuator applications, where a relatively low voltage is possible to achieve certain deformations, but the brittle nature of ceramics limits the deformations. Integrating piezoceramics with softer materials, such as polymers, allows for generating compliant and flexible systems that can be actuated by electric field inputs. Typical compliant systems are in the forms of slender/thin structures where high aspect ratios are shown in their dimensions (rod, filament, and sheet). When subjected to external stimuli, compliant systems generally experience large deformations. Depending on the geometrical shapes and materials considered, compliant systems can experience relatively small strains while undergoing large rotations [9, 10]. This study considers electro-active flexible/foldable structures in the forms of slender beams and thin plates/shells having piezoelectric materials (ceramics or polymers) as active components and polymeric substrates. When piezoceramics is being used, the existence of piezoelectric

ceramics limits the strains in the flexible structures and large deformation in such structures are predominantly due to large rotations.

1-1-1 Large deformation analyses of structures

There have been analytical and numerical studies presented on simulating large deformations in flexible structures, such as slender beams, thin plates and shells, subjected to a mechanical stimulus. Most of these studies have considered elastic and homogeneous structures. The commonly used analytical methods for obtaining solutions to large deformations of elastic beams include power series, equivalent systems [11], e.g., pseudo-linear systems, which solve the nonlinear problems by transforming the equations into a set of linear equations, and elliptical integrals [12, 13], while the numerical approaches include Runge-Kutta, shooting method and finite element analyses, see Tada and Lee [14], Yang [15] and Chajes [16]. In the analysis of slender beams undergoing large deformations, the slope of the deflected middle axis cannot be neglected in determining the curvature of the deformed beam. Reissner [17] formulated the governing equations for large in-plane displacements and finite strains of elastic beams subjected to mechanical loadings. Later, Irschik and Gerstmayr [18] derived the Reissner's governing equations for originally straight beams based on continuum mechanics. The governing equations are expressed in the Lagrangian configuration and results in a system of nonlinear differential equations, which can be solved numerically or analytically depending on the prescribed boundary conditions.

Limited studies have been done on analyzing nonlinear deformations of smart beams, rods, plates and shells. Lagoudas and co-authors [19-21] studied the deformations of flexible rods with embedded shape memory alloys by using shear-lag model in order to approximate the axial forces and moments induced by the actuators. Banerjee et al. [22] presented nonlinear shooting and Adomain decomposition methods in order to obtain solutions to large deformations of cantilever beams under mechanical loadings, which can be extended to predict large deformations in cantilever beams with piezoelectric materials. Moderate and large deformation of plates are governed by coupled nonlinear differential equations for which analytical solutions are available only for very few cases involving simple geometries and loading conditions. Regarding smart plates, Chen and Chen [23] studied piezoelectric

layered-plates by adopting von Karman theory and using finite difference method in order to obtain solutions to the governing equations. Xue et al. [24] derived nonlinear partial differential equations for thin plates made of piezoemagnetic and piezoelectric materials under mechanical loads by considering von Karman theory. Jayakumar et al [25] also adopted von Karman strain displacement relations in studying large deformation of simply supported piezo-laminated composite beams under distributed transverse load. Von Karman theory considers up to quadratic terms in definition of strain components and neglects higher order terms and so is suitable for moderate deformations and strains including rotations and translations in slender beams. The governing equation in von-Karman theory is not suitable for problems involving folding or rolling of the thin/slender structures.

One of the commonly used numerical techniques to solve for large deformations of plates and shells is finite element method (FEM). For finite element (FE) analysis of structures, three Lagrangian kinematic descriptions have been developed: (a) total Lagrangian (TL), (b) updated Lagrangian and (c) co-rotational (CR). For the TL approach, the governing equations are written with respect to the original configuration of the body while for the UL method, the reference configuration is updated and for each step or increment, the equations are formulated with respect to equilibrated configuration from the previous step. The CR description is based on a separation of rigid body displacements from the deformational displacements. In the CR method, the deformational component is typically formed based on small strain measures, although other general strain measures are also possible. The governing equations are expressed with respect to the current configuration obtained from the rigid body motion of the original configuration. The limitation of the CR method is that the rigid body displacements and rotations can be large but the strains must remain relatively small, when the small strain measures are considered for the deformation part, while there is no such limitation for the TL and UL method.

The CR formulation was first introduced by Wempner [26] in 1969 and Belytschko et al. [27] in 1973. Fraeijs de Veubeke [28] developed a co-rotated dynamic frame attached to the flexible bodies to split their mean rigid body motions from the deformations and used Hamilton's principle for vibration analyses. The concept of co-rotated frame attached to the element allows for maintaining linear formulations for the deformation of the element, which was discussed by Bergan and Horrigmoe [29] and Argyris [30]. This concepts was developed

later by Rankin and Brogan [31] and Nour-Omid and Rankin [32] where they presented element independent CR formulation which was later improved by Nour-Omid and Rankin [32]. The formulation relies on using rotation projector to form the tangent stiffness directly from the CR formulation. Cardona [33] used the CR concept for analyzing mechanical deformations of components of flexible mechanisms. Crisfield developed the concept of consistent CR formulation in which the tangent stiffness formulation was written directly from the variation of the internal force [34-36] and presented the formulation for beam elements [34]. Felippa and Haugen [37] summarized the existing CR formulations, combined the invariant nature of Bergan et al. [29] formulation and the equilibrium and consistency of the formulation of Nour-Omid and Rankin, and presented a unified theoretical framework for co-rotational finite element (CRFE) in geometrically nonlinear analyses of structures. Cai et al. [38] used the CR formulation of plane elements with large rotations for analysis of slender plate structure under static loads leading to large rotations. Li et al. [39] developed a quadrilateral curved shell element by adding rotational nodal variables for co-rotational element formulation to derived an explicit expression of the element strain energy and verified reliability and computational efficiency of the element through modeling some curved shell structures under mechanical loadings.

Co-rotational finite element (CRFE) formulation allows the use of linear finite element approaches to capture the nonlinear deformations whereas large rigid body motions are treated separately and therefore it is computationally efficient. Recently, by using the CR formulation, triangular flat shell elements were constructed by researchers for nonlinear analysis of shells and plates subjected to small strains and large rotations due to mechanical loads [40-42]. Cai and Atluri [43, 44] considered also CRFE method for analyzing plates with moderate strains by adopting the von-Karman nonlinear strains in the rotated element frame. To the best of our knowledge, the CRFE method has not been used for studying deformations in smart flexible plates/shells actuated by non-mechanical stimuli.

1-1-2 Responses of piezoelectric ceramics and active fiber composites

Piezoelectric ceramics such as lead zirconate titanate (PZT) or barium titanate (BaTiO3) used are commonly used in actuator and sensor applications due to their relatively

large electro-mechanical coupling properties, compared to those of piezoelectric polymers such as polyvinlidene fluoride (PVDF). In order to actuate PVDF significantly large voltage is required as compared to the voltage required in piezoelectric ceramics. The crystal structures in piezoelectric ceramics possess electro-mechanical coupling effect due to electric polarization. The piezoelectric effects become noticeable once the piezoelectric materials have been polarized to align the dipoles in the crystalline. Thus, prior to using piezoelectric materials in applications, they are polarized by applying high electric field until saturation polarization is reached, which is typically done at high temperatures. In applications, piezo actuators are generally operated under electric field stimulus lower than the coercive field limit, which is the amount of electric field that cause reorientation of the dipoles in opposite of poling direction, in order to avoid depolarization.

In actuation applications, it is often necessary to apply high electric field inputs to the piezoelectric components in order to obtain large deformations. When subjected to high electric fields, the polarized piezoelectric materials often experience nonlinear electro-mechanical responses. Tiersten [45] was among researchers who studied nonlinear electro-mechanical behaviors of polarized piezoelectric ceramics. He formulated an electro-mechanical constitutive model by considering higher order terms of the electric field in order to describe the nonlinear electro-mechanical coupling behavior of piezoelectric ceramics (PZT-G) materials. A higher order electro-mechanical model can also be applied to other electro-active materials such as electrostrictive materials, where one can consider only even terms. A limited number of studies have considered nonlinear electro-mechanical response of piezoelectric materials due to large electric fields [46-48], but for small deformations. In the present study, higher order terms of the electric field are taken into account in the electro-mechanical constitutive relation of smart structures undergoing large deformations, mainly due to large rotations, but the strains remain small. The small strain limit is partly due to the use of piezoelectric ceramics based materials. In general, slender structures whose dimensions are not of comparable orders of magnitude can also experience relatively small strains while undergoing large rotations (or bending), see Naghdi and Vongsarnpigoon (1983) and Srinivsasa (2015).

Due to its brittle nature piezoelectric ceramics is not suitable for applications that involve large deformations. One solution to improve deformations that can be attained by

piezoelectric ceramics is to use it in shape of fibers embedded in a polymeric matrix. The assembly is called active fiber composites (AFC), which was originally proposed by Ben and Hagood [8]. AFCs, made from piezoelectric lead zirconate titanate (PZT) fibers and an epoxy matrix, were originally developed as actuators for adaptive materials systems (see an example of AFC on Figure 1) and to amplify deflection caused by piezoelectric effect. A schematic of AFC architecture is shown in Figure 2. PZT fibers are embedded in the epoxy matrix and are aligned along the longitudinal direction. The electric field is applied to PZT fiber through the aluminum electrode wires that are placed on the top and bottom of the fibers and aligned in the lateral direction perpendicular to the longitudinal direction of AFC fibers. Electrodes that are placed on the top and bottom in the thickness direction of the AFC patch have the same electric potential. Thus, the electric field on the central plane of the AFC is zero. Electrodes that are adjacent to each other in the longitudinal direction of the AFC have the opposite electric potentials. As a result, an electric field is formed in the longitudinal direction of fibers [49]. However, the electric field lines along the fibers are not distributed uniformly, where the maximum electric fields are typically near the electrodes. The main advantages of AFC compared to PZT wafer are 1) higher toughness due to capability of AFC to absorb more strain energy from the polymer substrates, 2) larger deformation (bending and/or twisting) related to piezoelectric effect, 3) potential of large-scale actuation and sensing in complaint and flexible smart structures and mechanisms, and 4) the existence of polymers prevent catastrophic failure due to fiber breakage (particularly in AFC due to the placement and arrangement of electrodes even when fracture occurs in some part of fibers the AFC still has the electro-mechanical coupling function). The microstructure of AFC enables it to easily be integrated in curved structures as well.

AFC electro-mechanical coupling properties also allow its use as sensors or emitters-receivers in various applications. As some examples of its applications, acoustic emission (AE) sensor, emitter-receiver pair for acoustic-ultrasonic (AU), strain gage [50], transducer probes for medical diagnostic ultrasound health monitoring of fetus, SONAR [51] and aero-elastic and structural acoustic control of rotary wing aircraft and rotor blades [52, 53] can be mentioned.

Some observations have showed the nonlinear and time-dependent responses of AFCs. Limited studies are available on the electro-mechanical nonlinear behavior of AFCs.

Mollayousef [49] and Ben Atitallah et al. [54, 55] have studied material characterization of AFC under a wider range of electro-mechanical loads. Mollayousef used a unit cell approach to characterize its electro-mechanical properties. Ben Atitallah et al. measured the material properties via experiments and showed nonlinear time and temperature dependent response of the composite under high temperatures and different strain rates as well as high electric voltages. Tajeddini et al. [56] modeled relaxation properties of AFCs and predicted creep response of the material under different temperatures and stress levels with quasi linear viscoelastic (QLV) approach.

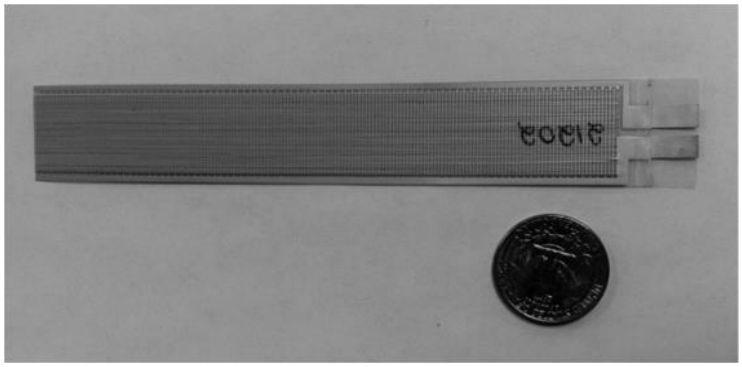

Figure 1.1. An AFC sample, manufactured by Advanced Cerametrics Incorporated

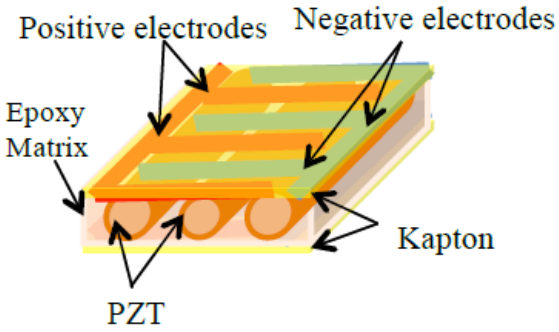

Figure 1.2. Schematic of an AFC [54]

1-1-3 Viscoelastic nature of polymers and large deformations analyses in viscoelastic structures

In many flexible structures, polymers are widely used because they can undergo large deformations, they are generally lightweight which is important in many applications, and

they can be easily fabricated with a relatively low cost. One of the prominent characteristics of polymers is their time-dependent (viscoelastic) behavior. It is noted that piezoelectric ceramics also show time-dependent responses (creep, hysteretic effect, loss and stored electro-mechanical properties that are frequency dependent). It is then necessary to consider the time-dependent behaviors in the smart structures with viscoelastic polymeric substrate and piezoelectric ceramics when they are subjected to mechanical and electrical stimuli. There are limited studies that address large deformations of viscoelastic solids. Ya-Peng and Ya-Fei [57] used the updated Green strain tensor and Kirchhoff stress tensor for analyzing large deformations in viscoelastic beams and used FEM for obtaining the solutions to the governing equations. Some analytical and numerical studies of large deformation beams with linear viscoelastic constitutive model are discussed by Holden [58], Baranenko [59], Lee [60], Vaz and Caire [61]. Few studies such as [62-64] have been reported on simulating moderate deformations and strains of viscoelastic plates by using von-Karman type strain-displacement relations. To the best of our knowledge, very limited studies address nonlinear deformation of active viscoelastic structures. Beldica and Hilton [65] studied stress, deformation and failure of a fiber composite beam with piezoelectric layers by considering general nonlinear anisotropic viscoelastic constitutive relations for piezoelectric layers and the beam. For incorporating large deformations they took into account a large rotation in expressing the curvature of the middle axis of the beam. Muliana and Tajeddini [66, 67] studied large deformations of viscoelastic homogeneous and composite beams semi-analytically by adopting Reissner's theory of beams to handle large curvature problems and considering load effect of the electrically activated thin piezoelectric patches. Yang and Zhang [68] studied bending of piezoelectric cylindrical shells based on nonlinear strains and applying finite difference method to solve the governing equations.

1-2 Scope of the present study

The focus of present study is on analyzing nonlinear deformations of elastic and viscoelastic smart flexible and foldable systems, such as slender beams, plates, and shells having multiple piezoelectric patches. The flexible structures are subjected to electrical and mechanical actuations in order to achieve large deformations and rotations. Linear and

nonlinear electro-mechanical constitutive models are incorporated for the piezoelectric patches, while elastic and viscoelastic behaviors are considered for the host structures. The results from the present analyses are useful for designing autonomous flexible devices that are activated by non-mechanical stimuli.

Smart flexible beams are considered first in Chapter 2. Analysis of large deformations of a smart elastic slender cantilever beam, i.e., homogeneous elastic beam with arbitrary number of piezoelectric actuator patches is presented. The beam is assumed relatively slender so that the effect of the transverse shear deformations on the lateral deflections of the beam can be neglected. The actuators are piezoelectric patches attached to the top and bottom surfaces of the beam symmetrically with respect to the middle axis or plane of the structure. To induce large deformations and curvatures in the beam, each pair of the actuators opposite to each other on the top and bottom of the substrate are subjected to large electric fields in a way that they experience opposite elongation and contraction along the longitudinal axis of the beam. The governing equations for large deformations in an elastic beam formulated by Reissner [17] are adopted and modified to include the electro-mechanical coupling effect from the piezoelectric patches. Analytical solutions of the governing equations are then presented for the deformations of the beams. When the cantilever smart beam is also subjected to mechanical loads, the nonlinear shooting method [22] is used to convert the boundary value problem from the governing equations of the deformations of the beams to an initial value problem, and a 4^{th}-Runge-Kutta method is used to numerically solve the initial value problem.

In Chapter 3, three-dimensional deformations of smart elastic shells integrated with piezoelectric patches undergoing large deformations are studied. Co-rotational finite element method is used for numerically solving the equations that govern the deformations of the electro-active shells. As in Chapter 2, a nonlinear electro-mechanical constitutive equation for the active piezoelectric materials is taken into account. Preliminary results of the deformations and shape changes of electro-active elastic shells are presented. It is noted that the nonlinear electro-mechanical constitutive model based on higher order function can also be used to capture electro-mechanical responses of other electro-active materials, such as electrostrictive, in which only the even terms are needed.

Chapter 4 discusses smart structures with viscoelastic characteristics and so time-dependent structural response is taken into account. As there are several advantages of using AFCs as mentioned above, it is expected that the integrated AFCs with the flexible shells will improve the actuation and deformation capability in the electro-active flexible structures. In addition, many of flexible structures consist of polymeric host structures, in which they show prominent viscoelastic behaviors. Formulation of CRFE of electro-active viscoelastic shells is presented in this chapter.

Chapter 5 presents conclusions and possible future research.

2. ANALYSIS OF SMART ELASTIC AND VISCOELASTIC BEAMS WITH GEOMETRIC NONLINEARITIES*

2-1 Distributed piezoelectric actuators on the supporting beam

Actuators, such as piezoelectric ceramics, have been widely used to actively control deformations and vibrations (Crawley and de Luis [69]) and reducing noises (Dimitriadis and Fuller [70]; Wang, Dimitriadis and Fuller [71]) in structures. To understand the behaviors of structures induced by actuators, equations that govern the deformations in active structures and constitutive models for all constituents have been formulated. There have been several studies done on developing models that describe the interaction between actuators and host structures. Crawley and de Luis [69] developed a model for piezo-ceramic patches bonded to the surface or embedded into the beams. They showed that the perfectly bonded distributed actuators result in two equivalent concentrated moments acting at the edges of an actuator patch. Im and Atluri [72] proposed a refined model including the transverse shear and axial forces in addition to the bending moments induced by actuators. Wang and Rogers [73] used the classical laminated plate theory to determine the equivalent force and moment induced by the actuator patches attached to or embedded into laminated beams and plates. Dimitriadis, Fuller and Rogers [74] also presented a two-dimensional model for piezo-ceramic patches ideally bonded on top and bottom surfaces of a rectangular plate, and showed that the resultant moments induced by the piezo-ceramic patches were along the edges of piezo-ceramic patches under an assumption of pure bending. The above studies focus on small deformations based on Euler-Bernoulli or classical Kirchhoff-Love plate theories of beams or plates integrated with piezoelectric actuators.

In this chapter, large deformations of active beams activated by piezoelectric materials are modeled. It is assumed that patches are perfectly bonded to the supporting structure and their thickness is much smaller than that of the host structure so that their effect

on the geometry and properties of the overall responses of the active beams is negligible. The actuators are needed to prescribe an external electrical stimulus. Quasi-static equilibrium and compatibility conditions are considered to estimate the bending moments induced by the actuator patches to the supporting beams or plates. When piezoelectric ceramics are considered, the patches are considered in the forms of several small segments distributed in the substrates as in practical applications the brittle nature of ceramics would lead to cracking. However, when other soft active materials are considered, such as piezoelectric polymers, it is possible to have long and continuous active components integrated to the substrates.

In this study, for each piezoelectric patch attached to the top surface of the supporting beam, there is a similar patch attached to the bottom surface and the geometry of the entire smart structure remains symmetric in the thickness direction of the structure and inducing bending moment about the middle-axis of the beam thickness. However this condition can be relaxed with a consequence of having axial-bending coupling effect. In rest of the study, a pair of patches is referred to two patches attached on top and bottom surfaces of the supporting structure. Also, the top and bottom piezoelectric patches have the same through the thickness poling direction, and in order to induce bending the piezoelectric patches are activated by applying voltages in opposite directions through their thickness.

Consider a segment of the beam in Figure 2.1 with its middle axis in *x*-direction and with a pair of piezoelectric patches bonded on the top and bottom surfaces. The thickness of the bonding agent and its effect on the overall deformations of the beams are neglected. The actuators with the same through the thickness poling direction as mentioned are excited by electric voltages in opposite directions. The magnitude and direction of the applied electric field are in such that the overall effect of the pair of active patches induces moments to the substrate which is discussed later. Incorporating the interaction of the patches and the substructure, the bottom actuator undergoes strain ε_{ac} while the top one undergoes strain $-\varepsilon_{ac}$. The axial deformation is assumed linearly varied through the thickness, and imposing small strain measures, the axial strain in the beam ε_b also linearly varies through the thickness of the beam as shown in Figure 2.1. At the interfaces between active materials and substrates displacement continuity is maintained.

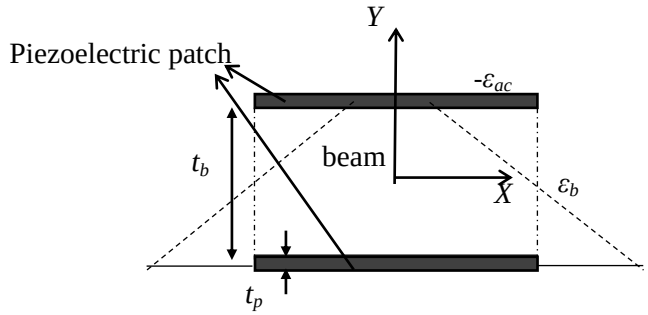

Figure 2.1. Strain distribution in the cross section of beam by an active piezoelectric patch

The piezoelectric material is assumed linear elastic with regard it its mechanical behavior, while linear and nonlinear responses are considered for the electro-mechanical coupling. The stress in the excited bottom actuator is expressed as

$$\sigma_{ac} = E_p(\varepsilon_p - \varepsilon_{ac}) \tag{2.1}$$

where E_p is the elastic modulus of the piezoelectric actuator, ε_p is the piezoelectric free strain, which is a strain in the actuator due to applied electric field without constraints to the actuator. The strain ε_{ac} is generally smaller than ε_p due to the constraints from imposing the compatibility condition between the beam and actuator, and equilibrium of forces and moments. The stress in the top patch has the same magnitude as the stress in the top patch in Eq. (2.1), but in compression. Thus, the moment M_{ac} induced by the stressed actuators in Eq. (2.1) with the respect to middle axis of the beam is expressed as

$$M_{ac} = t_p b\left(t_p + t_b\right) E_p(\varepsilon_p - \varepsilon_{ac}) \tag{2.2}$$

where b is width of the beam; t_p and t_b are thicknesses of patches and the beam respectively.

If a linear elastic beam is considered, the stress in the beam is given as:

$$\sigma_b = E_b \varepsilon_b \tag{2.3}$$

where E_b is the elastic modulus of the beam. Hence, an equivalent bending moment in the beam is obtained from following expression:

$$M_0 = -\int_{-\frac{t_b}{2}}^{\frac{t_b}{2}} E_b \varepsilon_b Y b dY \tag{2.4}$$

Considering the beam segment and the patches as a system, the equilibrium of moments about the middle axis of the beam gives $M_{ac} = M_0$. By equating Eq. (2.2) and (2.4), the induced moment due to application of electric field in the piezoelectric patches is expressed as

$$M_0 = \frac{-b t_p {t_b}^3 \left(t_p + t_b\right) E_p E_b}{{t_b}^3 E_b + 6 t_p \left(\frac{t_p}{2} + t_b\right)\left(t_p + t_b\right) E_p} \varepsilon_p \tag{2.5}$$

If it is assumed that the thickness of the piezoelectric patches is much smaller than the thickness of the beam, $t_p << t_b$, Eq. (2.5) can be approximated as

$$M_0 \approx \frac{-bt_p t_b^{\,2} E_p E_b}{t_b E_b + 6t_p E_p}\varepsilon_p \tag{2.6}$$

Depending on the magnitude of electric field applied and the response of piezoelectric material, the strain in the piezoelectric patches is expressed as follows:

$$\varepsilon_p = d_{12} E^e \tag{2.7}$$

when a linear electro-mechanical constitutive relation is considered, which is valid only for relatively small amount of electric field input. When a relatively large electric field input is considered, constitutive models with higher order electric fields are considered, such as a second order constitutive relation for large electric field [45]:

$$\varepsilon_p = d_{12} E^e + \frac{1}{2}\beta_{12} E^{e\ 2} + HOT \tag{2.8}$$

where d_{12} is piezoelectric constant and E^e is electric field in thickness direction, *Y*, of the patch. β_{12} is the higher order piezoelectric constant. The above models in Eqs. (2.8) and (2.9) are for polarized piezoelectric samples, and valid for electric field smaller than the coercive electric limit of the materials, so that depolarization does not occur. As also seen from Eq. (2.8) when d_{12} is taken as 0, the second order terms can be used to describe electro-mechanical responses of electrostrictive materials.

As mentioned, it is assumed that the top and bottom piezoelectric patches have the same through the thickness poling direction. Also, as discussed, to induce only bending moment by a pair of patches on top and bottom of the beam, ε_p of the top patch should have the same magnitude as of the bottom patch but with opposite sign. Consequently, according to Eq, (2.7), if the piezoelectric material show a linear behavior due to the electric field input,

the magnitude of the electric field applied to the patch on top should be the same as the one to the bottom patch but in opposite direction:

$$E^e\big|_{top} = -E^e\big|_{bottom} \tag{2.9}$$

However, for a nonlinear behavior of the actuators according to Eq. (2.8), the applied electric field in top patch with respect to the on in bottom patch has different magnitude and may be in same direction or opposite direction as expressed in Eq. (2.10) and Eq. (2.11), respectively.

$$E^e\big|_{top} = -\left(\frac{\sqrt{{d_{21}}^2 + 2\beta_{12}\left(d_{12}\, E^e\big|_{bottom} + 0.5\beta_{12}\, {E^e\big|_{bottom}}^2 \right)} + d_{12}}{\beta_{12}} \right) \tag{2.10}$$

$$E^e\big|_{top} = \frac{\sqrt{{d_{12}}^2 + 2\beta_{12}\left(d_{12}\, E^e\big|_{bottom} + 0.5\beta_{12}\, {E^e\big|_{bottom}}^2 \right)} - d_{12}}{\beta_{12}} \tag{2.11}$$

2-2 Formulations for nonlinear analysis of smart beams

This study adopts the kinematic and governing equations for large deformation of beams, presented by Reissner [17], where large stretch and rotation are possible and the effect of the transverse shear deformations are accounted for. For the current study, a slender beam with integrated piezoelectric patches is considered so that the large deformation in the beam is mainly due to rotation, while the beam is undergoing small strains. Furthermore, the effect of transverse shear deformation is neglected. Consider an originally straight cantilever beam under electric field inputs applied to the pair of piezoelectric patches, which causes the beam to deform, as shown in Figure 2.2.

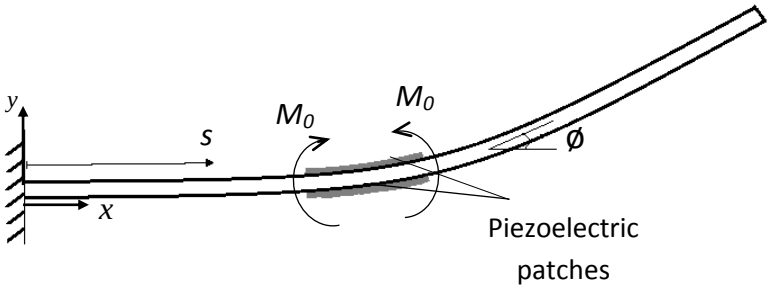

Figure 2.2. Deformation of a cantilever beam with a pair of piezoelectric patches to induced bending

Following Reissner's formulation for large deformations of slender beams, the deformation of the beam actuated by non-mechanical effect is also studied. The beam is initially straight and subjected to the following internal shear force *Q*, normal force *N* and bending moment *M*. Consider a differential element of the straight beam with length *ds* at location *s* before deformation as shown in Figure 2.3a. After deformations, the current location of the element is $x(s)=s+u(s)$ and $y(s)=v(s)$, where $u(s)$ and $v(s)$ are the displacement in the *x* and *y* axes, respectively. The kinematic relations for the displacements and rotation of the beam element are written as:

$$\begin{aligned} 1+u' &= (1+\varepsilon)\cos\phi \\ v' &= (1+\varepsilon)\sin\phi \end{aligned} \tag{2.13}$$

where ϕ is the rotational angle of the cross-section when the beam deforms.; thus, ϕ' is the curvature of the deformed beam, ε is the axial strain along the centroidal axis of the beam which, in case of no shear strain, is the same as the relative change of length of a differential element of the beam axis due to deformation. ()' stands for the derivative with respect to *s*, which is the distance along the length of the beam measured from its left end. Referring to

Figure 2.3b, the force and moment equilibriums of the differential element lead to the following system of equations:

$$\begin{aligned} M' + (1+\varepsilon)Q &= 0, \\ N' + \phi' Q &= 0, \\ \phi' N - Q' &= 0. \end{aligned} \tag{2.14}$$

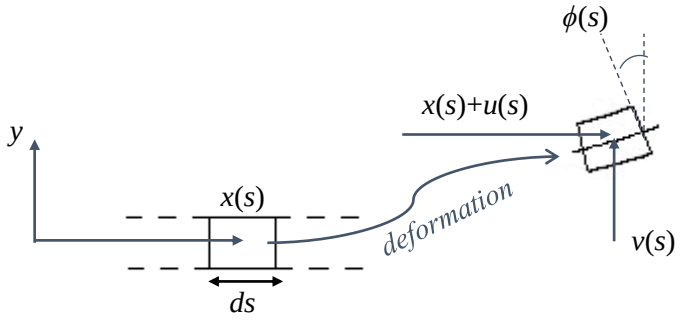

(a)

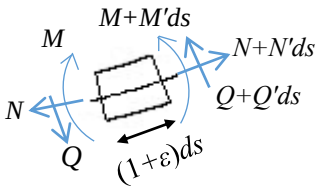

(b)

Figure 2.3. (a) Kinematics of an element of the beam before and after deformation and (b) free body diagram of an element of the beam

A linear elastic constitutive relation for the beam (host structure) and equilibrium equations in terms of the axial force and bending moment lead to:

$$\begin{aligned} N &= E_b A \varepsilon \\ M &= E_b I \phi' \end{aligned} \tag{2.15}$$

here E_bA and E_bI are the axial stiffness and bending stiffness of the beam respectively.

Under a pure bending condition, deformation of a cantilever beam, Eqs. (2.13-15), can be solved analytically in order to obtain displacement components of the beam. In cases other than pure bending, for instance when the patches excite axial forces in the substructure or when mechanical loads are applied to the beam, closed form expressions for the deformed configuration are not necessarily available and a numerical method is then considered. One of the available numerical methods is nonlinear shooting method presented by Banerjee et al. [22] for obtaining solutions to large deformations of beams. The method is briefly described here and used for the analyses in Section 2.4.

Consider a beam under a bending moment and concentrated forces F_x and F_y, shown in Figure 2.4. The bending moment at a point (x,y) of the cantilever beam is expressed as

$$M(x,y) = F_x(d_y - y) + F_y(d_x - x) + M_0\left[u(s-l_1) - u(s-l_2)\right] \tag{2.16}$$

where $u(s)$ is a unit step function; F_x and F_y are the components of the concentrated force in x and y directions, respectively, and d_x and d_y are the x-direction and y-direction distance of the force from the clamped end.

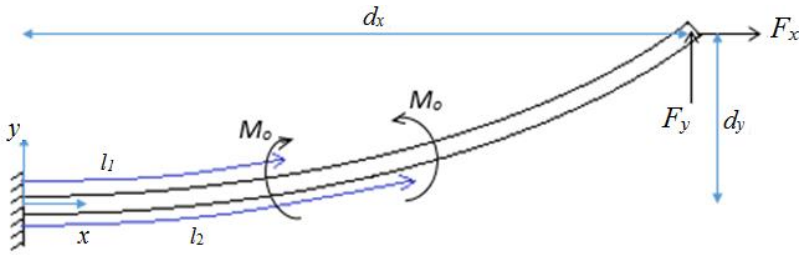

Figure 2.4. Configuration of cantilever beam under applied moment and force

By substituting Eq. (2.13) into moment-curvature relation in Eq. (2.15) and differentiating with respect to *s*, the first derivative of the curvature is given as:

$$\phi'' = -\frac{1}{E_b I}(F_y \cos\phi + F_x \sin\phi) + M_o\left[\delta(s-l_1) - \delta(s-l_2)\right] \tag{2.17}$$

where $\delta(s)$ is Dirac-Delta function. The boundary conditions for a cantilever beam are

$$\begin{aligned} \phi\big|_{s=0} &= 0\,, \\ \phi'\big|_{s=L} &= 0 \end{aligned} \tag{2.18}$$

The boundary value problem is transformed to an initial value problem (IVP) by estimating a value *m* for curvature at *s*=0. So the initial values for Eq. (2.17) are

$$\begin{aligned} \phi\big|_{s=0} &= 0\,, \\ \phi'\big|_{s=0} &= m \end{aligned} \tag{2.19}$$

This initial value problem is then solved by 4th order Runge-Kutta; then, the curvature at *s*=*L* named λ, which is equal to zero here, is used as a reference to evaluate the trial value *m* that is expected to be close to the actual value for $\phi'\big|_{s=0}$. The trial value *m* is then modified and this procedure is repeated for several steps until the calculated $\phi'\big|_{s=L}$ is close enough to the λ with a rate depending on the initial estimation for *m*. At each step, *k*, the formula for deriving m_k is expressed as

$$m_k = m_{k-1} - \frac{\phi'|_{s=L} - \lambda}{\frac{\partial}{\partial m}\left(\phi'|_{s=L}\right)} \tag{2.20}$$

It is seen that $\frac{\partial}{\partial m}\left(\phi'|_{s=L}\right)$ should be calculated as well. The right side of Eq. (2.17) is expressed as $f(s, \phi, \phi')$ and a new variable $\psi = \frac{\partial \phi}{\partial m}$ is defined. By introducing new variables as $\xi = \phi'$ and $\zeta = \psi'$, and after some algebraic manipulations, a system of first order differential equations is derived. In each step *k*, 4th order Runge-Kutta method is used to solve the IVP in Eq. (2.17):

$$\begin{aligned} D.E. &\begin{cases} \phi' = \xi \\ \xi' = f(s, \phi, \xi) \\ \psi' = \zeta \\ \zeta' = f_{,\phi}\psi + f_{,\xi}\zeta \end{cases} \\ I.C. &\begin{cases} \phi|_{s=0} = 0 \\ \xi|_{s=0} = m_k \\ \psi_{s=0} = 0 \\ \zeta|_{s=0} = 1 \end{cases} \end{aligned} \tag{2.21}$$

which gives $\xi|_{s=L} = \left(\phi'|_{s=L}\right)$ and $\zeta|_{s=L}\left(= \frac{\partial}{\partial m}\left(\phi'|_{s=L}\right)\right)$. For the next step, the modified m_{k+1} is calculated from Eq. (2.20) and the above procedure is repeated until the solution converges or $\xi|_{s=L} \to \lambda$. Finally the curvature of the beam is determined and the deformed configuration of the beam can be obtained from the kinematic relations Eq. (2.13).

2-3 Governing equations for active viscoelastic beams

In this section, a time-dependent parameter is taken into account for analyzing deformations in active beams with viscoelastic host structures. A constitutive relation for the axial strain in a linear viscoelastic beam is described as follows

$$\varepsilon_b(x,y,t) = \int_{0^-}^{t} J(t-\tau)\frac{d\sigma(x,y,\tau)}{d\tau}d\tau \tag{2.22}$$

where σ is the axial stress and $J(t)$ is the creep function of the beam. The equation for the bending moment is obtained by multiplying both sides of Eq. (2.22) by a distance *y* measured from a mid-surface of the beam and integrating both sides over the cross-section area of the beam:

$$\int_A y\varepsilon_b(x,y,t)dA = \int_A y\int_{0^-}^{t} J(t-\tau)\frac{d\sigma(x,y,\tau)}{d\tau}d\tau\, dA = \int_{0^-}^{t} J(t-\tau)\frac{dM_0(x,y,\tau)}{d\tau}d\tau \tag{2.23}$$

M_0 is an induced moment in the beam as expressed in Eq. (2.4). By considering the time-dependence material properties of the beam, similar to elastic case referring to from moments equilibrium conditions,

$$M_{ac} = M_0 \tag{2.24}$$

or in terms of strains,

$$t_p\left(t_b+t_p\right)E_p\varepsilon_p(t)=\frac{1}{6}t_b^2\int_0^t E_b(t-\tau)\frac{d\varepsilon_{ac}(\tau)}{d\tau}\mathrm{d}\tau+t_p\left(t_b+t_p\right)E_p\varepsilon_{ac}(t) \qquad (2.25)$$

$E_b(t)$ is the relaxation function of the viscoelastic substrate. To solve Eq. (2.25), Laplace transformation is utilized to make it a linear equation as follows

$$t_p\left(t_b+t_p\right)E_p\tilde{\varepsilon}_p=\frac{1}{6}t_b^2\tilde{E}_b\tilde{\mathrm{D}}\tilde{\varepsilon}_{ac}+t_p\left(t_b+t_p\right)E_p\tilde{\mathrm{D}}\tilde{\varepsilon}_{ac}/s \qquad (2.26)$$

D represents time derivative and '~' denotes for the quantity in Laplace space. It should be noted that $\tilde{\mathrm{D}}$ means derivative with respect to *s* in Laplace space. From the Eq. (2.26),

$$s\tilde{\varepsilon}_{ac}=t_p\left(t_b+t_p\right)E_p\tilde{\varepsilon}_p/\left(t_b^2\tilde{E}_b/6+t_p\left(t_b+t_p\right)E_p/s\right) \qquad (2.27)$$

and by taking the inverse Laplace transformation ε_{ac} as a function of time can be determined. The moment and strain relations are:

$$M_0=-\int_{-\frac{t_b}{2}}^{\frac{t_b}{2}}\int_{0^-}^{t}E_b(t-\tau)\frac{d\varepsilon_b}{d\tau}d\tau\,ydy=-\frac{bt_b^{\,3}}{t_b+\frac{t_p}{2}}\int_{0^-}^{t}E_b(t-\tau)\frac{d\varepsilon_{ac}}{d\tau}d\tau \qquad (2.28)$$

$E_b(t)$,the relaxation function, which is related to the creep function of the beam J_b as follows

$$1 = J_b(0)E_b(t) + \int_{0^+}^{t} E_b(t-\tau)\frac{dJ_b(\tau)}{d\tau}d\tau \tag{2.29}$$

In this study, the mechanical response of the actuators is assumed linear elastic. Thus, ε_p is given in Eq. (2.8) or (2.9). By assuming no longitudinal extension of the centroidal axis of the beam under pure bending moment, the strain can be written in terms of the curvature as $\varepsilon = -y\phi'$. Thus, Eq. (2.23) is rewritten as

$$I_y\phi' = J_b(t)M_0(x,0) + \int_{0^+}^{t} J_b(t-\tau)\frac{dM_0(x,\tau)}{d\tau}d\tau \tag{2.30}$$

By solving Eq. (2.30) for curvature, the deformed configuration of the beam can be obtained in a similar way as for the elastic case.

2-4 Boundary value problems

This section presents analyses of boundary value problems for elastic and viscoelastic beams having several arrangements of piezoelectric patches. Linear and nonlinear electro-mechanical responses are considered for the piezoelectric patches. Analyses of shape changing in smart beams controlled by electric field inputs are presented.

2-4-1 Elastic beam with multiple pairs of piezoelectric patches

Bending of smart cantilever beams with several pairs of piezoelectric patches is presented. Figure 2.5a shows an undeformed cantilever beam with a pair of piezoelectric patches with length l_p attached to the top and bottom surface of the beam. The piezoelectric patches are assumed to be homogeneous having the same width as the beam. From Eqs.

(2.13) and (2.15), the closed form solution for the displacement components, *u* and *v*, in term of *s* are:

$$\begin{cases} u = 0 \\ v = 0 \end{cases} \qquad 0 < s < l_1$$

$$\begin{cases} u = -\dfrac{E_b I}{M_o}\left(\sin\dfrac{M_0(l_1 - s)}{E_b I}\right) - s + l_1 \\ v = \dfrac{E_b I}{M_o}\left(\cos\dfrac{M_0(l_1 - s)}{E_b I} - 1\right) \end{cases} \qquad l_1 < s < l_1 + l_p \tag{2.31}$$

$$\begin{cases} u = \left(\cos\dfrac{M_0 l_p}{E_b I} - 1\right)s + l_1 + \dfrac{EI}{M_o}\left(\sin\dfrac{M_0 l_p}{E_b I}\right) - (l_1 + l_p)\cos\dfrac{M_0 l_p}{E_b I} \\ v = -\left(\sin\dfrac{M_0(l_1 - s)}{E_b I}\right)s + \dfrac{EI}{M_o}\left(\cos\dfrac{M_0 l_p}{E_b I} - 1\right) + (l_1 + l_p)\sin\dfrac{M_0 l_p}{E_b I} \end{cases} \qquad l_1 + l_p < s$$

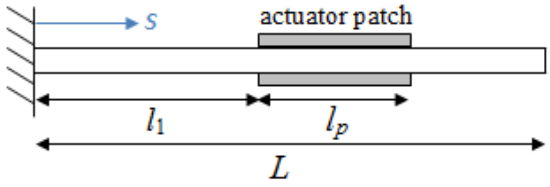

(a)

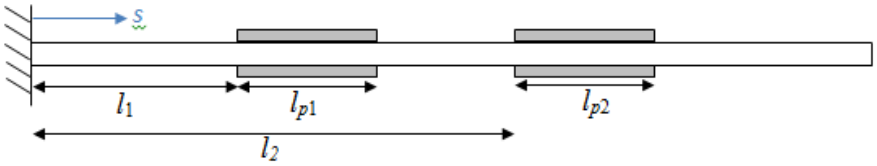

(b)

Figure 2.5. Cantilever beam with one (a) and two (b) pairs of piezoelectric patches

It is possible to attach several pairs of piezoelectric patches along the length of the beam and different magnitude of electric field can be applied to the piezoelectric patches in

order to induce various shape changes. Placing several small segment of patches is practically useful when piezoelectric ceramics is considered. Consider now a cantilever beam with two piezoelectric patches and geometric quantities shown in Figure 2.5b. The moments generated by the two pairs of the piezoelectric patches from left to right are M_1 and M_2, respectively. The closed form solutions for the displacement components of the elastic beam are:

$$\begin{cases} u = 0 \\ v = 0 \end{cases} \qquad 0 < s < l_1$$

$$\begin{cases} u = -\dfrac{E_b I}{M_o} \sin \dfrac{M_1 (l_1 - s)}{E_b I} - s + l_1 \\ v = \dfrac{E_b I}{M_o} \left(\cos \dfrac{M_1 (l_1 - s)}{E_b I} - 1 \right) \end{cases} \qquad l_1 < s < l_1 + l_{p1}$$

$$\begin{cases} u = \left(\cos \dfrac{M_1 l_{p1}}{E_b I} - 1 \right) s + l_1 + \dfrac{E_b I}{M_o} \left(\sin \dfrac{M_1 l_{p1}}{E_b I} \right) - (l_1 + l_{p1}) \cos \dfrac{M_1 l_{p1}}{E_b I} \\ v = -\left(\sin \dfrac{M_1 (l_1 - s)}{E_b I} \right) s + \dfrac{E_b I}{M_o} \left(\cos \dfrac{M_1 l_{p1}}{E_b I} - 1 \right) + (l_1 + l_{p1}) \sin \dfrac{M_1 l_{p1}}{E_b I} \end{cases} \qquad l_1 + l_{p1} < s < l_2$$

(2.32-1)

for $l_2 < s < l_2 + l_{p2}$:

$$\begin{cases} u = -\left(\dfrac{E_b I}{M_2} \right) \sin(\varphi) - s + c^{(1)} \\ v = \left(\dfrac{E_b I}{M_2} \right) \cos(\varphi) + c^{(2)} \end{cases} \qquad (2.32\text{-}2)$$

where

$$\phi = -\frac{M_2}{E_b I} s + \frac{M_2 l_2 - M_1 l_{p1}}{E_b I}$$

$$c^{(1)} = l_1 + (l_2 - l_1 - l_{p1})\cos\frac{M_1 l_{p1}}{E_b I} + EI\left(\frac{1}{M_1} - \frac{1}{M_2}\right)\sin\left(\frac{M_1 l_{p1}}{E_b I}\right)$$

$$c^{(2)} = -\left(l_2 - l_1 - l_{p1}\right)\sin\frac{M_1 l_{p1}}{E_b I} - \frac{E_b I}{M_2}\cos\left(\frac{M_1 l_{p1}}{E_b I}\right) - \frac{E_b I}{M_1}\left(1 - \cos\frac{M_1 l_{p1}}{E_b I}\right)$$

for $l_2 + l_{p2} < s$:

$$\begin{cases} u = \left(\cos\phi - 1\right)s + c^{(1)} \\ v = -\left(\sin\phi\right)s + c^{(2)} \end{cases} \tag{2.32-3}$$

where

$$\phi = \frac{M_1 l_{p1} + M_2 l_{p2}}{E_b I}$$

$$c^{(1)} = l_1 + \left(l_2 - l_1 - l_{p1}\right)\cos\frac{M_1 l_{p1}}{E_b I} - (l_3 + l_{p2})\cos\left(\frac{M_1 l_{p1} + M_2 l_{p2}}{E_b I}\right) + \frac{E_b I}{M_2}\left[\sin\left(\frac{M_1 l_{p1} + M_2 l_{p2}}{E_b I}\right) - \sin\frac{M_1 l_{p1}}{E_b I}\right]$$

$$c^{(2)} = \left(l_1 + l_{p1} - l_2\right)\sin\frac{M_1 l_{p1}}{E_b I} + (l_3 + l_{p2})\sin\left(\frac{M_1 l_{p1} + M_2 l_{p2}}{E_b I}\right) + \frac{E_b I}{M_2}\left[\cos\left(\frac{M_1 l_{p1} + M_2 l_{p2}}{E_b I}\right) - \cos\frac{M_1 l_{p1}}{E_b I}\right] - \frac{E_b I}{M_1}\left(1 - \cos\frac{M_1 l_{p1}}{E_b I}\right)$$

In general, any number of piezoelectric patches can be added to the cantilever beam and a closed form solution for deformation of the beam under induced bending moments can be derived. The general procedure is to calculate the rotational angle of the axis of the deformed beam ϕ from moment-curvature constitutive relation at first and then deriving deformation components in every location of the beam from the kinematics relation. In calculating the displacements, the compatibility condition (continuity displacements) at the interface of each two adjacent segments of the beam is considered as the boundary conditions for analyzing the deformation of each segment. Consider a part of the beam with multiple piezoelectric patches on its top and bottom as shown in Figure 2.6. Continuity of the

displacement between the adjacent segments of the beams leads to boundary conditions as follows:

$$\begin{aligned} \phi_i(s_i) &= \phi_{i+1}(s_i) \\ u_i(s)\big|_{s=s_i} &= u_{i+1}(s)\big|_{s=s_i} \\ v_i(s)\big|_{s=s_i} &= v_{i+1}(s)\big|_{s=s_i} \end{aligned} \tag{2.33}$$

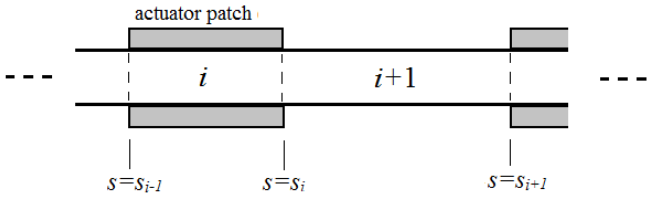

Figure 2.6. A part of the beam with multiple attached patches with pair i shown

From Eq. (2.13), the displacement components for segment i and $i+1$, respectively, are:

$$\begin{aligned} u_i(s) &= \int \cos\phi_i(s)\,ds - s + c_i^{(1)} \\ v_i(s) &= \int \sin\phi_i(s)\,ds + c_{(i)}^{(2)} \end{aligned} \tag{2.34-1}$$

$$\begin{aligned} u_{i+1}(s) &= \left(\sin\phi_{i+1} - 1\right)s + c_{(i+1)}^{(1)} \\ v_{i+1}(s) &= -\left(\cos\phi_{i+1}\right)s + c_{(i+1)}^{(2)} \end{aligned} \tag{2.34-2}$$

The constants $c_i^{(1)}$, $c_i^{(2)}$, $c_{i+1}^{(1)}$ and $c_{i+1}^{(2)}$ are derived from Eq. (2.33). It should be noted that the rotation of segment $i+1, \phi_{i+1}$, is constant due to no internal force or moment in the segment.

As mentioned earlier, the induced bending moment depends on the axial strain in the excited actuator patches which may be linearly or nonlinearly proportional to the applied

electric field. The effect of linear versus nonlinear response of the piezoelectric material on the deformation of a cantilever beam with two pairs of piezoelectric patches is shown in Figure 2.7. To obtain the results, the linear and quadratic terms of the piezoelectric coeficients are chosen as d_{13}=0.18 nm/V and β_{13}=8×10^{-7} n m^2 /V^2 [45] which are reported for piezoelectric material PZT G-1195. As seen in the figure, assuming a linear response of piezoelectric material with respect to electric field underestimates the bending moment. In this example, the position and length of the patches are $l_1 = 0.25L$ $l_2 = 0.6L$ and $l_{p2} = l_{p1} = 0.15L$, respectively and E^e=1.3 MV/m. The magnitude of applied electric field is smaller than the coercive limit of the material.

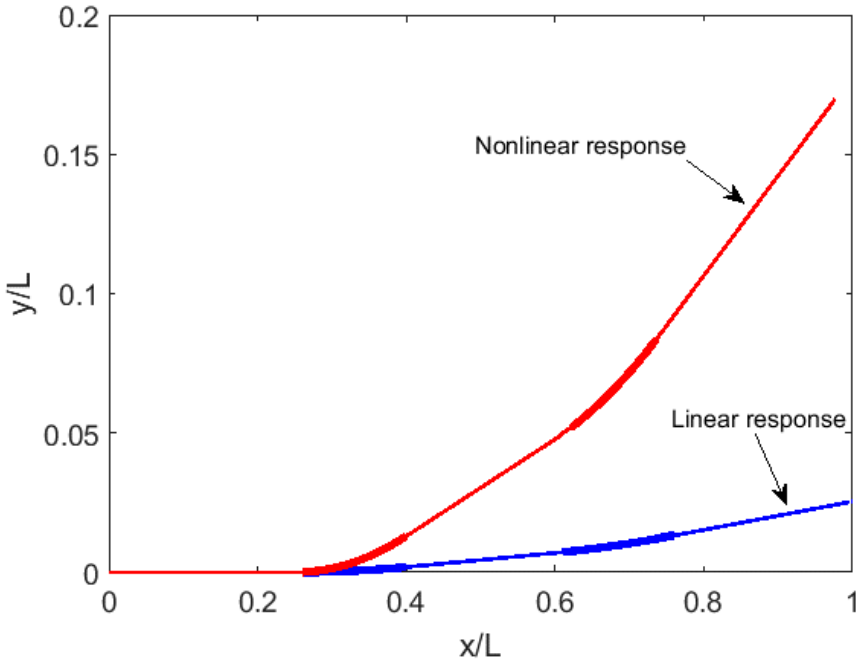

Figure 2.7. Deflection of the cantilever beam with one pairs of actuator patches their strain depends on the electric field: — linearly and - - - quadratically

Next, The deformation of a cantilever beam actuated electrically by the piezoelectric patches and mechanically by a concentrated force at its free end is analyzed by solving Eq. (2.17) using the nonlinear shooting method. Three smart beams are studied and the responses are shown in Figure 2.8. The analyses are done by considering $F_xL^2/E_bI = F_yL^2/E_bI$= 0.2 where F_x and F_y are components of the applied F; all the patches are assumed to be the same

length and thickness and subjected to the same amount of electric field such that for each pair $M_0 L / E_b I = 1$. This excersice is conducted to test the solution method presented in this study.

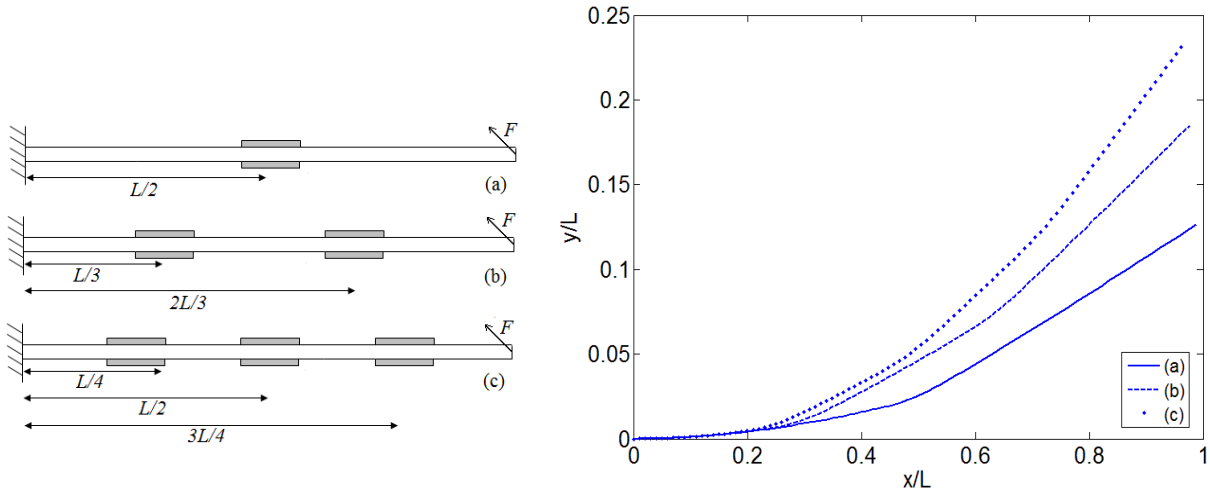

(a) (b)

Figure 2.8. Deformation of cantilever beam with one (a), two (b) and three (c) pairs of patches under electro-mechanical actuation

2-4-2 Shape control applications

Shape changes in thin smart flexible beams can be obtained by applying electric fields to the piezoelectric patches. Desired configurations can be achieved in principle by selecting appropriate values for the electric field inputs at different locations along the beams. The presented analyses can be used for preliminary design of flexible systems controlled by mechanial and non-mechanial stimuli. For example a gripper can be design in which the claws are in the forms of slender cantilever beams which can be folded, in order to hold an object, by by prescribing electric fields. Figure 2.9 shows a schematic of a four-claw gripper that consists of four cantilever thin beams as its claws. This type of gripper may be used in robots to grab and carry objects.

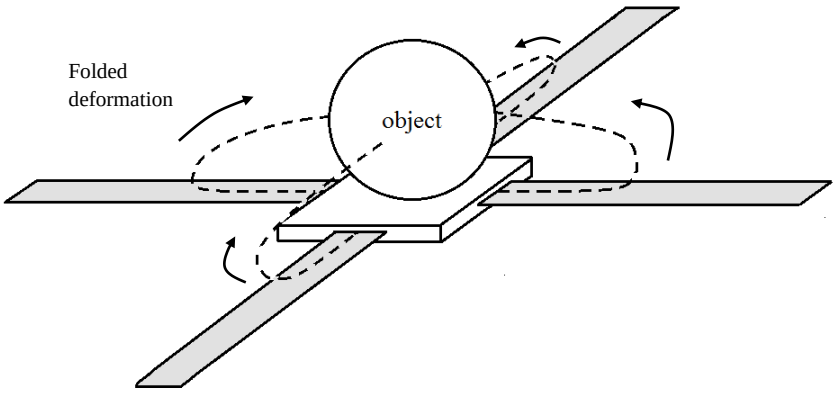

Figure 2.9. Schematic of a gripper with four smart beams as its claws

Figure 2.10a shows an example of a deformed shape of a smart beam with two pairs of actuators placed at the locations $l_1 = 0.5L$, $l_2 = 0.62L$. The two actuators have the same length, $l_{p1} = l_{p2}$, but having different bending moments $M_2 = 2.92M_1$ with $M_1 L / E_b I = 8$ and E_1^e =1.3MV/m with assumption of nonlinear response for the piezoelectric patches. The bending moments are the results of applying the electric fields through the piezoelectric patches, in Eq. (2.6). As far as the shape of the deformed beam is concerned, multiple variables can be controlled and studied, such as number of actuator patches, their geometrical properties, their location, magnitude of applied voltage etc. For instance, the same form for the deformation can be obtained by installing pairs of the patches with the same magnitude of induced moments and the same distance from each other, but by changing the length of one or both the pairs of patches. Figure 2.10b shows the deformation of the beam for same positions for the patches but $M_2 = M_1$, and $l_{p2} = 2.92 l_{p1}$ and E^e=1.32MV/m.

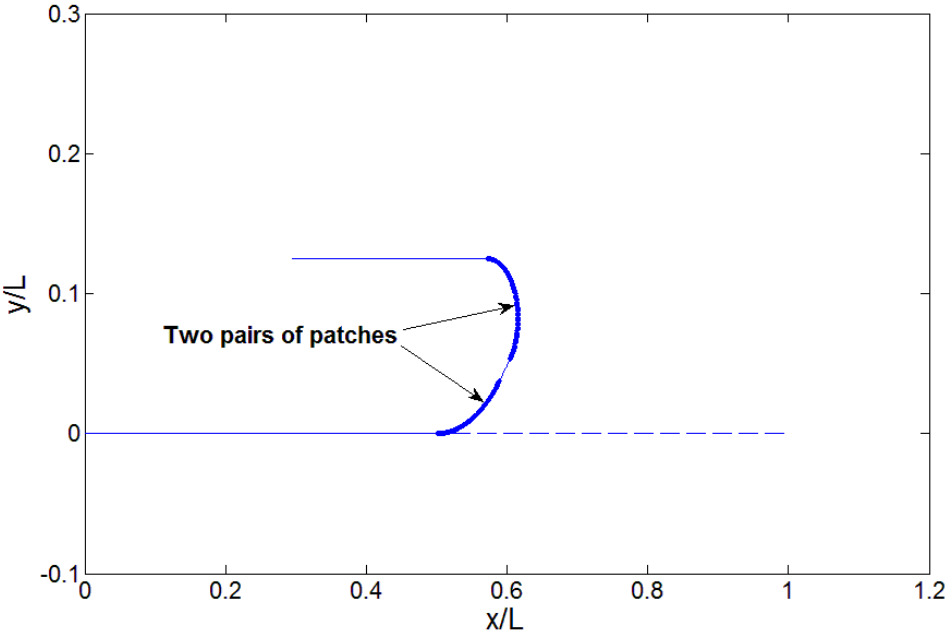

(a)

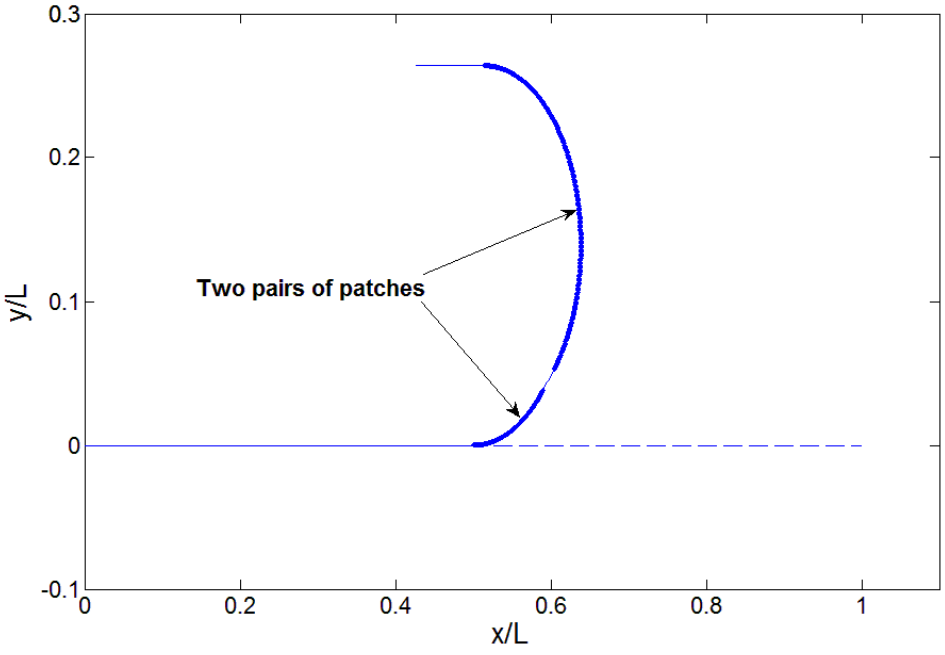

(b)

Figure 2.10. U-shaped beam under actuation of two pairs of patches with same length (a) and different lengths (b)

Another example is folding of slender beams under actuation of multiple patches, which may be used in deployable systems. Figure 2.11 shows a beam with five pairs of patches attached to them. The beam is originally straight (figure 2.11a) with patch labels shown. Nonlinear response in terms of electric field is assumed for the actuators and an electric field E^e=1.2 MV/m is applied to the patch number one and it generates bending moment as $M_0 L / E_b I = 21$ which folds the tip of the beam into a ring- shape configuration (Figure 2.11b). Then, the next patch undergoes the same magnitude of electric field and another pair of moment induced to the beam so larger part of the beam folds (Figure 2.11c). This process of actuating can be continued by patches three, four and five, and the ring-shape moves to the left as seen in Figure 2.11c-e respectively. It should be noted that since the beam and the patches are elastic, the configuration of the beam does not depend on the history of applied electric fields.

For this example the amount axial strain of the beam is calculated. According to Eq. (2.15), curvature of the beam is $\phi' = M_0 / E_b I$ and under pure bending, axial strain along thickness of the beam is calculated as $\varepsilon_x = z\phi'$. Therefore, maximum axial strain of the beam is at $z = \pm t/2$ along the segments covered by the active patches. For the presented example, the calculated maximum axial strain is around 7%.

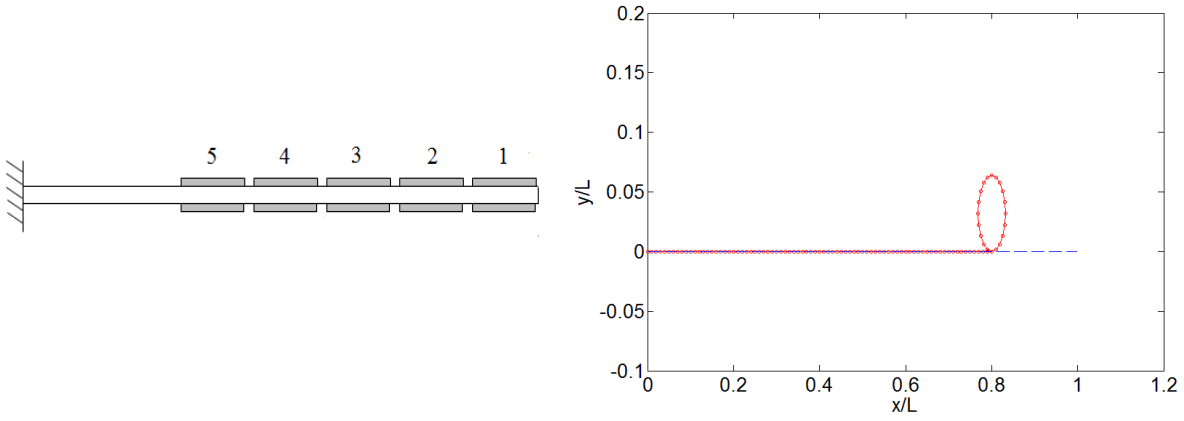

(a) (b)

Figure 2.11. Rolling configuration of an originally straight cantilever beam (a) under actuation of one to five active pair of patches (b-f)

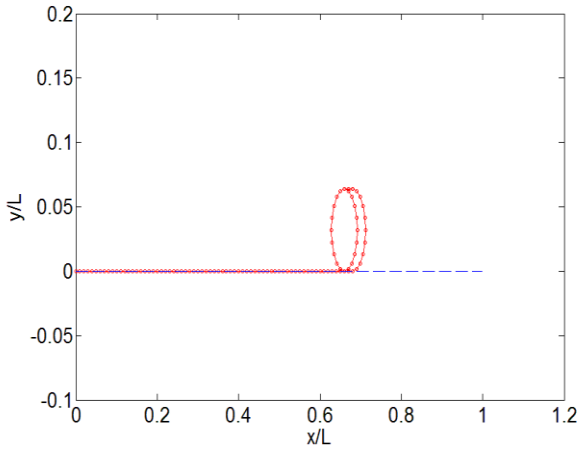

(c)

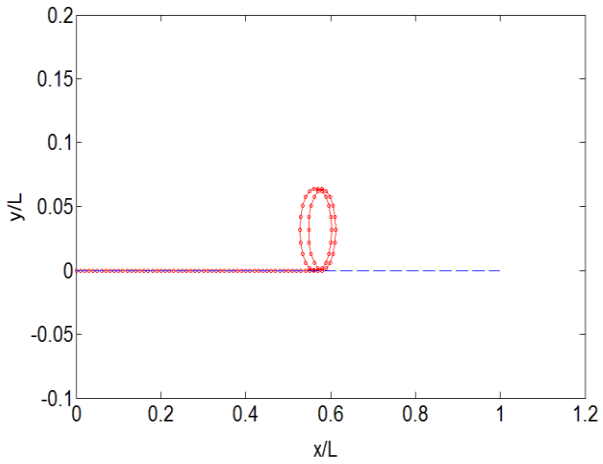

(d)

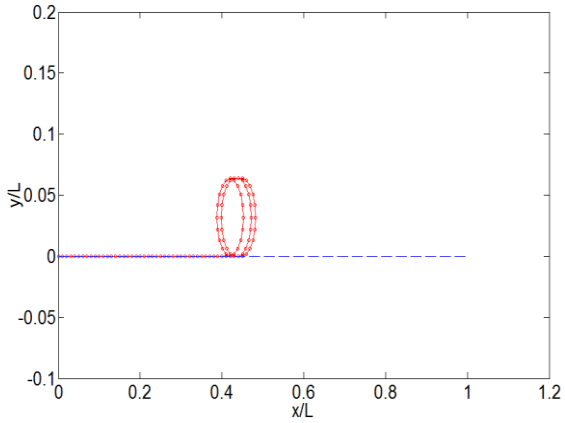

(e)

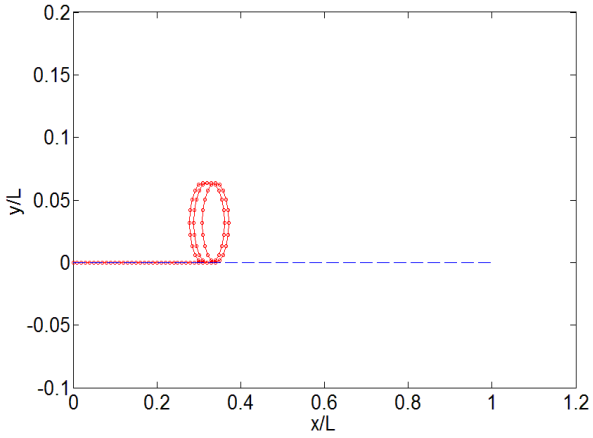

(f)

Figure 2.11. Continued

2-4-3 Viscoelastic beam integrated with elastic piezoelectric patches

Finally, a viscoelastic cantilever beam with two patches is considered. The patches with length l_{p1} and l_{p2} are attached at left and right ends of the beams, respectively as shown in Figure 2.12.

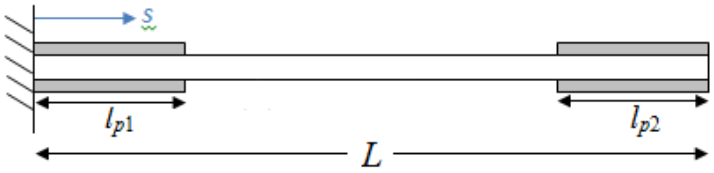

Figure 2.12. Cantilever viscoelastic beam with two patches in undeformed shape

The nonlinear strain of the piezoelectric material is considered as $\varepsilon_p = d_1 E^e + d_2 E^{e\,2}$. The properties of the beam and the patches are chosen as: $d_1 = 0.18$ nm/V, $d_2 = 0.8$ f(m/V)^2, $E_p = 63$ GPa, $E_b = 0.8\left(1 - 0.95\left(1 - e^{-t/\tau_0}\right)\right)$ GPa where τ_0 is characteristic time l_{p1}=l_{p2} =0.2 L and t_p=0.1t_b =0.1mm. As a common type of loading history, the time-dependent electric voltage is considered to increase from zero to a maximum value E_m^e fast and then remains constant. The following function which is continuous over time approximates very well the described load history input:

$$E^e(t) = E_m^e(1 - e^{-50t}) \tag{2.35}$$

The time-dependent deformation of the beam with relaxation function, is obtained and shown in Figure 2.13 for electric field histories, Eq. (2.35) with $E_m^e = 1.4$ MV/m and with three characteristic time, τ_0 =0.5, 2 and 20sec. The curvature of the shell increases gradually at early time but it almost remains unchanged after T=1sec and so the configuration of the structure remains constant although the relaxation modulus of the viscoelastic shell decreases over time. The reason is that during stress relaxation within the substrate, the induced moment, which depends on the relaxation modulus of the substrates (Eqs. 2.24 and 2.25), from the activated actuators also relaxes with time (refer to figure 2.14).

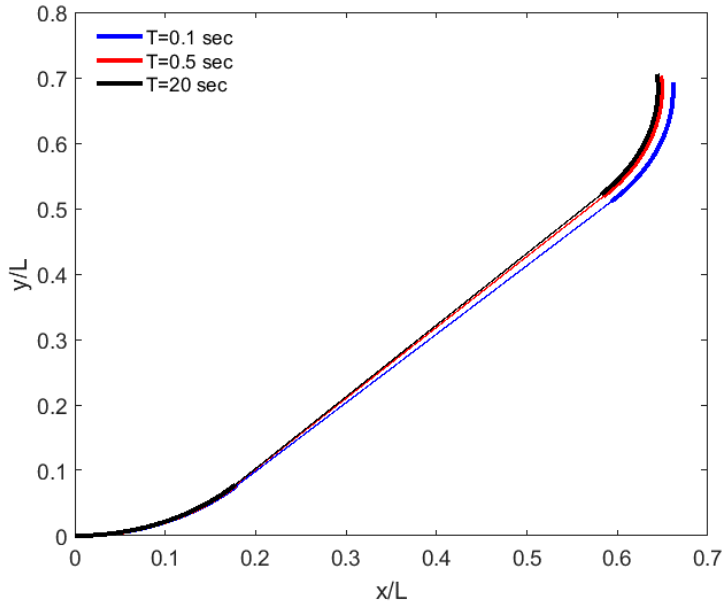

(a)

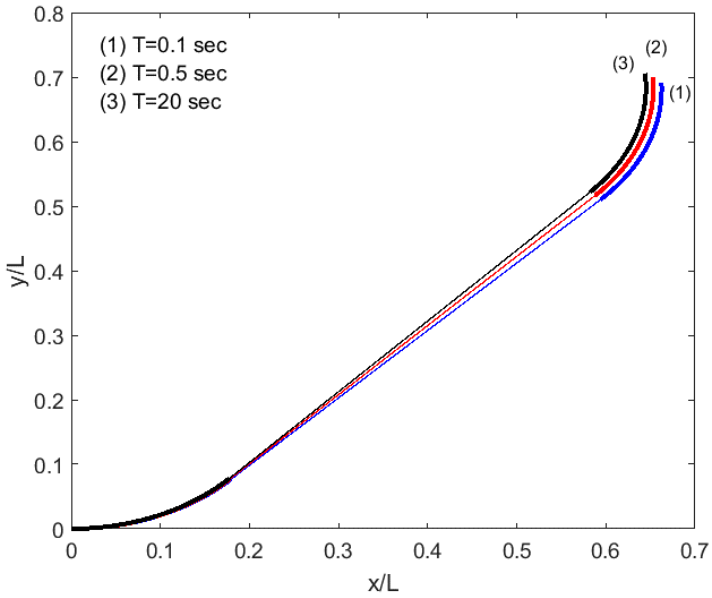

(b)

Figure 2.13. Effect of time-dependent electric field on deformation of a viscoelastic smart beam with two pairs of actuator patches and with τ_0 equals (a) 0.5 sec (b) 2 sec and (c) 20 sec

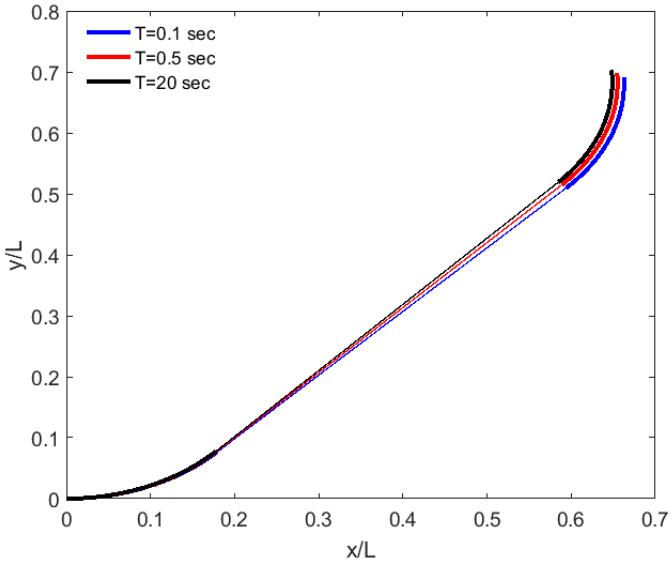

(c)

Figure 2.13. Continued

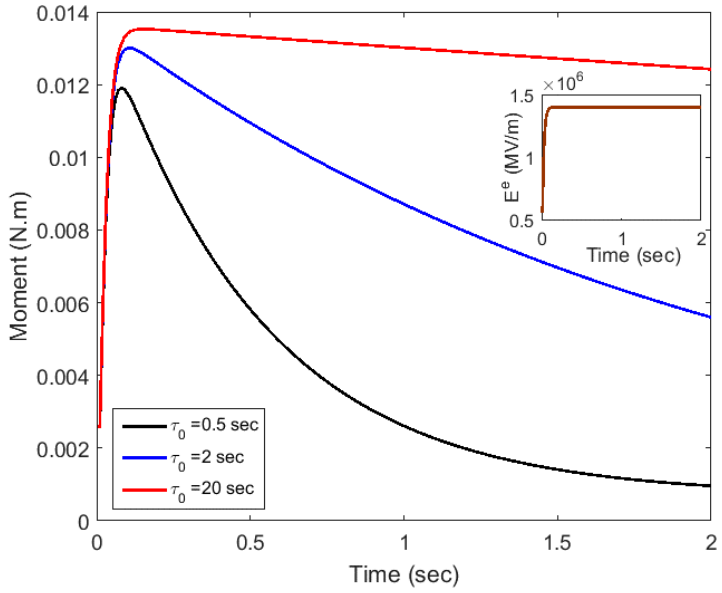

Figure 2.14. Induced moment to the viscoelastic substrate beam with different time characteristics under shown electric stimulus E^e

In Figure 2.15 reconfiguration of another unconstrained beam with two active patches is shown. Changes in the deformation after T>0.1 sec is seen to be negligible with the same reason discussed previously.

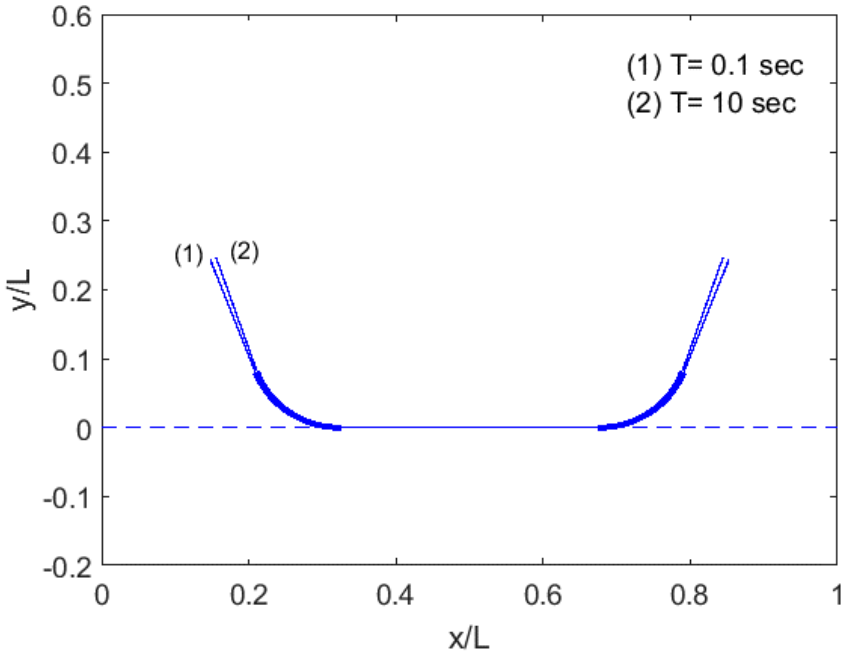

Figure 2.15. Deformation of a free viscoelastic beam with two pairs of active patch

In the next example, configuration of an actuated cantilever beam with two layers of active piezoelectric patches bonded along the length of the structure on top and bottom of it is calculated as shown in Figure 2.16. The relaxation function of the beam and applied electric field are the same as for the previous boundary value problem. As seen and expected similar to before, the shape of viscoelastic structure remains unchanged almost after the electric field input remains constant. It is noted that in the above analyses, only the time-dependent responses of the polymeric substrates are considered while the responses of the active components are time-independent. When different time-dependent responses of the active materials and substrates are considered, different behaviors are expected, which will be shown later in Chapter 4.

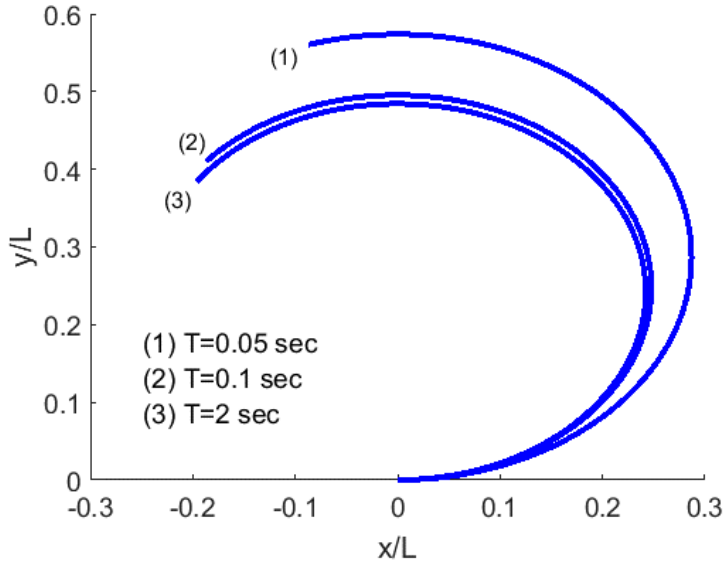

Figure 2.16. Configuration of an originally straight (at T<0) cantilever viscoelastic beam under actuation of two active layers of piezoelectric

3. ANALYSIS OF SMART ELASTIC SHELLS WITH GEOMETRIC NONLINEARITIES

3-1 Deformations of thin shell with distributed piezoelectric actuators

The smart beam analysis presented in the previous chapter is now extended to two-dimensional structures, i.e., slender originally flat planar structures undergoing general three-dimensional shape changes. Dimitriadis et al. [74] estimated the corresponding load induced from the piezoelectric patch to a supporting elastic plate to study linear vibration of simply-supported plates with bonded distributed patches. They considered mainly small deformations structures and used a semi-analytical method based on Fourier series in order to obtain solutions to the governing equations. This study adopts the same approach as in Dimitriadis et al. [64] in terms of determining the induced bending moment from the piezoelectric patches and considers the slender plates undergoing large deformations.

Consider a part of the shell with thickness 2*h*, with integrated actuators as shown in Figure 3.1. Since the patches are assumed perfectly bonded to the elastic isotropic homogeneous shell, the displacements at the interfaces of the shell and the piezoelectric patches are continuous; and due to the differences in the elastic moduli of the patches and substrate, stress discontinuities arise at the interfaces. In this case, the normal strains in the actuators are in the in-plane directions, which are perpendicular to the poling axis of the wafer. The induced stresses and strains at the interfaces are equal in the *x*- and *y*- directions and the resulting stress distributions in the *x*-*z* and *y*-*z* planes are identical. Figure 3.1 represents the *x*-*z* and *y*-*z* stress distributions. Also, it is seen that the stress distributions due to the electric stimulus prescribed on the top and bottom actuators must be anti-symmetric about the neutral axis in order to create bending moments and curvatures.

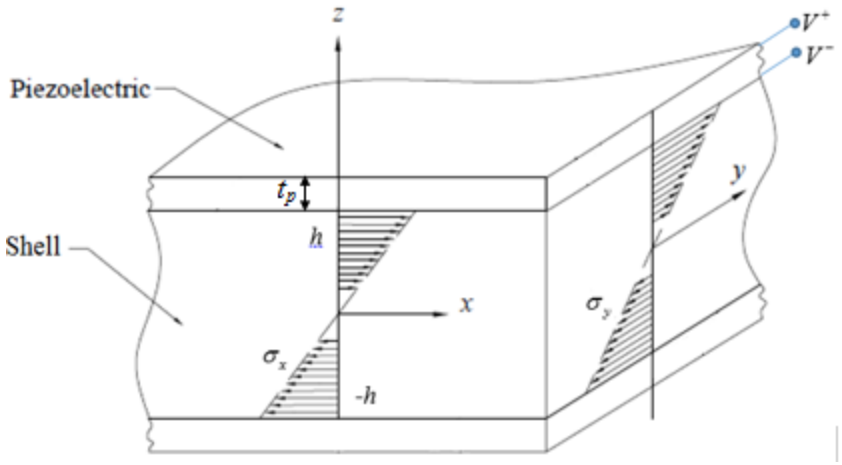

Figure 3.1. Stress distribution in the structure section due to active piezoelectric

Referring to Figure 3.1, the normal stress distribution within the shell results in the couples m_x and m_y per unit length (bending moments):

$$\int_{-h}^{h} \sigma_x z \, dy \, dz = m_x dy$$
$$\int_{-h}^{h} \sigma_y z \, dx \, dz = m_y dx \qquad (3.1)$$

The axial in-plane strain distribution is considered small and varies linearly along the thickness direction and expressed as:

$$\varepsilon_x = z\kappa_x , \quad \varepsilon_y = z\kappa_y \qquad (3.2)$$

where κ_x and κ_y are the curvatures of the neutral surface of the shell parallel to the *x*-*z* and *y*-*z* planes. By considering a linear elastic constitutive model for isotropic material, and equations (3.1) and (3.2), the following moment-curvature expressions are obtained

$$
\begin{aligned}
m_x &= D_{pl}\left(\kappa_x + \nu\kappa_y\right) \\
m_y &= D_{pl}\left(\kappa_y + \nu\kappa_x\right)
\end{aligned}
\tag{3.3}
$$

where D_{pl} is the flexural rigidity of the shell, $2E_{pl}h^3/3(1-\nu^2)$ with E_{pl} denotes the elastic modulus of the shell. The objective is to determine the equivalent edge moments of the actuator patch such that the axial stresses at the surfaces of the shell are equal to the interface stresses of the shell when the patch is activated. The stress-strain relations at the interface for the linear elastic shell is

$$
\begin{aligned}
\left(\sigma_{xi}\right)_{pl} &= \frac{E_{pl}}{1-\nu_{pl}^2}\left(\varepsilon_{xi} + \nu_{pl}\varepsilon_{yi}\right) \\
\left(\sigma_{yi}\right)_{pl} &= \frac{E_{pl}}{1-\nu_{pl}^2}\left(\varepsilon_{yi} + \nu_{pl}\varepsilon_{xi}\right)
\end{aligned}
\tag{3.4}
$$

where the subscript *i* of the stress and strains denotes their measurement at the interface. On the other hand, the stress-strain relations of the actuator at the interface is expressed as

$$
\begin{aligned}
\left(\sigma_{xi}\right)_{p} &= \frac{E_{p}}{1-\nu_{p}^2}\left(\varepsilon_{xi} + \nu_{p}\varepsilon_{yi} - \left(\varepsilon_{x}\right)_{p} - \nu_{p}\left(\varepsilon_{y}\right)_{p}\right) \\
\left(\sigma_{yi}\right)_{p} &= \frac{E_{p}}{1-\nu_{p}^2}\left(\varepsilon_{yi} + \nu_{p}\varepsilon_{xi} - \left(\varepsilon_{y}\right)_{p} - \nu_{p}\left(\varepsilon_{x}\right)_{p}\right)
\end{aligned}
\tag{3.5}
$$

where E_p and ν_p are the elastic modulus and Poisson's ratio of the patch respectively. $\left(\varepsilon_x\right)_p$ and $\left(\varepsilon_y\right)_p$ denote the unconstrained (free) strains in *x*- and *y*- directions, respectively, due to application of electric fields to the piezoelectric patches, which are defined in terms of prescribed electric field in the same way as in the previous chapter as follows

$$\varepsilon_p = d_{13} E^e \tag{3.6-a}$$

$$\varepsilon_p = d_{13} E^e + \frac{1}{2}\beta_{13} E^{e\ 2} + HOT \tag{3.6-b}$$

where the linear electro-mechanical constitutive relation, Eq. (2.7-a), is valid for a relatively small amount of electric field input and the higher order terms of the electric fields are included for relatively large electric field input, Eq. (2.7-b).

Considering a linear distribution of stresses in the thickness direction of the shell and the piezoelectric patches, the expressions for the axial stresses in terms of their magnitude at the interface are

$$\begin{aligned} &\left(\sigma_x\right)_{pl} = \frac{\left(\sigma_{xi}\right)_{pl}}{h} z; \quad \left(\sigma_y\right)_{pl} = \frac{\left(\sigma_{yi}\right)_{pl}}{h} z; \\ &\left(\sigma_x\right)_p = \left(\sigma_{xi}\right)_p - \left(\sigma_{xi}\right)_{pl}\left(1 - \frac{z}{h}\right), \\ &\left(\sigma_y\right)_p = \left(\sigma_{yi}\right)_p - \left(\sigma_{yi}\right)_{pl}\left(1 - \frac{z}{h}\right) \end{aligned} \tag{3.7}$$

From the moment equilibrium about the neutral axis of the shell in *x*- direction,

$$\int_0^h \left(\sigma_x\right)_{pl} z dz + \int_h^{h+t} \left(\sigma_x\right)_p z dz = 0 \tag{3.8}$$

where *t* is thickness of the patch. Substituting Eq. (3.6) and (3.7) into Eq. (3.8) and evaluating the integrals results in

$$\left(\sigma_x\right)_{pl} = \kappa_g \left(\sigma_{xi}\right)_p \tag{3.9}$$

where the geometric parameter k_g is defined as

$$\kappa_g = \frac{3th\left(2h+t\right)}{2\left(h^3+t^3\right)+3ht^2} \tag{3.10}$$

In a similar way, the stress relations at the interface are obtained in *y*- direction.

$$\left(\sigma_y\right)_{pl} = \kappa_g \left(\sigma_{yi}\right)_p \tag{3.11}$$

From Eqs. (3.4) and (3.5) by using the Eqs. (3.9) and (3.11), the expressions for the interface strains are derived as follow:

$$\begin{aligned} \varepsilon_{xi} &= \frac{\left(1-p\right)\gamma_x - \left(\nu_{pl} - \nu_p p\right)\gamma_y}{\left(1-p\right)^2 - \left(\nu_{pl} - \nu_p p\right)^2} \\ \varepsilon_{yi} &= \frac{\left(1-p\right)\gamma_y - \left(\nu_{pl} - \nu_p p\right)\gamma_x}{\left(1-p\right)^2 - \left(\nu_{pl} - \nu_p p\right)^2} \end{aligned} \tag{3.12}$$

where

$$p = \frac{-E_p}{E_{pl}}\left(\frac{1-\nu_{pl}^2}{1-\nu_p^2}\right)\kappa_g \tag{3.13}$$

and

$$\gamma_x = -p\left(\left(\varepsilon_x\right)_p + \nu_p\left(\varepsilon_y\right)_p\right)$$
$$\gamma_y = -p\left(\left(\varepsilon_y\right)_p + \nu_p\left(\varepsilon_x\right)_p\right) \tag{3.14}$$

Substituting Eqs. (3.2) and (3.12) into Eq. (3.3), expressions for the couples m_x and m_y are obtained as follows

$$m_x = \frac{2h^2}{3}\left(\frac{E_{pl}}{1-\nu_{pl}^2}\right)\left(\varepsilon_{xi} + \nu_{pl}\varepsilon_{yi}\right)$$
$$m_y = \frac{2h^2}{3}\left(\frac{E_{pl}}{1-\nu_{pl}^2}\right)\left(\varepsilon_{yi} + \nu_{pl}\varepsilon_{xi}\right) \tag{3.15}$$

3-2 Co-rotational finite element (CRFE) analysis of smart thin shells

In this section, 3-D deformations of smart thin planar structures undergoing small strains but large rotations due to electro-mechanical input are analyzed. The CRFE approach is adopted for obtaining the approximate solutions. The planar structure is considered as geometrically nonlinear shell structures. The co-rotational (CR) formulation is based upon an explicit separation of rigid body motions, including translations and rotations, from the total deformations. The benefit gained through this approach is that an existing linear finite element method is used for the deformational part of motion, while a nonlinear analysis is incorporated for the rigid body motions part.

3-2-1 Kinematics of CR formulation

Consider an individual triangular element deformed to a current configuration as shown in Figure 3.2. The element in its initial configuration is denoted C^0. The motion of the element under an applied load carries it to a deformed configuration C^D. The rigid-body

motion undergone by the element brings the initial configuration to the co-rotated configuration or dashed configuration C^R.

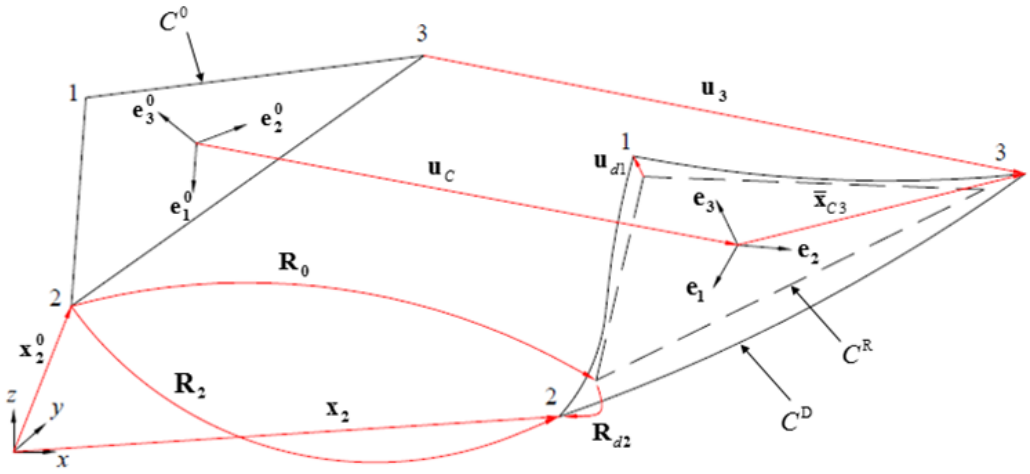

Figure 3.2. Co-rotational element kinematics

Two types of coordinate systems are considered: global coordinate system defined by the triad of unit orthogonal vectors (i, j, k) and local coordinate system of the element including initial coordinate system ($\mathbf{e_1^0}$, $\mathbf{e_2^0}$, $\mathbf{e_3^0}$) and co-rotated coordinate system ($\mathbf{e_1}, \mathbf{e_2}, \mathbf{e_3}$) which is the reference coordinate system for both C^R and C^D. Regarding the notations used for variables, the superscripts 0 and R correspond to the variables at the initial and co-rotated configurations, respectively. Variables without superscript correspond to the deformed configuration. Subscripts correspond to the starting and ending points of the vector. The variables in the local coordinate system are referred by an overbar. When the variable is considered in the global coordinate system, the overbar is omitted. To establish an initial coordinate system of the element, the origin of the coordinate system is selected at the centroid of the triangular element. For the orientation of the coordinate system, the axis $\mathbf{e_1^0}$ is parallel to the side 1-2 of the element, $\mathbf{e_3^0}$ is perpendicular to the element plane determined by the three nodes of the element. In other words, the triad of unit orthogonal vectors of the coordinate system is derived as follows

$$\mathbf{e}_1^0 = \frac{\mathbf{x}_{21}^0}{\left|\mathbf{x}_{21}^0\right|}, \quad \mathbf{e}_3^0 = \frac{\mathbf{x}_{21}^0 \times \mathbf{x}_{31}^0}{\left|\mathbf{x}_{21}^0 \times \mathbf{x}_{31}^0\right|}, \quad \mathbf{e}_2^0 = \mathbf{e}_3^0 \times \mathbf{e}_1^0 \tag{3.16}$$

where $\mathbf{x}_{ba}^0 = \mathbf{x}_b^0 - \mathbf{x}_a^0$, $(a,b = 1,2,3)$ and $\mathbf{x}_a^0$ refers to global position vector of element node *a* in element initial configuration C^0.

A vector **x** in the global coordinate system is related to its expression in the local coordinate as follows

$$\begin{aligned} \bar{\mathbf{x}}^0 &= \mathbf{T}_0 \mathbf{x}, \\ \bar{\mathbf{x}} &= \mathbf{T}\mathbf{x} \end{aligned} \tag{3.17}$$

where $\mathbf{T}_0$ and $\mathbf{T}$ are the transformation tensors of a location in C^0 and C^{D}, from global to local coordinate systems. Based on Eq. (3.1), $\mathbf{T}_0$ is expressed as

$$\mathbf{T}_0 = [\mathbf{e}_1^0 \quad \mathbf{e}_2^0 \quad \mathbf{e}_3^0]^T \tag{3.18}$$

Similar to the initial coordinate system, the co-rotated coordinate system for the co-rotated and deformed configurations of the element are established in terms of global position vectors of the nodes $\mathbf{x}_a$, $(a = 1,2,3)$ in C^{D} and so transformation matrix $\mathbf{T}$ is expressed as

$$\mathbf{T} = [\mathbf{e}_1 \quad \mathbf{e}_2 \quad \mathbf{e}_3]^T \tag{3.19}$$

The position of the C^{R} is obtained through a rigid-body translation $\mathbf{u}_C$ and rigid-body rotation $\mathbf{R_0}$. The rigid body translation $\mathbf{u}_C$ is defined as the displacement of the centroid of the element. The orthogonal rotation matrix $\mathbf{R_0}$ is expressed as

$$\mathbf{R_0} = \mathbf{T}^T \mathbf{T}_0 \tag{3.20}$$

Translation of an element node *a* moves from the initial position $\mathbf{x}_a^0$ to its deformed position $\mathbf{x}_a$ in C^{D} is given by

$$\mathbf{u}_a = \mathbf{x}_a - \mathbf{x}_a^0 \tag{3.21}$$

According to the CR approach, this displacement can be split into rigid-body and deformational components:

$$\mathbf{u}_a = \mathbf{u}_{ra} + \mathbf{u}_{da} \tag{3.22}$$

where

$$\begin{aligned} \mathbf{u}_{ra} &= \mathbf{x}_a^R - \mathbf{x}_a^0 = \mathbf{u}_C + \mathbf{x}_{Ca}^R - \mathbf{x}_{Ca}^0 \\ \mathbf{u}_{da} &= \mathbf{x}_a - \mathbf{x}_a^R \end{aligned} \tag{3.23}$$

where $\mathbf{x}_C^R = \frac{1}{3}\sum_{a=1}^{3} \mathbf{x}_a^R$ and $\mathbf{x}_C^0 = \frac{1}{3}\sum_{a=1}^{3} \mathbf{x}_a^0$ for a triangular element. Thus, the deformational or in this case an elastic translation of the node can be expressed as

$$\mathbf{u}_{da} = \mathbf{u}_a + \mathbf{x}_a^0 - \mathbf{x}_{Ca}^0 - \mathbf{u}_C - \mathbf{x}_{Ca}^R \tag{3.24}$$

In a local coordinate system, the displacement of the deformed body is expressed as

$$\bar{\mathbf{u}}_{da} = \bar{\mathbf{x}}_{Ca} - \bar{\mathbf{x}}_{Ca}^R = \mathbf{T}\mathbf{u}_{da} = \mathbf{T}(\mathbf{u}_a + \mathbf{x}_a^0 - \mathbf{x}_{Ca}^0 - \mathbf{u}_C - \mathbf{x}_{Ca}^R) \tag{3.25}$$

where $\bar{\mathbf{x}}_{Ca} = \bar{\mathbf{x}}_a - \bar{\mathbf{x}}_C$ and the rotation of a node *a* as it moves from its initial position in C^0 to its deformed position in C^{D} can be described by the rotation tensor $\mathbf{R}_a$. As for the translation, $\mathbf{R}_{\mathrm{a}}$ is assumed to be decomposed into a rigid-body rotation $\mathbf{R}_0$ for nodal rotation in $C^0 \rightarrow C^{\mathrm{R}}$ and a deformational rotation $\mathbf{R}_{da}$ as

$$\mathbf{R}_a = \mathbf{R}_{da}\mathbf{R}_0 \tag{3.26}$$

From Eq. (3.5) and (3.11), the deformational rotation in the local coordinate system of C^{R} and C^{D} can be expressed as

$$\bar{\mathbf{R}}_{da} = \mathbf{T}\mathbf{R}_a\mathbf{T}_0^T \tag{3.27}$$

In addition to the rotation matrix **R**, a pseudo-vector $\boldsymbol{\theta}$ is defined in the process of computation. $\boldsymbol{\theta}$ is the rotational pseudo-vector defined as $\boldsymbol{\theta} = \theta\mathbf{n}$ where θ is magnitude of the rotation angle $\theta = \sqrt{\theta_x^2 + \theta_y^2 + \theta_z^2}$ about an axis given by the unit vector *n*. The rotation matrix **R** is a nonlinear function of the rotational pseudo-vector $\boldsymbol{\theta}$. Based on purely geometric analyses [35], a rotation of a vector $\mathbf{r}_0$ through an angle θ about an axis oriented through the unit vector $\mathbf{n}^T = [n_1, n_2, n_3]$ gives a new vector **r** that can be represented as

$$\mathbf{r} = \mathbf{R}\mathbf{r}_0 \text{ where } \mathbf{R}=(\mathrm{I}+\mathbf{N}\sin\theta+\mathbf{N}^2(1-\cos\theta)) \tag{3.28}$$

and

$$\mathbf{N} = \mathrm{spin}(\mathbf{n}) = \begin{pmatrix} 0 & -n_3 & n_2 \\ n_3 & 0 & -n_1 \\ -n_2 & n_1 & 0 \end{pmatrix} \tag{3.29}$$

On the other hand, the pseudo-vector $\boldsymbol{\theta}$ associated with a known $\mathbf{R}$ can be calculated as

$$\boldsymbol{\theta} = \theta\mathbf{n} = \frac{\theta}{2\sin\theta}\begin{Bmatrix} R_{32} - R_{23} \\ R_{13} - R_{31} \\ R_{21} - R_{12} \end{Bmatrix} \tag{3.30}$$

In order to avoid numerical instability in computation, $\theta/\sin\theta$ is set to one for small θ, e.g. $\theta<10^{-8}$ or its truncated Taylor series can be used for, $\theta<10^{-2}$ [42].

The finite element state of the triangular element is described by the nodal translational displacement $\mathbf{u}_a$ and the rotational orientation $\mathbf{R}_a$ of the nodes. Total nodal displacement in the global coordinate system is denoted by an array $\mathbf{d}_a = \langle \mathbf{u}_a \ \ \mathbf{R}_a \rangle$ for a=1, 2, 3. The goal is to establish the deformational nodal displacement array $\mathbf{p}_d$ for the element containing translational and rotational degrees of freedom as expressed below based on the finite displacement state $\mathbf{d}_a$ of the nodes in global coordinate system:

$$\mathbf{p}_d = \{u_{d1}\ \theta_{d1}\ u_{d2}\ \theta_{d2}\ u_{d3}\ \theta_{d3}\}^T \tag{3.31}$$

or in local coordinate system, is given as:

$$\bar{\mathbf{p}}_d = \{\bar{u}_{d1}\ \bar{\theta}_{d1}\ \bar{u}_{d2}\ \bar{\theta}_{d2}\ \bar{u}_{d2}\ \bar{\theta}_{d2}\}^T \tag{3.32}$$

Another quantity used in the CREF approach is a pseudo-vector $\boldsymbol{\omega}$ denoting instantaneous rotation axis about which the rotational angle θ is measured. In order to solve for the nonlinear finite element equations with iterative methods, the iterative incremental solutions represent the superposition additional infinitesimal incremental rotation $\delta\bar{\boldsymbol{\omega}}_{da}$ on the basis of finite rotation of the node expressed by pseudo-vector $\bar{\boldsymbol{\theta}}_{da}$. The incremental rotation $\delta\bar{\boldsymbol{\omega}}_{da}$ is related to $\delta\bar{\boldsymbol{\theta}}_{da}$ as follows

$$\delta\bar{\boldsymbol{\theta}}_{da} = \mathbf{H}(\bar{\boldsymbol{\theta}}_{da})\delta\bar{\boldsymbol{\omega}}_{da} \tag{3.33}$$

where

$$\mathbf{H}(\bar{\boldsymbol{\theta}}_{da}) = \frac{\partial\bar{\boldsymbol{\theta}}_{da}}{\partial\bar{\boldsymbol{\omega}}_{da}} = \mathbf{I}_3 - \frac{1}{2}\mathrm{spin}(\bar{\boldsymbol{\theta}}_{da}) + \eta\mathrm{spin}(\bar{\boldsymbol{\theta}}_{da})^2 \tag{3.34}$$

$\mathbf{I}_3$ is 3×3 identity matrix,

$$\mathrm{spin}(\bar{\boldsymbol{\theta}}_{da}) = \begin{pmatrix} 0 & -\bar{\theta}_{daz} & \bar{\theta}_{day} \\ \bar{\theta}_{daz} & 0 & -\bar{\theta}_{dax} \\ -\bar{\theta}_{day} & \bar{\theta}_{dax} & 0 \end{pmatrix}, \tag{3.35}$$

and

$$\eta = \frac{1 - \frac{1}{2}\bar{\theta}_{da}\cot\left(\frac{1}{2}\bar{\theta}_{da}\right)}{\bar{\theta}_{da}^{\,2}} \tag{3.36}$$

Again, for maintaining a numerical stability, for small $\bar{\theta}_{da}$, say $\bar{\theta}_{da} \le 3^{\circ}$, truncated Taylor series of η is used:

$$\eta = \frac{1}{12} + \frac{1}{720}\bar{\theta}_{da}^{\,2} + \frac{1}{30240}\bar{\theta}_{da}^{\,4} + \frac{1}{1209600}\bar{\theta}_{da}^{\,6} + \ldots \tag{3.37}$$

Equation (3.33) is used in order to update the rotational degree of freedom in the solution process by transforming from $\delta\bar{\boldsymbol{\omega}}_{da}$ to $\delta\bar{\boldsymbol{\theta}}_{da}$. Also, the increment of the total displacements of a node *a* is expressed by $\delta\mathbf{d}_a = \{\delta\mathbf{u}_a^T \;\; \delta\boldsymbol{\omega}_a^T\}^T$ while the total nodal displacements is represented as $\mathbf{d}_a = \langle \mathbf{u}_a \;\; \mathbf{R}_a \rangle$, (*a*=1, 2, 3) as mentioned before. $\delta\boldsymbol{\omega}_a$ also refers to an instantaneous rotation axis of the node *a*. To update the total rotation of the node *a*, at the end of each increment based on the derived incremental rotation pseudo-vector $\delta\boldsymbol{\omega}_a$, the following formula is used:

$$\mathbf{R}_{a,new} = \mathbf{R}(\delta\boldsymbol{\omega}_a)\mathbf{R}_{a,old} \tag{3.38}$$

where

$$\begin{aligned} \mathbf{R}(\delta\boldsymbol{\omega}_a) &= I_3 + \frac{\sin(\delta\omega_a)}{\delta\omega_a}\,\mathrm{spin}(\delta\omega_a) + \frac{1}{2}\left[\frac{\sin(\delta\omega_a/2)}{\delta\omega_a/2}\right]^2 \mathrm{spin}(\delta\omega_a)^2 \\ \delta\omega_a &= \sqrt{\delta\omega_{ax} + \delta\omega_{ay} + \delta\omega_{az}} \end{aligned} \tag{3.39}$$

In order to avoid numerical instability, power series expansion of $\sin(\delta\omega_a)/\delta\omega_a$ and ($\sin(\delta\omega_a)/\delta\omega_a)^2$ can be used for $\delta\omega_a \le 3^\circ$.

3-2-2 Internal force and tangent stiffness

In the co-rotated coordinate system of the element, the deformational displacement vector $\bar{\mathbf{p}}_d$, Eq. (3.32), is related to the element internal force $\bar{\mathbf{f}}$ and local element stiffness matrix $\bar{\mathbf{K}}$ in a linearized form as follows

$$\bar{\mathbf{f}} = \bar{\mathbf{K}}\bar{\mathbf{p}}_d \tag{3.40}$$

where the vector $\bar{\mathbf{p}}_d$ is expressed in Eq. (3.32) and by denoting the internal forces and moments at each node *a* as $\bar{\mathbf{n}}_a$ and $\bar{\mathbf{m}}_a$ respectively, $\bar{\mathbf{f}}$ is written as

$$\bar{\mathbf{f}} = [\bar{\mathbf{n}}_1^T \;\; \bar{\mathbf{m}}_1^T \;\; \bar{\mathbf{n}}_2^T \;\; \bar{\mathbf{m}}_2^T \;\; \bar{\mathbf{n}}_3^T \;\; \bar{\mathbf{m}}_3^T] \tag{3.41}$$

It should be noted that Eq. (3.40) describes the deformation with respect to C^R in local coordinate system, and $\bar{\mathbf{f}}$ and $\bar{\mathbf{K}}$ are computed based on small deformations. However, with respect to C^0 in the global coordinate system we deal with nonlinear equations as the internal force of the element is nonlinear in terms of displacements and the transformation matrices between the local and global coordinate systems depend on the displacement vector corresponding to large rotation effects. In the global coordinate system, the linearized relation between the tangent stiffness matrix $\mathbf{K}_T$ of the element and its internal force vector is

$$\delta\mathbf{f} = \mathbf{K}_T\delta\mathbf{d} \tag{3.42}$$

where $\mathbf{d}$ is the vector of total displacement.

In order to derive $\mathbf{K}_T$ of the element, a relationship between the variation of the total displacement $\delta\mathbf{d}$ in global coordinate system and deformational displacement $\delta\bar{\mathbf{p}}_d$ in local coordinate system should be first obtained. For the element, the variation of $\delta\bar{\mathbf{p}}_d = \{\delta\bar{\mathbf{u}}_d^T \;\; \delta\bar{\boldsymbol{\theta}}_d^T\}^T$ in terms of $\delta\bar{\mathbf{d}}_d = \{\delta\bar{\mathbf{u}}_d^T \;\; \delta\bar{\boldsymbol{\omega}}_d^T\}^T$ is [37]

$$\delta\bar{\mathbf{p}}_d = \mathbf{H}\delta\bar{\mathbf{d}}_d \tag{3.43}$$

where

$$\bar{\mathbf{H}} = \text{diag}\left[\mathbf{I}_3 \;\; \bar{\mathbf{H}}_1 \;\; \mathbf{I}_3 \;\; \bar{\mathbf{H}}_2 \;\; \mathbf{I}_3 \;\; \bar{\mathbf{H}}_3\right] \tag{3.44}$$

is composed of submatrices $\mathbf{I}_3$ and nodal submatrices $\bar{\mathbf{H}}_a = \bar{\mathbf{H}}_a(\bar{\boldsymbol{\theta}}_{da})$ $(a = 1,2,3)$ as in Eq. (3.34). For each node of the element, *a*, the variation of its deformational displacement vector $\delta\bar{\mathbf{d}}_{da}$ is expressed as [42]

$$\delta\bar{\mathbf{d}}_{da} = \sum_{b=1}^{3}\bar{\mathbf{P}}_{ab}\delta\bar{\mathbf{d}}_b\,,\;\; \bar{\mathbf{P}}_{ab} = \begin{pmatrix} \mathbf{U}_{ab} + \bar{\mathbf{S}}_a\bar{\mathbf{G}}_{u,b} & 0_3 \\ -\bar{\mathbf{G}}_{u,b} & \delta_{ab}\mathbf{I}_3 \end{pmatrix} \tag{3.45}$$

where

$$\mathbf{U}_{ab} = \left(\delta_{ab} - \frac{1}{3}\right)\mathbf{I}_3\,,\;\; \bar{\mathbf{S}}_a = \text{spin}(\bar{\mathbf{x}}_a) \tag{3.46}$$

$\bar{\mathbf{G}}_{u,b}$ is the gradient of incremental rigid-body rotation of the element with respect to the nodal displacement vector for node *b* in local coordinate system. At each node, $\bar{\mathbf{G}}_{u,b}$ is defined as

$$\bar{\mathbf{G}}_{u,1}=\frac{1}{2A}\begin{pmatrix}0 & 0 & \bar{x}_{23}\\ 0 & 0 & \bar{y}_{23}\\ 0 & -2A/l_{12} & 0\end{pmatrix},\ \bar{\mathbf{G}}_{u,2}=\frac{1}{2A}\begin{pmatrix}0 & 0 & \bar{x}_{13}\\ 0 & 0 & \bar{y}_{13}\\ 0 & -2A/l_{12} & 0\end{pmatrix},\ \bar{\mathbf{G}}_{u,3}=\frac{1}{2A}\begin{pmatrix}0 & 0 & \bar{x}_{21}\\ 0 & 0 & \bar{y}_{21}\\ 0 & 0 & 0\end{pmatrix} \tag{3.47}$$

where *A* is area of the element and $\bar{x}_{ij}=\bar{x}_i-\bar{x}_j$, $\bar{y}_{ij}=\bar{y}_i-\bar{y}_j$ $(i,j=1,2,3)$ in which $\bar{x}$ and $\bar{y}$ are the local coordinates of the element nodes.

The derivation of $\bar{\mathbf{P}}_{ab}$ is explained in details in [37, 40] and is not repeated here. $\bar{\mathbf{P}}_{ab}$ is the submatrix of the projector matrix $\bar{\mathbf{P}}$ which is one of the main auxiliary matrices in the CR formulation to extract deformational translations and rotations from the total translations and rotations of the element. Thus, for an element,

$$\delta\bar{\mathbf{d}}_d=\bar{\mathbf{P}}\delta\bar{\mathbf{d}} \tag{3.48}$$

From Eq. (3.42) and (3.47),

$$\delta\bar{\mathbf{p}}_d=\bar{\mathbf{H}}\bar{\mathbf{P}}\delta\bar{\mathbf{d}}=\bar{\mathbf{H}}\bar{\mathbf{P}}\mathbf{T}_{el}\delta\mathbf{d} \tag{3.49}$$

where $\mathbf{T}_{el}$ is composed of transformation submatrices **T** given in Eq. (3.19) as follows:

$$\mathbf{T}_{el}=\mathrm{diag}[\mathbf{T}\ \mathbf{T}\ \mathbf{T}\ \mathbf{T}\ \mathbf{T}\ \mathbf{T}] \tag{3.50}$$

The next step is to obtain the tangent stiffness of the element $\mathbf{K}_T$ by taking variation of the global internal force of the element $\mathbf{f}$. Based on the virtual work invariance due to a rigid body motion

$$\delta \mathbf{d}^T \mathbf{f} = \delta \bar{\mathbf{p}}_d^T \bar{\mathbf{f}} \tag{3.51}$$

Thus, using Eq. (3.49), the global internal force can be written as

$$\mathbf{f} = \mathbf{T}_{el}^T \bar{\mathbf{P}}^T \bar{\mathbf{H}}^T \bar{\mathbf{f}} \tag{3.52}$$

Taking the variation of f results in

$$\begin{aligned} \delta \mathbf{f} &= \delta \mathbf{T}_{el}^T \bar{\mathbf{P}}^T \bar{\mathbf{H}}^T \bar{\mathbf{f}} + \mathbf{T}_{el}^T \delta \bar{\mathbf{P}}^T \bar{\mathbf{H}}^T \bar{\mathbf{f}} + \mathbf{T}_{el}^T \bar{\mathbf{P}}^T \delta \bar{\mathbf{H}}^T \bar{\mathbf{f}} + \mathbf{T}_{el}^T \bar{\mathbf{P}}^T \bar{\mathbf{H}}^T \delta \bar{\mathbf{f}} \\ &= \underbrace{(\mathbf{K}_{GR} + \mathbf{K}_{GP} + \mathbf{K}_{GM} + \mathbf{K}_M)}_{\mathbf{K}_T} \delta \mathbf{d} \end{aligned} \tag{3.53}$$

As seen, the tangent stiffness of the element in the global coordinate system includes four terms. The first three terms, $\mathbf{K}_{GR} + \mathbf{K}_{GP} + \mathbf{K}_{GM}$, are the components of geometric stiffness, $\mathbf{K}_G$, and the fourth term $\mathbf{K}_M$ is known as material stiffness. Here, the calculation of each term in details is presented in [37] and here only the results and expression for each term is presented. $\mathbf{K}_{GR}$ is the rotational geometric stiffness expressed as

$$\mathbf{K}_{GR} = -\mathbf{T}_{el}^T \bar{\mathbf{F}}_{nm} \bar{\mathbf{G}} \mathbf{T}_{el} \tag{3.54}$$

where

$$\bar{\mathbf{G}} = \left[\bar{\mathbf{G}}_{u,1}\ \mathbf{0}_3\ \bar{\mathbf{G}}_{u,2}\ \mathbf{0}_3\ \bar{\mathbf{G}}_{u,3}\ \mathbf{0}_3\right],$$
$$\bar{\mathbf{F}}_{nm} = [\text{spin}(\bar{\mathbf{n}}_{p,1})^T\ \text{spin}(\bar{\mathbf{m}}_{p,1})^T \ldots \text{spin}(\bar{\mathbf{n}}_{p,3})^T\ \text{spin}(\bar{\mathbf{n}}_{p,3})^T]^T \tag{3.55}$$

where $\bar{\mathbf{n}}_{p,a}$ and $\bar{\mathbf{m}}_{p,a}$ are the force and moment components of vector $\bar{\mathbf{f}}_p = \bar{\mathbf{P}}^T\bar{\mathbf{H}}^T\bar{\mathbf{f}}$. K_{GP} is the equilibrium projection geometric stiffness expressed as

$$\mathbf{K}_{GP} = -\mathbf{T}_{el}^T\bar{\mathbf{G}}^T\bar{\mathbf{F}}_n{}^T\bar{\mathbf{P}}\mathbf{T}_{el} \tag{3.56}$$

where

$$\bar{\mathbf{F}}_n = [\text{spin}(\bar{\mathbf{n}}_{p,1})^T\ \mathbf{0}_3\ \text{spin}(\bar{\mathbf{n}}_{p,2})^T\ \mathbf{0}_3\ \text{spin}(\bar{\mathbf{n}}_{p,3})^T\ \mathbf{0}_3]^T \tag{3.57}$$

$\mathbf{K}_{GM}$ is the moment-correction geometric stiffness due to variation of *H* and expressed as

$$\mathbf{K}_{GP} = \mathbf{T}_{el}^T\bar{\mathbf{P}}^T\bar{\mathbf{L}}\bar{\mathbf{P}}\mathbf{T}_{el} \tag{3.58}$$

where

$$\mathbf{L} = \text{diag}[\mathbf{0}_3\ \bar{\mathbf{L}}_1\ \mathbf{0}_3\ \bar{\mathbf{L}}_2\ \mathbf{0}_3\ \bar{\mathbf{L}}_3]^T \tag{3.59}$$

where the nodal submatrix $\bar{L}_a$ is

$$\bar{\mathbf{L}}_a = \left\{ \eta\left(\bar{\boldsymbol{\theta}}_{da} \bar{\mathbf{m}}_a \mathbf{I}_3 + \bar{\boldsymbol{\theta}}_{da} \bar{\mathbf{m}}_a^T - 2\bar{\mathbf{m}}_a \bar{\boldsymbol{\theta}}_{da}^T \right) + \mu \text{spin}(\bar{\boldsymbol{\theta}}_{da})^2 \bar{\mathbf{m}}_a \bar{\boldsymbol{\theta}}_{da}^T - \frac{1}{2}\text{spin}(\mathbf{m}_a) \right\} \bar{\mathbf{H}}(\bar{\boldsymbol{\theta}}_{da})$$
$$\mu = \frac{d\eta / d\bar{\theta}_{da}}{\bar{\theta}_{da}} \tag{3.60}$$

η is defined already in Eq.(3.36) and Eq.(3.37). The material stiffness matrix is obtained by congruential transformation of the local stiffness to the global frame:

$$\mathbf{K}_M = \mathbf{T}_{el}{}^T \bar{\mathbf{P}}^T \bar{\mathbf{H}}^T \bar{\mathbf{K}} \bar{\mathbf{H}} \bar{\mathbf{P}} \mathbf{T}_{el} \tag{3.61}$$

In summary, the following expression gives the tangent stiffness of the element in the global coordinate system:

$$\mathbf{K}_T = \mathbf{T}_{el}{}^T \left(\bar{\mathbf{P}}^T \bar{\mathbf{H}}^T \bar{\mathbf{K}} \bar{\mathbf{H}} \bar{\mathbf{P}} + \bar{\mathbf{P}}^T \bar{\mathbf{L}} \bar{\mathbf{P}} - \bar{\mathbf{G}}^T \bar{\mathbf{F}}_n{}^T \bar{\mathbf{P}} - \bar{\mathbf{F}}_{nm} \bar{\mathbf{G}} \right) \mathbf{T}_{el} \tag{3.62}$$

Also, by transforming the local internal stiffness of the element to the global frame, we can calculate the displacement components from Eq. (3.42)

$$\mathbf{f} = \mathbf{T}_{el}^T \bar{\mathbf{P}}^T \bar{\mathbf{H}}^T \bar{\mathbf{f}} \tag{3.63}$$

3-3 Flat triangular shell element

The element used in this study is three-node linear flat shell element with six degree of freedom per node obtained by combining the Discrete Kirchhoff Theory (DKT) plate bending element [75] and optimal (OPT) membrane element [76] which includes drilling (in-plane rotation) degree of freedom.

3-3-1 Plate bending element stiffness

The configuration of the element with its nodal degrees of freedom is shown in Figure 3.3. The formulation of the element [75, 77] is based on the discrete Kirchhoff theory for bending of thin plates with considering transverse shear deformations. However, in this study, the transverse shear deformation is neglected and the Kirchhoff hypothesis is introduced in a discrete way along the edges of the element to relate the rotational degrees of freedom to the transverse displacements. The explicit form of the stiffness of each element is presented here:

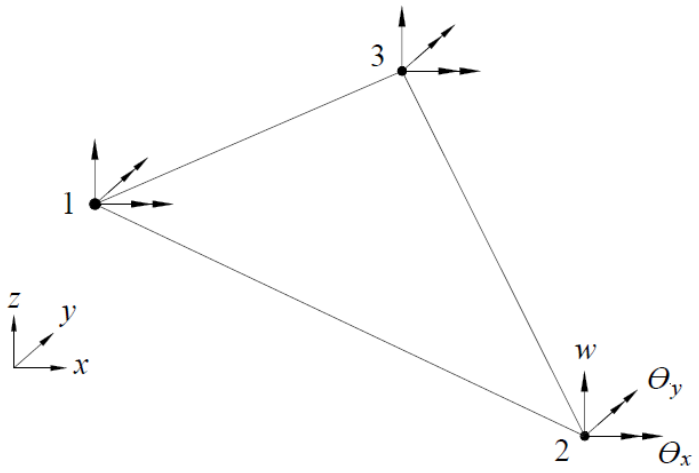

Figure 3.3. Triangular plate bending element with its degrees of freedom

As seen, schematically, in figure 3.3, the nodal displacement vector including degrees of freedom of the element is

$$\mathbf{U} = \left[u_{z1} \;\; \theta_{x1} \;\; \theta_{y1} \;\; u_{z2} \;\; \theta_{x2} \;\; \theta_{y2} \;\; u_{z3} \;\; \theta_{x3} \;\; \theta_{y3} \right]^T \tag{3.64}$$

The stiffness of the optimal plate element is obtained as follows

$$\mathbf{K}_{DKT} = 2A\int_0^1 \int_0^{1-\eta} \mathbf{B}^T \mathbf{D}\mathbf{B} \tag{3.65}$$

where A is area of the element and ξ and η are the in-plane components of the isoparametric area coordinates. **B** is the strain-displacement transformation matrix defined as

$$\mathbf{B}(\xi,\eta) = \frac{1}{2A}\begin{bmatrix} y_{31}\mathbf{H}^T_{x,\xi} + y_{12}\mathbf{H}^T_{x,\eta} \\ -x_{31}\mathbf{H}^T_{\mathrm{y},\xi} - x_{12}\mathbf{H}^T_{\mathrm{y},\eta} \\ -x_{31}\mathbf{H}^T_{\mathrm{x},\xi} - x_{12}\mathbf{H}^T_{\mathrm{x},\eta} + y_{31}\mathbf{H}^T_{\mathrm{y},\xi} + y_{12}\mathbf{H}^T_{\mathrm{y},\eta} \end{bmatrix} \tag{3.66}$$

where

$$\mathbf{H}_{x,\xi} = \begin{Bmatrix} p_4(1-2\xi) + (p_6 - p_4)\eta \\ q_4(1-2\xi) - (q_6 + q_4)\eta \\ -4 + 6(\xi+\eta) + r_4(1-2\xi) - \eta(r_6 + r_4) \\ -p_4(1-2\xi) + \eta(p_5 + p_4) \\ -q_4(1-2\xi) - \eta(q_4 - q_5) \\ -2 + 6\xi + r_4(1-2\xi) + \eta(r_5 - r_4) \\ -\eta(p_6 + p_5) \\ \eta(q_5 - q_6) \\ -\eta(r_6 - r_5) \end{Bmatrix}, \tag{3.67-a}$$

$$\mathbf{H}_{x,\eta}=\begin{Bmatrix} -p_6(1-2\eta)-(p_4-p_6)\xi \\ q_6(1-2\eta)-(q_6+q_4)\xi \\ -4+6(\xi+\eta)+r_6(1-2\eta)-\xi(r_6+r_4) \\ \xi(p_4+p_5) \\ \xi(q_5-q_4) \\ -\xi(r_4-r_5) \\ p_6(1-2\eta)-\xi(p_5+p_6) \\ q_6(1-2\eta)+\xi(q_5-q_6) \\ -2+6\eta+r_6(1-2\eta)+\xi(r_5-r_6) \end{Bmatrix}, \tag{3.67-b}$$

$$\mathbf{H}_{y,\xi}=\begin{Bmatrix} t_4(1-2\xi)+(t_6-t_4)\eta \\ 1+r_4(1-2\xi)-(r_6+r_4)\eta \\ -q_4(1-2\xi)+\eta(q_6+q_4) \\ -t_4(1-2\xi)+\eta(t_4+t_5) \\ -1+r_4(1-2\xi)+\eta(r_5-r_4) \\ -q_4(1-2\xi)+\eta(q_4-q_5) \\ -\eta(t_6+t_5) \\ \eta(r_5-r_6) \\ \eta(q_6-q_5) \end{Bmatrix}, \tag{3.67-c}$$

$$\mathbf{H}_{y,\eta}=\begin{Bmatrix} -t_6(1-2\eta)-(t_4-t_6)\xi \\ 1+r_6(1-2\eta)-(r_6+r_4)\xi \\ q_6(1-2\eta)+\xi(q_6+q_4) \\ \xi(t_4+t_5) \\ \xi(r_5-r_4) \\ \xi(q_5-q_4) \\ t_6(1-2\eta)-\xi(t_5+t_6) \\ -1+r_6(1-2\eta)+\xi(r_5-r_6) \\ -q_6(1-2\eta)-\xi(q_5-q_6) \end{Bmatrix}, \tag{3.67-d}$$

with

$$
\begin{aligned}
&p_k = -6x_{ij} / l_{ij}^2; \quad t_k = -6y_{ij} / l_{ij}^2; \\
&q_k = 3x_{ij}y_{ij} / l_{ij}^2; \quad r_k = 3y_{ij}^2 / l_{ij}^2; \\
&k = 4,5,6 \text{ for } ij = 12,23,31, \text{ respectively}
\end{aligned} \tag{3.68}
$$

Finally, the bending rigidity matrix $\mathbf{D}$ for a linear elastic plate is obtained as follows

$$
\mathbf{D} = \int_{-t/2}^{t/2} \mathbf{E}\, z^2 dz \tag{3.69}
$$

where t is element thickness and $\mathbf{E}$ is the elasticity (material stiffness) tensor.

3-3-2 Membrane triangular element stiffness

The configuration of the membrane element with its nodal degrees of freedom is shown in Figure 3.3. In order to establish the membrane (plane stress) element and derive its elemental stiffness, the assumed natural deviatoric strain formulation (ANDES) discussed in [78] is adopted. The derivation of the stiffness is based on the natural strains, which are the normal strains in the in-plane directions measured along the sides of the triangular element. The element stiffness is composed of two parts: 1) basic stiffness which takes care of consistency in terms of force-moment equilibrium equations and their conjugate displacements and rotations and 2) higher order stiffness which takes care of accuracy and stability (rank sufficiency) of the solutions. To construct the higher order stiffness, deviatoric natural strain components are used. Here, deviatoric means change from the constant strain state and the natural strains are measured along the side direction of triangular element.

The reasons to consider drilling degree of freedom (in-plane rotational degree of freedom) are to improve the performance of the element in terms of numerical aspects like mesh sensitivity, avoiding singularity in the tangent stiffness matrix and model construction without adding midside nodes and so keeping the model and mesh preparation simple and it simplifies the treatment of the shell intersections and also connection of shells to beam

elements in discretizing a domain which includes joints of beam and shell structures. Here, the explicit form of the membrane stiffness is presented. Details of its derivations can be found in [76, 79].

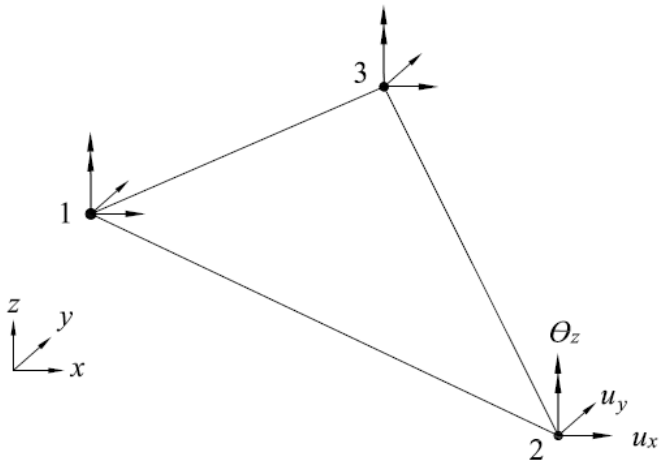

Figure 3.4. Membrane triangular element with its degrees of freedom

As seen in figure 3.4, the nodal displacement vector including degrees of freedom of the element is

$$\mathbf{U} = \left[u_{x1} \;\; u_{y1} \;\; \theta_1 \;\; u_{x2} \;\; u_{y2} \;\; \theta_2 \;\; u_{x3} \;\; u_{y3} \;\; \theta_3 \right]^T \tag{3.70}$$

The stiffness of the optimal membrane element is expressed as [76]

$$\mathbf{K} = \frac{t}{A}\mathbf{LEL}^T + \frac{3}{4}\beta_0 \tilde{\mathbf{T}}_\theta^{\,T} \mathbf{K}_\theta \tilde{\mathbf{T}}_\theta \tag{3.71}$$

where **L** is the element lumping matrix defined as [79]

$$\mathbf{L}=[\mathbf{L}_1,\mathbf{L}_2,\mathbf{L}_3]^T \text{ with } \mathbf{L}_j=\frac{1}{2}\begin{pmatrix} y_{ki} & 0 & -x_{ki} \\ 0 & -x_{ki} & y_{ki} \\ \frac{1}{4}\left(y_{ij}^2-y_{kj}^2\right) & \frac{1}{4}\left(x_{ij}^2-x_{kj}^2\right) & \frac{1}{2}\left(x_{kj}y_{kj}-x_{ij}y_{ij}\right) \end{pmatrix} \tag{3.72}$$

in expression of L_j, the nodal indices (i, j, k) take cyclic permutations of (1, 2, 3);

$$\beta_0=\min\left\{0.5(1-4\nu^2),\ 0.01\right\},\ \nu:\text{Poisson's ratio}$$

$$\tilde{\mathbf{T}}_\theta=\frac{1}{4A}\begin{bmatrix} x_{32} & y_{32} & 4A & x_{13} & y_{13} & 0 & x_{21} & y_{21} & 0 \\ x_{32} & y_{32} & 0 & x_{13} & y_{13} & 4A & x_{21} & y_{21} & 0 \\ x_{32} & y_{32} & 0 & x_{13} & y_{13} & 0 & x_{21} & y_{21} & 4A \end{bmatrix}, \tag{3.73}$$

and

$$\mathbf{K}_\theta=t\left(\mathbf{Q}_1^T\mathbf{T}_{st}^T\mathbf{E}\mathbf{T}_{st}\mathbf{Q}_1+\mathbf{Q}_2^T\mathbf{T}_{st}^T\mathbf{E}\mathbf{T}_{st}\mathbf{Q}_2+\mathbf{Q}_3^T\mathbf{T}_{st}^T\mathbf{E}\mathbf{T}_{st}\mathbf{Q}_3\right) \tag{3.74}$$

where

$$\mathbf{Q}_1=\frac{A}{3}\begin{pmatrix} \frac{-1}{l_{21}^2} & \frac{1}{l_{21}^2} & 0 \\ \frac{1}{l_{32}^2} & \frac{2}{l_{32}^2} & \frac{1}{l_{32}^2} \\ \frac{-2}{l_{13}^2} & \frac{-1}{l_{13}^2} & \frac{-1}{l_{13}^2} \end{pmatrix},\ \mathbf{Q}_2=\frac{A}{3}\begin{pmatrix} \frac{-1}{l_{21}^2} & \frac{-2}{l_{21}^2} & \frac{-1}{l_{21}^2} \\ 0 & \frac{-1}{l_{32}^2} & \frac{1}{l_{32}^2} \\ 0 & \frac{1}{l_{13}^2} & \frac{3}{l_{13}^2} \end{pmatrix},\ \mathbf{Q}_3=\frac{A}{3}\begin{pmatrix} \frac{2}{l_{21}^2} & \frac{1}{l_{21}^2} & \frac{1}{l_{21}^2} \\ \frac{-1}{l_{32}^2} & \frac{-1}{l_{32}^2} & \frac{-2}{l_{32}^2} \\ 0 & 0 & 0 \end{pmatrix},$$

$$\mathbf{T}_{st}=\frac{1}{4A^2}\begin{pmatrix} y_{23}y_{13}{l_{21}}^2 & y_{31}y_{21}{l_{32}}^2 & y_{12}y_{32}{l_{13}}^2 \\ x_{23}x_{13}{l_{21}}^2 & x_{31}x_{21}{l_{32}}^2 & x_{12}x_{32}{l_{13}}^2 \\ (y_{23}x_{31}+x_{32}y_{13}){l_{21}}^2 & (y_{31}x_{12}+x_{13}y_{21}){l_{32}}^2 & (y_{12}x_{23}+x_{21}y_{32}){l_{13}}^2 \end{pmatrix}, \tag{3.75}$$

$$l_{ij}=\sqrt{x_{ij}^2+y_{ij}^2}$$

3-4 Solution procedure

By defining the internal force and tangent stiffness of each element of the structure in the global frame, the structural tangent stiffness $\mathbf{K}_{St}$ and internal force $\mathbf{F}_{St}$ are obtained. The Newton-Raphson iterative algorithm with load control is adopted to determine the displacement solution of the structure under applied loads. Briefly, due to nonlinearity of the problem, the solution obtained by an increment-iterative process is as follows: Consider the equilibrium point of the structure after *n* load steps with known equilibrated displacement solution $\mathbf{U}^{(n)}$, structural tangent stiffness $\mathbf{K}_{St}^{(n)}$ and internal force $\mathbf{F}_{St}^{(n)}$ in the first iteration of $(n+1)^{\text{th}}$ increment, the following equation is considered as the predictor:

$$\delta\mathbf{U}_{(1)}^{(n+1)} = \left(\mathbf{K}_{St(1)}^{(n+1)}\right)^{-1}\left(\lambda^{(n+1)}\mathbf{F}_{ext}\right) \tag{3.76}$$

where $\delta\mathbf{U}_{(1)}^{(n+1)}$ is the initial guess of the structure's incremental displacement by using $\mathbf{K}_{St}^{(n)}$ at the end of n^{th} increment as the trial for tangent stiffness $\mathbf{K}_{St}^{(n+1)}$ due to the $(n+1)^{\text{th}}$ incremental load $\lambda^{(n+1)}\mathbf{F}_{ext}$; $\mathbf{F}_{ext}$ is the total external load applied to the structure and $\lambda^{(n+1)}$ is the load factor of the $(n+1)^{\text{th}}$ load step. The subscripts and superscripts in the parentheses stand for the iteration number and increment number, respectively.

The solution is updated as $\mathbf{U}^{(n+1)} = \mathbf{U}^{(n)} + \delta\mathbf{U}_{(1)}^{(n+1)}$ and then, the tangent stiffness and internal force of the structure is updated. Starting from the 2^{nd} iteration, the following equation is solved for each iteration (*i*)

$$\delta\mathbf{U}_{(i)}^{(n+1)} = \left(\mathbf{K}_{St(i)}^{(n+1)}\right)^{-1}\left(\lambda^{(n+1)}\mathbf{F}_{ext} - \mathbf{F}_{St(i)}\right) \tag{3.77}$$

and as for the first iteration, $\mathbf{U}^{(n+1)}$ is updated and $\mathbf{K}_{St}^{(n+1)}$ and $\mathbf{F}_{St}$ are calculated for next iteration. This process is repeated until iteration convergence criterion is met. The criterion in this study is considered as

$$\frac{\left\|\delta\mathbf{U}_{(i+1)}^{(n+1)}\right\|}{\left\|\mathbf{U}^{(n+1)}\right\|} \leq 10^{-3} \tag{3.78}$$

To improve the computational efficiency, the load control strategy is adopted in which the magnitude of the load increment is adjusted depending on the convergence rate in previous step: a maximum allowable iteration $i_{\max}$ is chosen for a single load step. For the n^{th} load step, if convergence does not occur after up to $i_{\max}$ iterations, the load factor $\lambda^{(n)}$ is reduced and incremental load is recalculated. On the other hand, if for the n^{th} load step, convergence occurs after j iterations where $j \leq i_{\max}$, the load factor is increased for computations of the next load step.

3-5 Boundary value problems

First, the CRFE solution is compared with the analytical solution for a cantilever beam under a bending moment along its free edge, as shown in Figure 3.5. Young's modulus and Poisson ratio of the beam are selected arbitrary here as 10 MPa and 0.2, respectively. It is seen that CRFE solution is in excellent agreement with the analytical solution obtained by Reissner's theory described in previous chapter. Figure 3.6 shows the deformed shapes of a cantilever thin shell under several magnitudes of bending moment along the free edge of the shell. Note that the displacements are normalized with respect to the length of the shell.

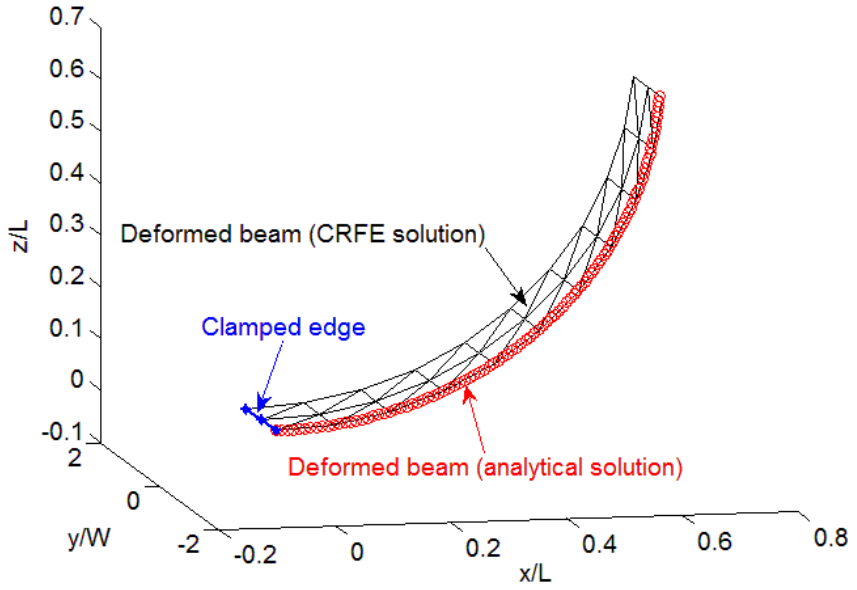

Figure 3.5. Comparison of predicted deformed configuration of the beam by CRFE method with Reissner's theory approach

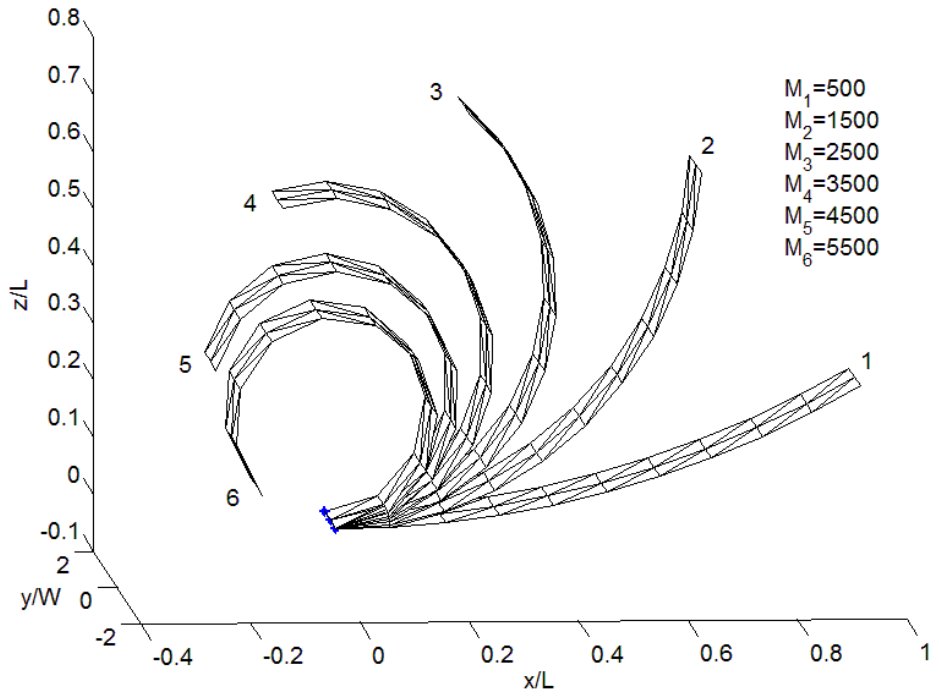

Figure 3.6. Deformed configuration of the beam subjected to a bending moment in N.m along its free edge

Table 3.1. Properties of the components of the smart shell

Piezoelectric patch	Supporting shell
$d_{13} = d_{23} = 0.18$ nm/V, $d_{63} = 0$, $\beta_{13} = 0.8$ f(m/V)^2 $E_p = 63$ GPa $v_p = 0.28$ $t_p = 0.5$ mm	$E_{pl} = 2$ GPa $v_{pl} = 0.1$ $t_{pl} = 5$ mm

In the following boundary value problems, several reconfigurations are simulated. The material properties are listed in Table 3.1. Convergence study is preformed to evaluate the size of elements needed for discretizing the domain for obtaining accurate results. Figure 3.7 shows the configuration of a shell with one pair of patches stimulated by electric field with magnitude of 1.3 MV/m when a nonlinear behavior is considered for the piezoelectric material in terms of electric field or 9.2 MV/m when a linear electro-mechanical behavior is considered. The domain is discretized with 600 elements. The effect of number of elements on the maximum displacement of the shell at its free edge is shown in Figure 3.8. As seen, there is a little change in the result by changing the number of elements from 200 to 600 with average number of iterations equals 3 during load steps. Therefore the results with 400 elements can be considered reasonably accurate although smaller element size leads to more accurate deflected configuration of the shell especially when quality of deflection is concerned. Moreover, in Figures 3.9 variations of translational and rotational displacements versus number of iterations until convergence are shown at two stages of loading: 0.1MV/m and 1.2MV/m. It should be noted that the criterion of zero residual load (Eq. (3.79)) was also checked in addition to Eq. (3.78) criterion, but for the problems considered here there is almost no change in the responses (less than 0.0001%) when only displacement residual or displacement and force residuals are considered. The variation of residual force versus iteration number is shown in Figure 3.10.

$$\frac{\left\|\mathbf{F}_{\text{int}} - \mathbf{F}_{ext}\right\|}{\left\|\mathbf{F}_{ext}\right\|} \leq 0.01 \tag{3.79}$$

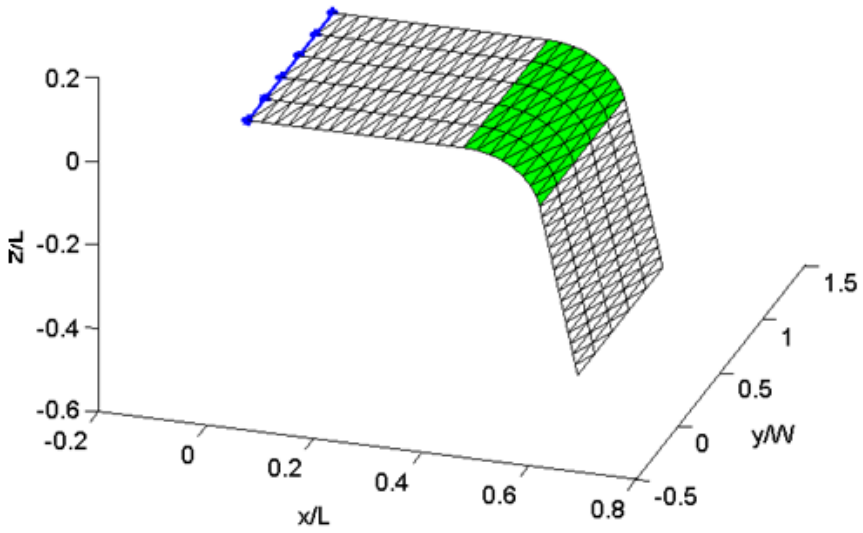

Figure 3.7. Configuration of the cantilever shell with one pair of active patches with 400 elements

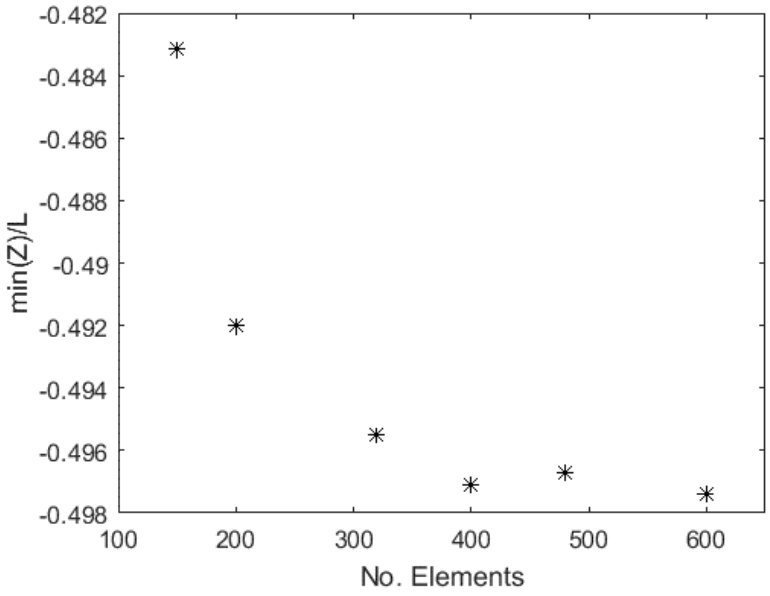

Figure 3.8. Convergence of the maximum displacement of the shell with one pair of patches

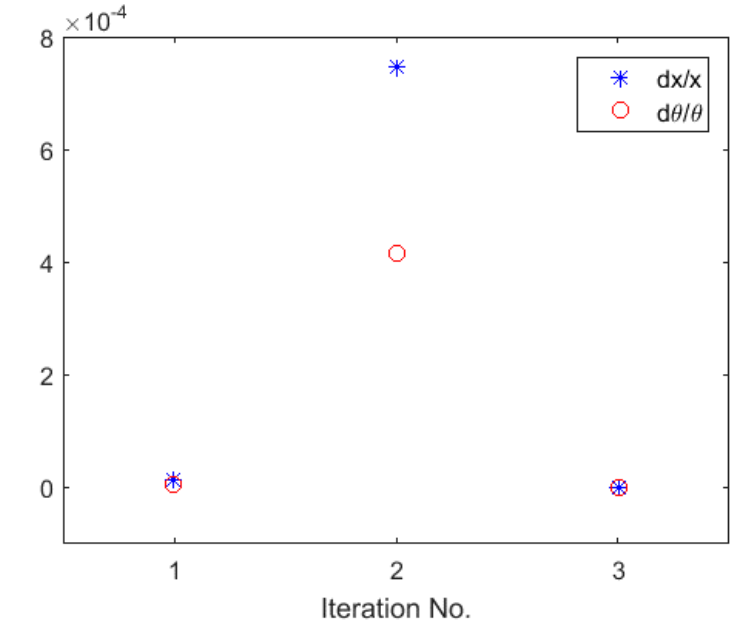

(a)

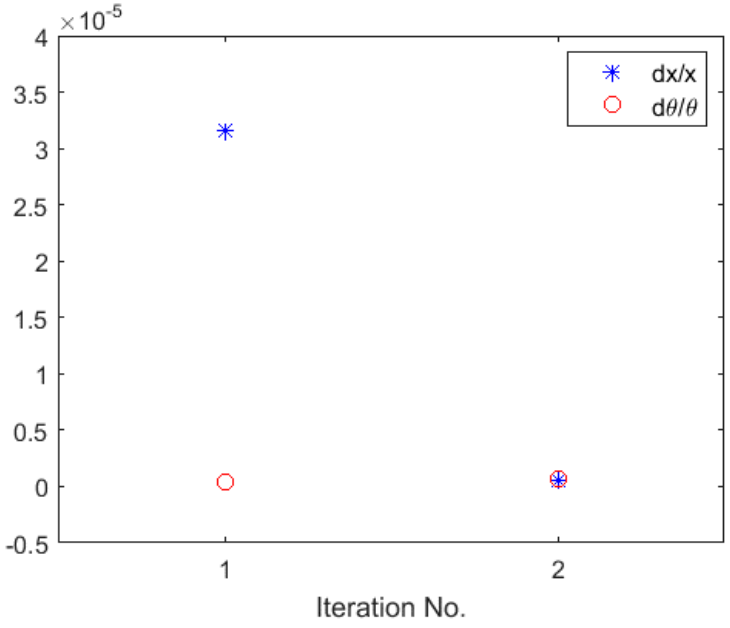

(b)

Figure 3.9. Translational and rotational displacement convergence criteria for the smart shell with one pair of patches at (a) 01 MV/m (b) 1.2 MV/m

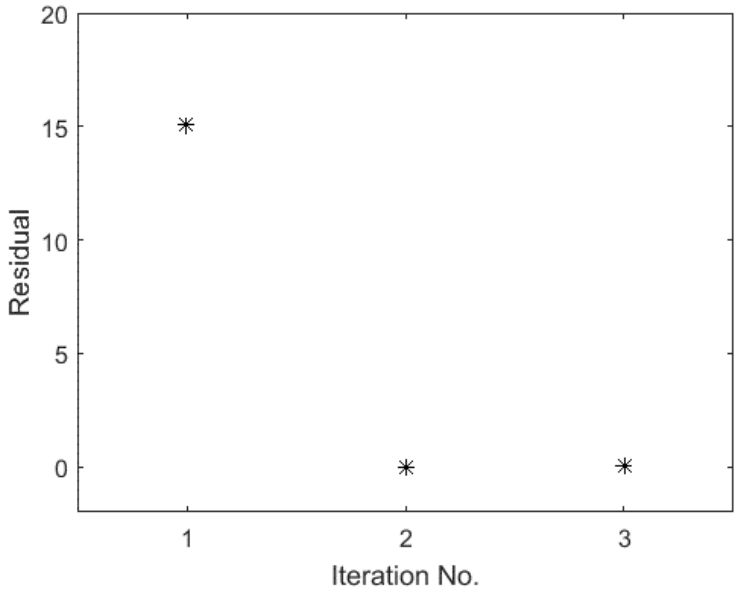

(a)

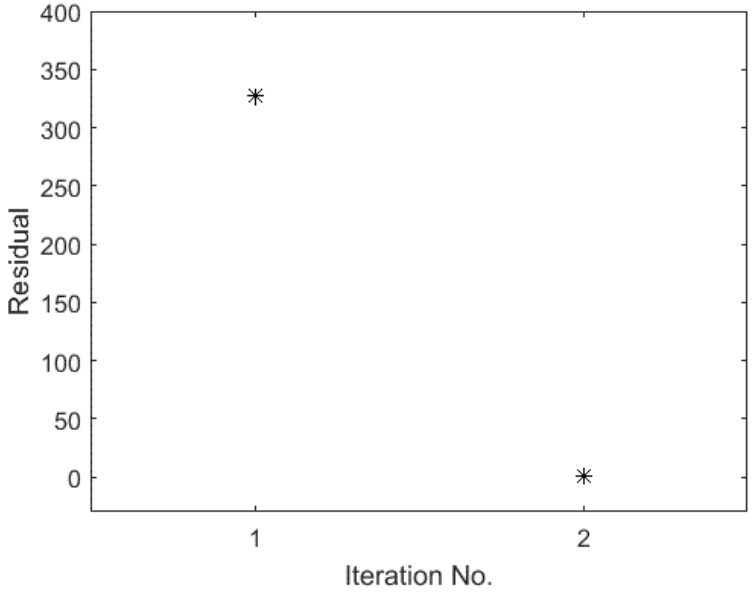

(b)

Figure 3.10. Convergence of the residual load of the shell with one pair of patches at (a) 0.1 MV/m and (b) 1.2 MV/m

Similar convergence analysis is presented for a smart shell with two pairs of patches shown in Figure 3.11. The direction of applied electric field to one pair is opposite of the other one which leads to opposite curvature direction on location of the shell covered by the patches.

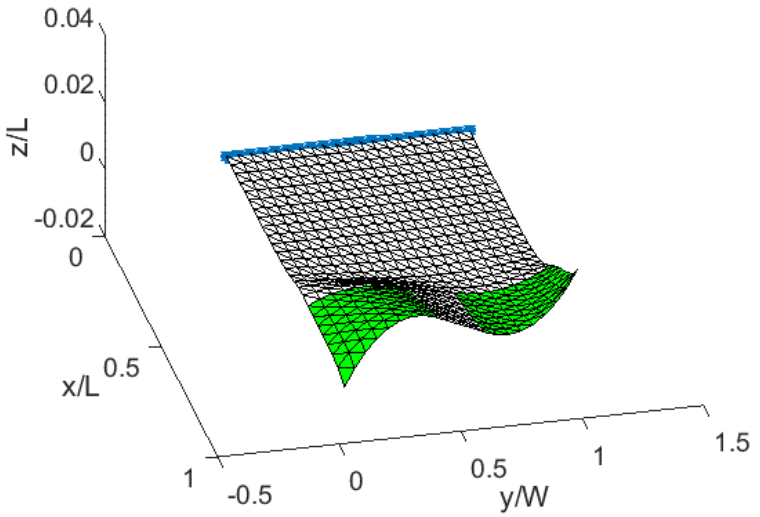

Figure 3.11. Configuration of the cantilever shell with two activated pairs of patches in opposite directions

Maximum tip displacement of the shell tip versus number of element used for discretization is shown in Figure 3.12 which implies that 600 elements give accurate results reasonably. Also, as in previous example, variation of convergence criteria versus iteration number at two load steps, 01 MV/m and 1.2 MV/m, are presented in figure 3.13 and 3.14.

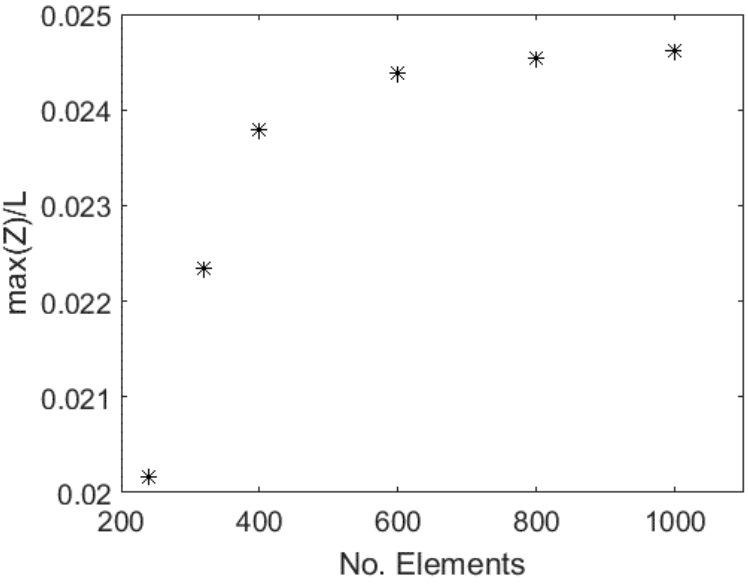

Figure 3.12. Convergence of the maximum displacement of the shell with one pair of patches

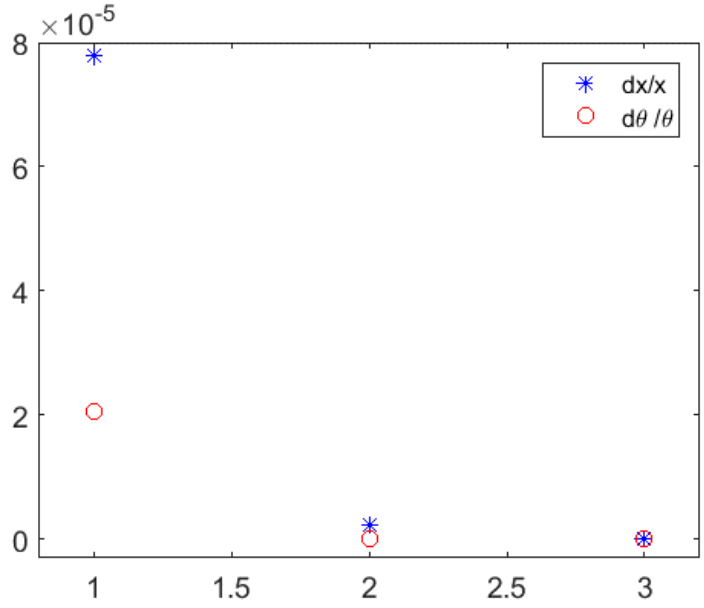

(a)

Figure 3.13. Translational and rotational displacement convergence criteria for the smart shell with two pairs of patches at (a) 01 MV/m (b) 1.2 MV/m

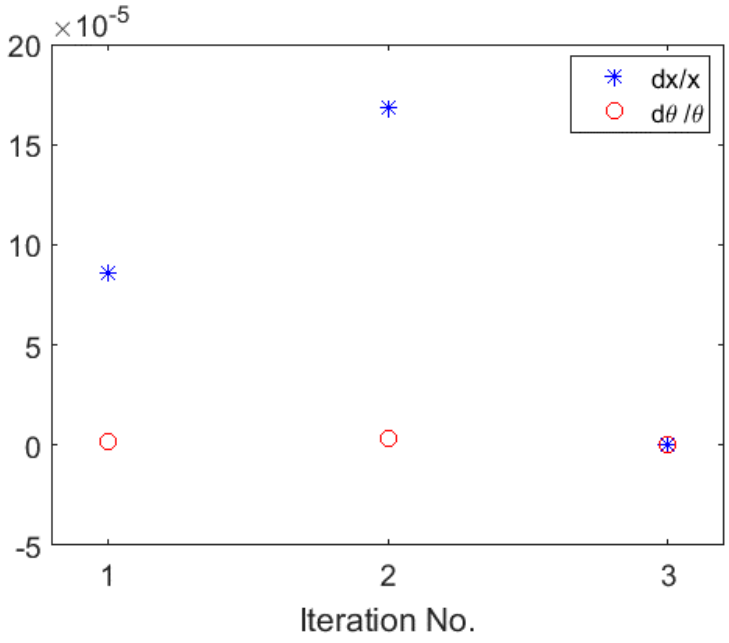

(b)

Figure 3.13. Continued

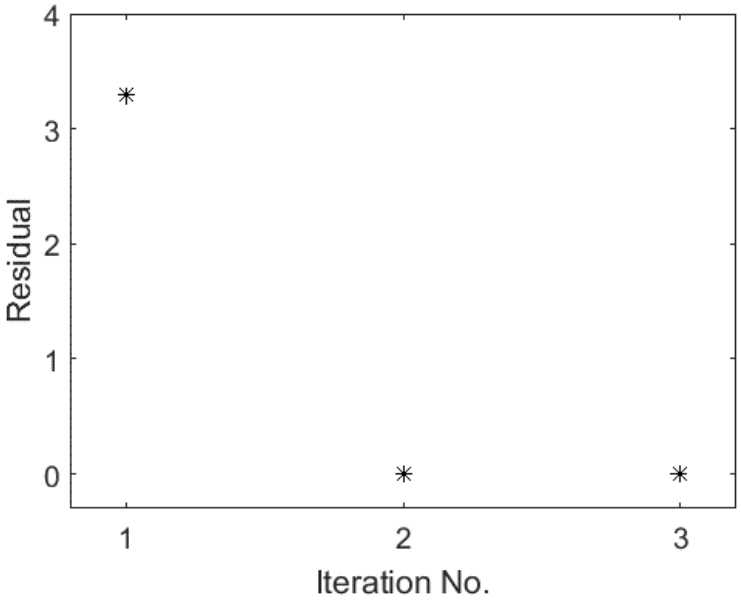

(a)

Figure 3.14. Convergence of the residual load of the shell with two pairs of patches at (a) 0.1 MV/m and (b) 1.2 MV/m

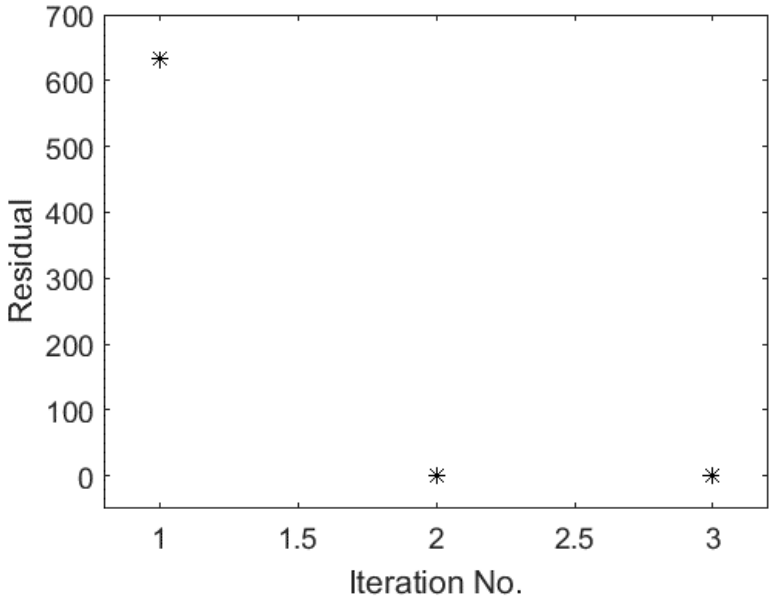

(b)

Figure 3.14. Continued

As seen in the two problems above, the load residual in each presented example decreases with increase of iteration number but no clear trend in variation of incremental displacements versus iteration number are observed.

The effect of magnitude of electric stimulus on deformation of the shell with one active pair of patches is shown in Figure 3.15a.This reconfiguration under different magnitudes of stimulus is to resemble morphing shape change of wing for a micro aircraft whose conceptual design is proposed by DARPA and NASA seen in Figure 3.15b.

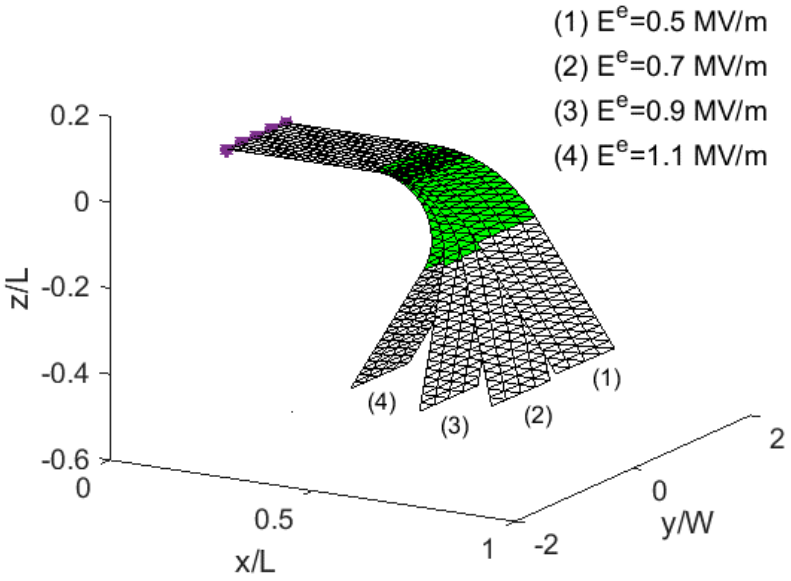

(a)

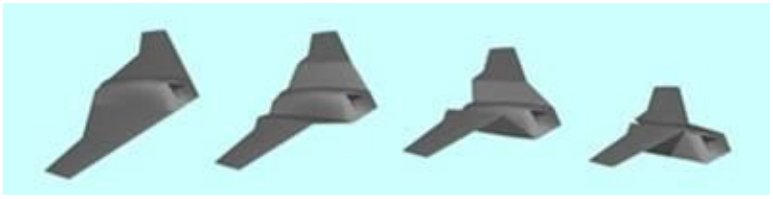

(b)

Figure 3.15. (a) Configuration of the cantilever shell under various magnitude of electric stimulus resembling (b) DARPA and NASA morphing wing concept

In Figures 3.16a-b respectively, linear and nonlinear electro-mechanical responses of piezoelectric material as actuators are compared. Again, nonlinear piezoelectric coefficient is considered as $\beta_{13}=8\times10^{-7}$ n m^2/V^2 [45]. Under the same magnitude of electric field $E^e = 1.3\text{MV/m}$, as seen, there is significant effect on deformed configuration of the structure with such magnitude of the stimulus for the actuators. Figures 3.17a and b show the axial strain distributions along the longitudinal direction of the shells corresponding to shells in

Figures 3.16a and b, respectively. Such ring shape configuration shown in Figure 3.12b can be useful for deployable applications. Besides, the strain magnitude over the covered areas with patches is relatively small for the shell undergoing large deformations shown in Figure 3.16.

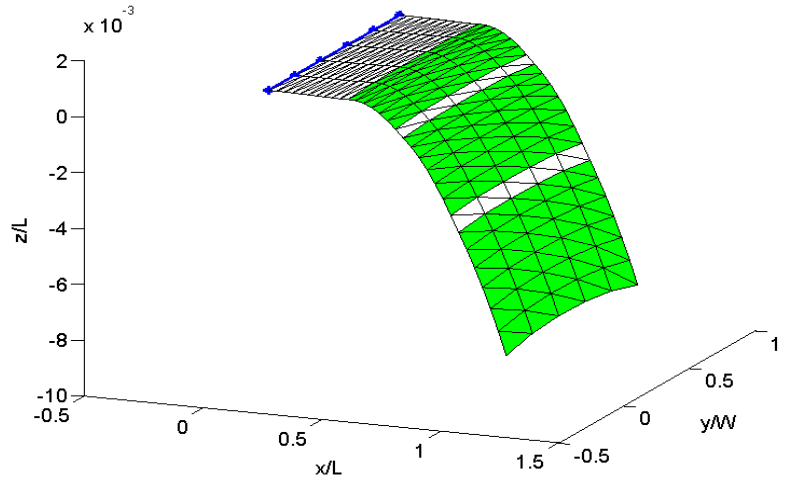

(a)

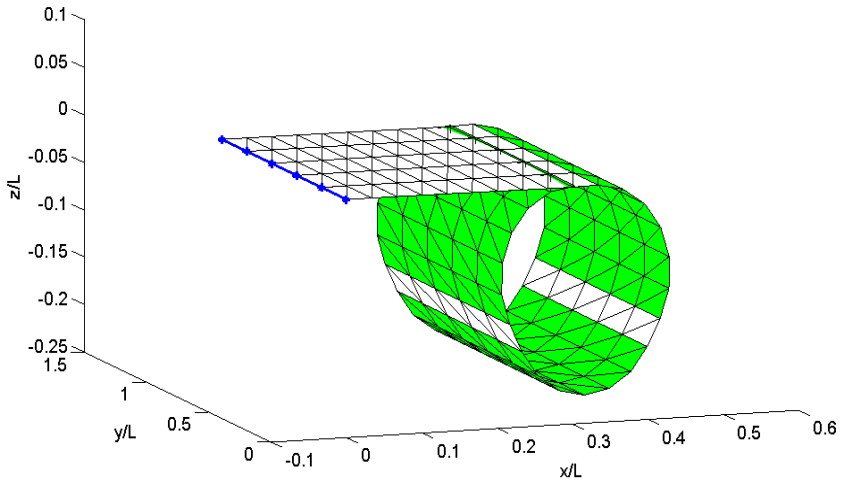

(b)

Figure 3.16. Configuration of the cantilever shell under actuation of three pairs of piezoelectric patches with (a) linear behavior (b) nonlinear behavior in terms of electric field

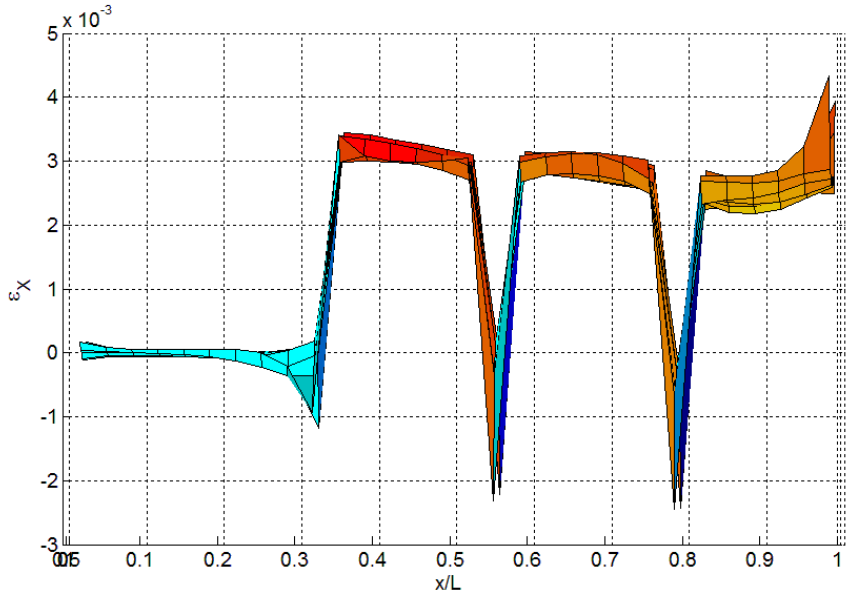

(a)

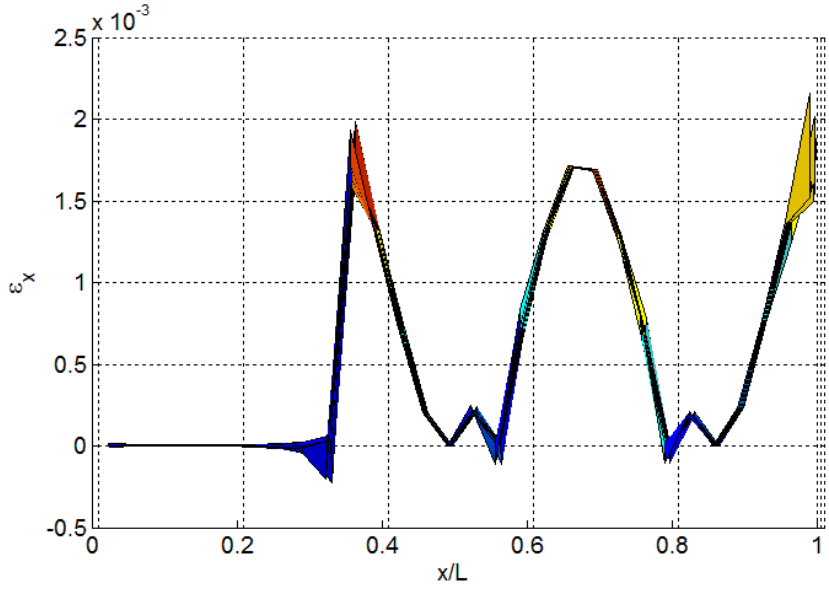

(b)

Figure 3.17. Axial strain distribution (ε_x) of the cantilever shell under actuation of three pairs of piezoelectric patches (a) with (a) linear behavior (b) nonlinear behavior in terms of electric field

Another example is shown in Figure 3.18, where configurations of a smart shell with two substrate stiffness, 2 GPa and 0.01 GPa and two pairs of active patches is shown is activated by an electric field E^e=0.9 MV/m. Nonlinear electro-mechanical responses is considered. As seen, the stiffness of the substrate does not affect amount of deflection significantly. It means that effect of the stiffness of the substrate on the magnitude of induced load is the same as on the magnitude of the bending rigidity of the structure; it is consistent with the results obtained in chapter 2 where change of relaxation function does not affect much configuration of actuate viscoelastic beam (see Figure 2.13 and 2.15). Such configuration can resemble deformed shape of flapping side wings or a tail wing of micro-aerial vehicle.

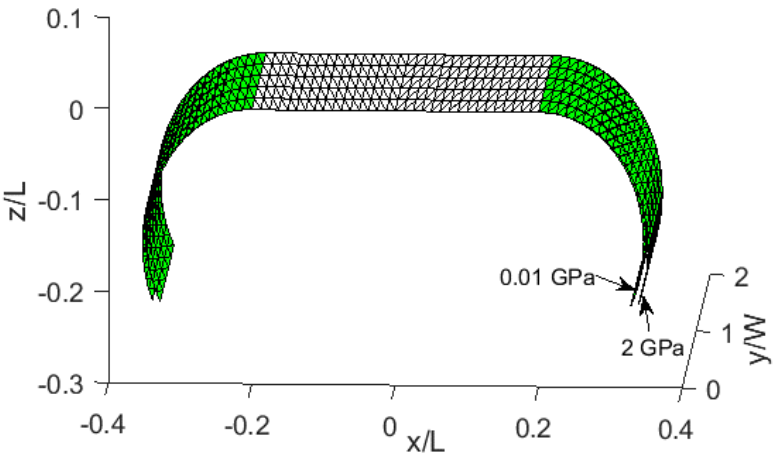

Figure 3.18. Configuration of the shell with two pairs of piezoelectric patches with two substrate stiffness

Figure 3.19 shows configuration of the actuated smart shells with one pair of actuated piezoelectric patches. The shell is clamped along its two opposite edges as highlighted in the figure and actuated with electric field in magnitude of 1.3 MV/m. Distribution of axial strains in direction of length and width of the plate, ε_x, ε_y are shown in Figure 3.20a and b, respectively. Again this confirms that the plate is undergoing small strain and the deformation in this configuration is dominated by rotation. Other configuration of a smart

shell with four pairs of patches constrained only in its middle subjected to 0.9 MV/m electric field is shown in Figure 3.21. Finally, Figure 3.22 shows a shell with four pairs of patches where in contrast to previous cases, the direction of applied electric fields, E^e= 0.9 MV/m are in opposite directions for the pairs.

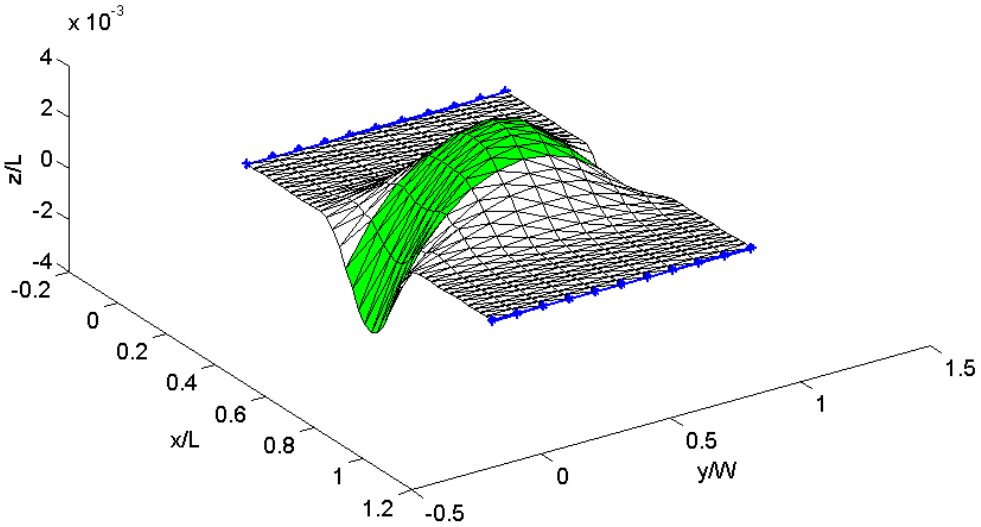

Figure 3.19. Configuration of the shell with two clamped edges under actuation of one pairs of piezoelectric patches

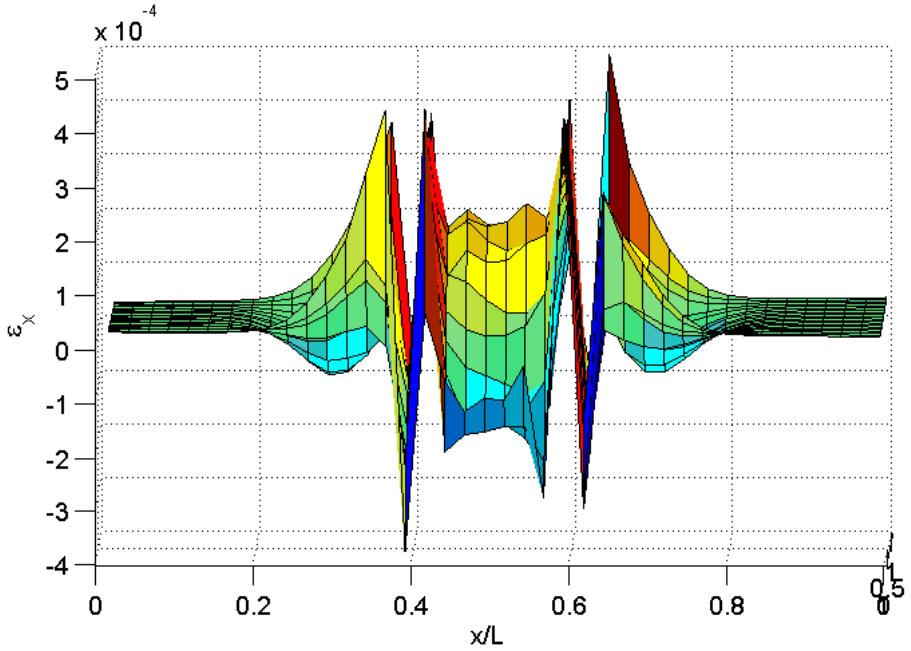

(a)

Figure 3.20. Axial strain distributions (a) ε_x and (b) ε_y over the shell with two opposite clamped edges

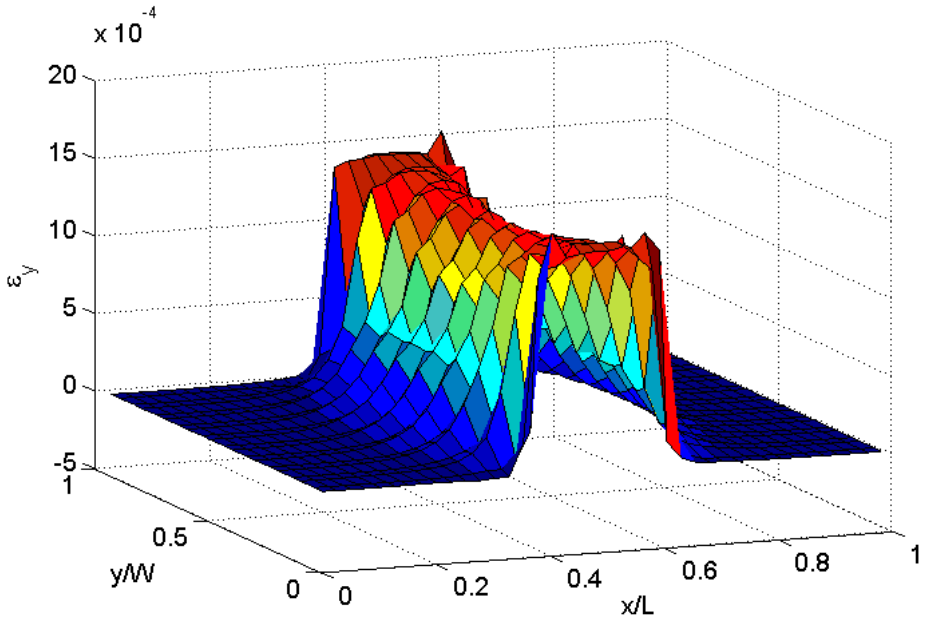

(b)

Figure 3.20. Continued

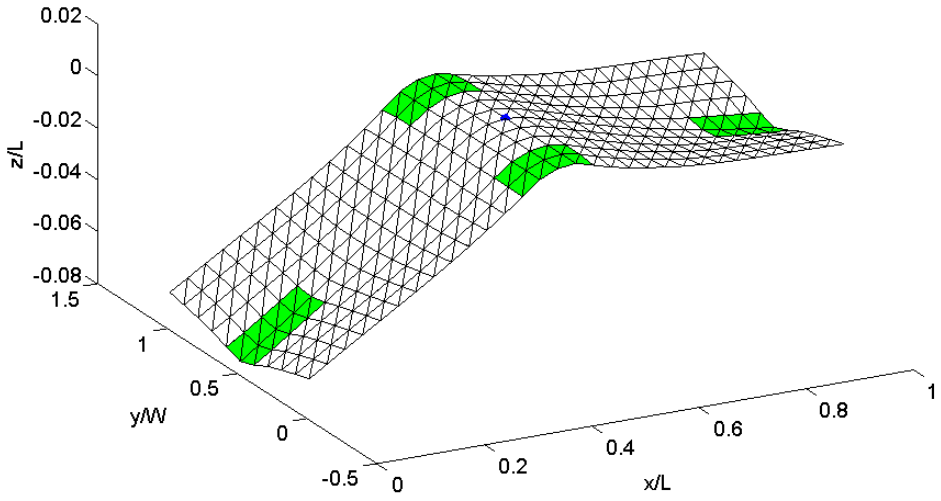

Figure 3.21. Configuration of the shell with free edges under actuation of four pairs of piezoelectric patches

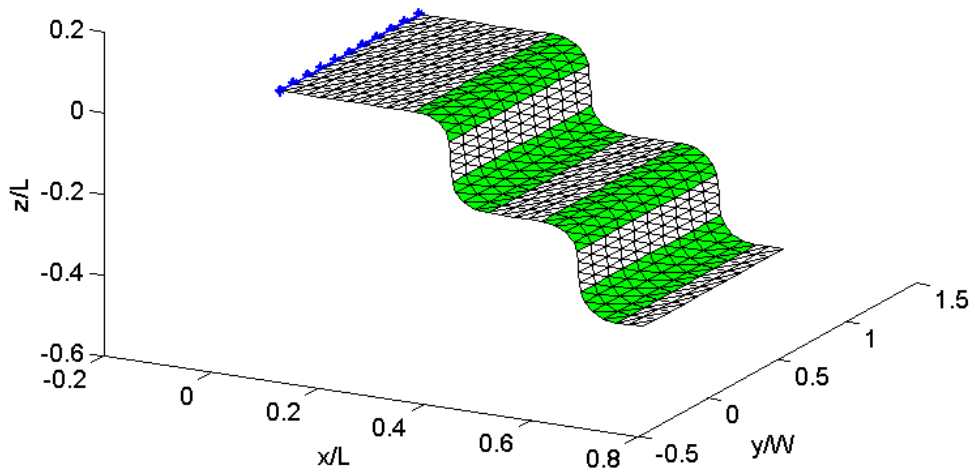

Figure 3.22. Configuration of the smart shell with four pairs of piezoelectric patches stimulated in opposite directions

4. ANALYSIS OF SMART SHELLS WITH GEOMETRIC NONLINEARITIES AND TIME-DEPENDENCE

4-1 Introduction

In this chapter, the study is extended to viscoelastic analysis so that it can contribute to wider range of applications where the structure is made of polymers and understand the impact of viscoelastic polymers have on the shape changes in active composites. Viscoelastic characteristics are considered for both components of the smart shell including the electro-active patch and substrates. AFC, which shows viscoelastic effect, is considered for the electro-active patches. Material characterizations of AFC are also discussed in this chapter. The general higher order electro-active model can also be used for other electro-active materials, such as piezoelectric polymers and electrostrictive materials.

4-2 Effect of distributed piezoelectric actuators on the supporting viscoelastic shell

Similar to the elastic substrate case, the shell is assumed to be originally straight and one or multiple pairs of piezoelectric patches are bonded perfectly to the top and bottom of the substrate symmetrically with respect to the middle axis or plane of the shell. Patches may show either elastic or viscoelastic response.

4-2-1 Elastic piezoelectric patch

In Chapter 3, for a completely elastic smart structure in chapter 3 the Eqs. (3.9) and (3.11) in terms of strains are written as follows

$$\begin{aligned} A\left(\varepsilon_{xi}+\nu_s\varepsilon_{yi}\right) &= B\left(E_p\varepsilon_{xi}+\nu_p E_p\varepsilon_{yi}-E_p(1+\nu_p)\varepsilon_p\right) \\ A\left(\varepsilon_{yi}+\nu_s\varepsilon_{xi}\right) &= B\left(E_p\varepsilon_{yi}+\nu_p E_p\varepsilon_{xi}-E_p(1+\nu_p)\varepsilon_p\right) \end{aligned} \tag{4.1}$$

where

$$A=\frac{E_s}{1-\nu_s{}^2}\ ;\ B=\frac{-3ht\left(2h+t\right)}{\left(2h^3+3ht^2+2t^3\right)\left(1-\nu_s{}^2\right)} \tag{4.2}$$

where the parameters are the same as the one defined in Chapter 3 and shown in Figure 3.1.

Now, by considering the time-independent response for the piezoelectric patches and linear viscoelastic constitutive relations for the substrate subjected to small strains under electric field stimulus, the viscoelastic version of Eq. (4.1) is rewritten as

$$\begin{aligned}\int_0^t A(t-\tau)\frac{d\varepsilon_{xi}}{d\tau}d\tau+\nu_{pl}\int_0^t A(t-\tau)\frac{d\varepsilon_{yi}}{d\tau}d\tau&=B\left(E_p\varepsilon_{xi}(t)+\nu_pE_p\varepsilon_{yi}(t)-E_p(1+\nu_p)\varepsilon_p(t)\right)\\ \int_0^t A(t-\tau)\frac{d\varepsilon_{yi}}{d\tau}d\tau+\nu_{pl}\int_0^t A(t-\tau)\frac{d\varepsilon_{xi}}{d\tau}d\tau&=B\left(E_p\varepsilon_{yi}(t)+\nu_pE_p\varepsilon_{xi}(t)-E_p(1+\nu_p)\varepsilon_p(t)\right)\end{aligned} \tag{4.3}$$

where $A(t)=E_s(t)/\ (1-\nu_s^2)$, $E_s(t)$ is the relaxation function of the substrate; the Poisson's ratio of the shell ν_s is assumed to be constant in terms of time. Again, E_p and ν_p are the elastic modulus and Poisson's ratio of the piezoelectric patches respectively. The free strain of the elastic piezoelectric material ε_p is defined as before but here is a function of time if the electric stimulus changes over time.

In more concise form, the Eq. (4.3) is written as

$$\begin{aligned}A(t)*\mathrm{D}\varepsilon_{xi}(t)+\nu_sA(t)*\mathrm{D}\varepsilon_{yi}(t)&=B\left(E_p\varepsilon_{xi}(t)+\nu_pE_p\varepsilon_{yi}(t)-E_p(1+\nu_p)\varepsilon_p(t)\right)\\ A(t)*\mathrm{D}\varepsilon_{yi}(t)+\nu_sA(t)*\mathrm{D}\varepsilon_{xi}(t)&=B\left(E_p\varepsilon_{yi}(t)+\nu_pE_p\varepsilon_{xi}(t)-E_p(1+\nu_p)\varepsilon_p(t)\right)\end{aligned} \tag{4.4}$$

where D denotes time derivative operator and '$*$' stands for convolution integral over [0, t].

To solve the above set of integral equations, Laplace transformation is used to transfer the system of integral equations (4.3) to Laplace space and obtain the following set of linear equations,

$$\begin{aligned}\tilde{A}\tilde{\mathrm{D}}\varepsilon_{xi}+\nu_s\tilde{A}\tilde{\mathrm{D}}\varepsilon_{yi}&=B\left(E_p\tilde{\mathrm{D}}\varepsilon_{xi}+\nu_pE_p\tilde{\mathrm{D}}\varepsilon_{yi}-E_p(1+\nu_p)\tilde{\mathrm{D}}\varepsilon_p\right)/s\\ \tilde{A}\tilde{\mathrm{D}}\varepsilon_{yi}+\nu_s\tilde{A}\tilde{\mathrm{D}}\varepsilon_{xi}&=B\left(E_p\tilde{\mathrm{D}}\varepsilon_{xi}+\nu_pE_p\tilde{\mathrm{D}}\varepsilon_{yi}-E_p(1+\nu_p)\tilde{\mathrm{D}}\varepsilon_p\right)/s\end{aligned} \tag{4.5}$$

where superscript '~' again indicates transformed function in Laplace space. By solving the above system and then inverse Laplace transformation, the time-dependent interface strains are obtained and then in similar way to the elastic case, the time-dependent induced unit moments to the substrate are obtained as:

$$\begin{aligned}m_x(t)&=\frac{2h^2}{3\left(1-\nu_{pl}^2\right)}\left(E_{pl}*\mathrm{D}\varepsilon_{xi}+\nu_{pl}E_{pl}*\mathrm{D}\varepsilon_{yi}\right)\\ m_y(t)&=\frac{2h^2}{3\left(1-\nu_{pl}^2\right)}\left(E_{pl}*\mathrm{D}\varepsilon_{yi}+\nu_{pl}E_{pl}*\mathrm{D}\varepsilon_{xi}\right)\end{aligned} \tag{4.6}$$

4-2-2 Viscoelastic active fiber composites (AFCs)

This section presents responses of AFCs manufactured from Advanced Cerametrics Inc. Mechanical tests were conducted on AFC at Pennsylvania State University, which show significant viscoelastic response of AFC. Electro-mechanical tests were also done that indicate time-dependent behaviors of the coupling properties. Time-dependent constitutive models are formulated for the mechanical and electro-mechanical coupling responses for AFC. Experimental data are used for material characterization and model verification. Finally, the time-dependent constitutive models for the AFCs are incorporated to the smart flexible shells.

4-2-2-1 Electromechanical properties of the AFC

The time-dependent relaxation function of the AFC is calibrated from experimental data obtained by Dr. Ounaies and her students at Pennsylvania State University reported in [56]. The time-dependent relaxation function of the AFC in fiber direction, 1, is assumed to have the following form:

$$E_{p,11}(t) = E_{p,11}^{el}\left(\Upsilon_\infty + \sum_{n=1}^{N} \Upsilon_n e^{-t/\tau_n}\right) \tag{4.7}$$

where $\Upsilon_\infty + \sum_{n=1}^{N} \Upsilon_n = 1$ and $\Upsilon_\infty + \sum_{n=1}^{N} \Upsilon_n e^{-t/\tau_n}$ is called the normalized relaxation function. Υ_∞ is the time-dependent function at relaxed (equilibrium) condition and τ_n, n =1,…,N, are series of relaxation times which indicate the speed of relaxation. Low values of τ_n show fast relaxation processes, while large values of τ_n indicate slow relaxation processes. Although the rate of relaxation process may change at different strain levels or temperatures, here we assume that temperature is kept constant (25^{o}C) under applied electric field and also because of small strain case, the relaxation function is considered only time-dependent.

Under a uniaxial tensile test in the fiber direction, the tensile elastic modulus of the AFC in the fiber direction E_{p11}^{el} is measured as 9.76 GPa, from the elastic (instantaneous) response. Figure 4.1 shows the relaxation data from experiment and the fitted curve based on the Prony series of Eq. (4.7). Since $E_{p11}(t)$ is in the form of Prony series, for optimized data fitting, a nonlinear least square algorithm named Trust region reflective algorithm, was utilized in MATLAB (Mathworks, Inc.). The obtained parameters $\Upsilon_\infty, \Upsilon_1, ..., \Upsilon_N$ are presented in Table 4.1.

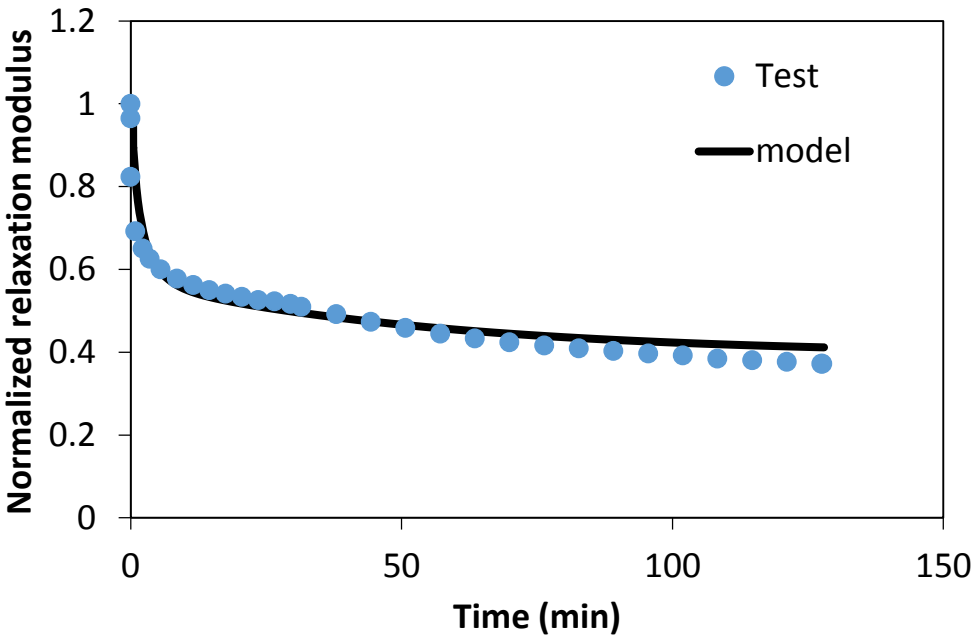

Figure 4.1. Time dependent relaxation function at room temperature

Table 4.1. Normalized parameters of the relaxation function

n	Υ_n	τ_n (min)
∞	0.3934	-
1	0.1449	1.04976
2	0.00277	0.00923
3	0.00069	49.75124
4	0.1771	3.32799
5	0.1078	0.01006
6	0.1759	56.17978

For the piezoelectric coefficients of the AFC, the values reported by Khan et al. [80] are used. The linear piezoelectric coefficient in the fiber direction (d_{11}) of the AFC is expressed as a time-dependent kernel function as follows

$$d_{p11}(t)=d_{p11,0}+\sum_{n=1}^{N} d_{p11,n}\left[1-e^{-t/\lambda_n}\right] \tag{4.8}$$

Table 4.2. Parameters of the Prony series for piezoelectric coefficient

n	$d_{p11,n}$ (pm/V)	λ_n (min)
0	110	-
1	10	0.2
2	120	1
3	10	10
4	140	60

Based on the available experimental data, the nonlinear piezoelectric coefficient (β_{p11}) is assumed to have similar time-dependent function and differs from the linear coefficient by a constant, which is calibrated from instantaneous response of the piezoelectric material. This approach is similar to the quasi-linear viscoelastic model, originally proposed by Fung [81]. Figure 4.2 shows the experimental data and estimated data from least square algorithm. The calibrated properties are $\varepsilon = d_{p11,0}(E^e + 2.32\times10^{-5}E^{e2})$ and therefore, $\beta_{p11} = 2.32\times10^{-5}(m/V)\times d_{p11}$. The R-squared equals 99.1% which verifies the high accuracy of the modeled data.

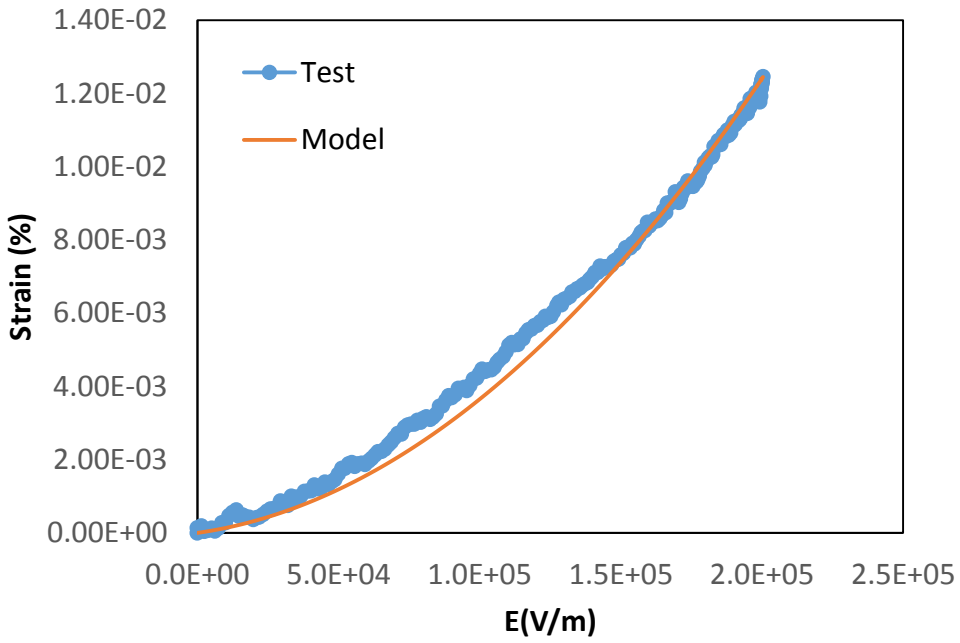

Figure 4.2. Strain response of AFC in fiber direction

The AFC is considered orthotropic with fibers in direction 1; due to lack of experimental data, the properties in directions perpendicular to the fibers are approximated as $E_{p22}(t) \approx (15/19)E_{p11}(t)$ [80] and $d_{21}(t) \approx -0.5d_{11}(t)$ [82]. The corresponding Poisson's coefficients (ν_{12} =0.28 and ν_{21}= (15/19) ν_{12} [80] of the material are assumed time-independent.

4-2-2-2 Time-dependent interaction of the AFCs and the substrate

The constitutive stress-strain for the AFC are written as:

$$\begin{aligned}\left(\sigma_{xi}\right)_p &= \frac{1}{1-\nu_{12}\nu_{21}}\left(E_{px} * \mathrm{D}\varepsilon_{xi} + \nu_{12}E_{py} * \mathrm{D}\varepsilon_{yi} - E_{px} * \mathrm{D}\varepsilon_{px} - \nu_{12}E_{py} * \mathrm{D}\varepsilon_{py}\right), \\ \left(\sigma_{yi}\right)_p &= \frac{1}{1-\nu_{12}\nu_{21}}\left(E_{py} * \mathrm{D}\varepsilon_{yi} + \nu_{12}E_{py} * \mathrm{D}\varepsilon_{xi} - E_{px} * \mathrm{D}\varepsilon_{py} - \nu_{12}E_{py} * \mathrm{D}\varepsilon_{px}\right)\end{aligned} \quad (4.9)$$

Fibers of the AFC are assumed in *x*-direction. From the equilibrium conditions and considering continuity condition at interface strains, the following sets of equations in terms of unknowns ε_{yi} and ε_{xi} are:

$$\left(\frac{E_s(t)}{1-\nu_{pl}{}^2}-\frac{\kappa_g E_{px}(t)}{1-\nu_{12}\nu_{21}}\right)*\mathrm{D}\varepsilon_{xi}(t)+\left(\frac{\nu_s E_s(t)}{1-\nu_s{}^2}-\frac{\kappa_g \nu_{12} E_{py}(t)}{1-\nu_{12}\nu_{21}}\right)*\mathrm{D}\varepsilon_{yi}(t)=$$
$$\frac{\kappa_g}{1-\nu_{12}\nu_{21}}\left(-E_{px}(t)*\mathrm{D}\varepsilon_{px}(t)-\nu_{12}E_{py}(t)*\mathrm{D}\varepsilon_{py}(t)\right),$$
$$\left(\frac{E_s(t)}{1-\nu_{pl}{}^2}-\frac{\kappa_g E_{py}(t)}{1-\nu_{12}\nu_{21}}\right)*\mathrm{D}\varepsilon_{yi}(t)+\left(\frac{\nu_s E_s(t)}{1-\nu_s{}^2}-\frac{\kappa_g \nu_{12} E_{py}(t)}{1-\nu_{12}\nu_{21}}\right)*\mathrm{D}\varepsilon_{xi}(t)=$$
$$\frac{\kappa_g}{1-\nu_{12}\nu_{21}}\left(-E_{py}(t)*\mathrm{D}\varepsilon_{py}(t)-\nu_{12}E_{py}(t)*\mathrm{D}\varepsilon_{px}(t)\right) \qquad (4.10)$$

where

$$\varepsilon_{px}\equiv\varepsilon_{p1}=\int_0^t d_{11}(t-\tau)\frac{\partial F^{\varepsilon}}{\partial E_1^e}\frac{\partial E_1^e(\tau)}{\partial\tau}d\tau$$
$$\varepsilon_{py}\equiv\varepsilon_{p2}=\int_0^t d_{21}(t-\tau)\frac{\partial F^{\varepsilon}}{\partial E_1^e}\frac{\partial E_1^e(\tau)}{\partial\tau}d\tau \qquad \text{(1 is in fiber direction)} \qquad (4.11\text{-a})$$

and

$$F^{\varepsilon}=E_1^e+2.32\times10^{-5}(m/V)\,E_1^{e\,2} \qquad (4.11\text{-b})$$

By solving Eq. (4.10) in Laplace space, the induced time-dependent moments to the substrate can be derived as before.

4-3 Structural analysis of the viscoelastic substrate

After computing the induced load from the elastic or viscoelastic actuators, the deformation analysis of viscoelastic thin substrate is performed using CRFE approach. The general stress-strain constitutive relation for the viscoelastic substrate in tensorial form is written as

$$\boldsymbol{\sigma}_{pl}(\mathbf{x},t)=\int_0^t \mathbf{E}_{pl}(t-\tau)\frac{\partial \boldsymbol{\varepsilon}_{pl}(\mathbf{x},t)}{\partial \tau}d\tau \tag{4.12}$$

or in matrix components form as follows

$$\sigma_{ij,\,pl}(\mathbf{x},t)=\int_0^t E_{ijkl,\,pl}(t-\tau)\frac{\partial \varepsilon_{kl,\,pl}(\mathbf{x},t)}{\partial \tau}d\tau \tag{4.13}$$

As the following equations are related to the substrate the subscript '*pl*' of the quantities is omitted for simplicity. We deal with the plane stress situation, $i, j, k, l = 1, 2$. In the FE formulation and incremental iterative process, the incremental quantities are expressed in discrete intervals of time. In order to determine small deformation displacements of an element, the incremental form of the viscoelastic constitutive equation is done in a similar procedure performed by Zocher et al [83] and presented here briefly. The incremental stress during the time increment *dt* from t_n to t_{n+1} on interval $[t_n, t_{n+1}]$ is written as

$$\Delta\boldsymbol{\sigma}=\int_0^{t_{n+1}} \mathbf{E}(t_{n+1}-\tau)\frac{\partial \boldsymbol{\varepsilon}(\mathbf{x},t)}{\partial \tau}d\tau-\int_0^{t_n} \mathbf{E}(t_n-\tau)\frac{\partial \boldsymbol{\varepsilon}(\mathbf{x},t)}{\partial \tau}d\tau \tag{4.14}$$

or

$$\Delta\sigma_{ij} = \int_{t_n}^{t_{n+1}} E_{ijkl}(t_{n+1}-\tau)\frac{\partial\varepsilon_{kl}(\mathbf{x},\tau)}{\partial\tau}d\tau + \int_{0}^{t_n}\Delta E_{ijkl}\frac{\partial\varepsilon_{kl}(\mathbf{x},\tau)}{\partial\tau}d\tau \tag{4.15}$$

The Wiechert model is chosen for describing components of the material relaxation tensor:

$$E_{ijkl}(t) = E_{ijkl_\infty} + \sum_{m=1}^{N_{ijkl}} E_{ijkl_m} e^{-\frac{t}{\rho_{ijkl_m}}} \tag{4.16}$$

In calculating the integrals in Eq. (4.14), $\partial\boldsymbol{\varepsilon}/\partial\tau$ is approximated as a constant matrix, the strain rate $\boldsymbol{\varepsilon}^{\bullet}$, and $\Delta\boldsymbol{\varepsilon} = \boldsymbol{\varepsilon}^{\bullet}\Delta t$ over the interval [t_n, t_{n+1}]. Thus, the incremental form of the constitutive Eq. (4.14) is written as

$$\Delta\boldsymbol{\sigma} = \mathbf{E}'\boldsymbol{\varepsilon}^{\bullet} + \Delta\boldsymbol{\sigma}^{R} \tag{4.17}$$

where

$$\begin{aligned}
&\mathbf{E}' = \int_{t_n}^{t_{n+1}} \mathbf{E}(t_{n+1}-\tau)d\tau\ , \\
&\Delta\boldsymbol{\sigma}^{R} = \int_{0}^{t_n}\left[\mathbf{E}(t_{n+1}-\tau) - \mathbf{E}(t_n-\tau)\right]\frac{\partial\boldsymbol{\varepsilon}(\mathbf{x},t)}{\partial\tau}d\tau
\end{aligned} \tag{4.18}$$

For the FE implementation, the principle virtual work similar to the elastic problem but by considering time dependency can be written at t+Δt as

$$\int_{\Omega^e}\left(\boldsymbol{\sigma}^{t}+\Delta\boldsymbol{\sigma}\right)\left(\hat{\boldsymbol{\varepsilon}}^{t}+\Delta\hat{\boldsymbol{\varepsilon}}\right)dV = \int_{\partial\Omega^e}\mathbf{t}^{t+\Delta t}\boldsymbol{\psi}^{t+\Delta t}dS + \int_{\Omega^e}\rho\mathbf{q}^{t+\Delta t}\boldsymbol{\psi}^{t+\Delta t}dV \tag{4.19}$$

where **t** and **q** are surface traction and body force vectors respectively; ρ is density of the medium and $\boldsymbol{\psi}$ is a vector arbitrary admissible displacement functions and each component of $\hat{\boldsymbol{\varepsilon}}$ is defined in terms of components of $\boldsymbol{\psi}$ as $\hat{\varepsilon}_{ij} = 0.5(\psi_{i,j} + \psi_{j,i})$.

By considering the known equilibrium condition at *t* and substituting Eq. (4.17) into Eq. (4.19) gives

$$\int_{\Omega^e} \Delta\hat{\boldsymbol{\varepsilon}}\mathbf{E}'\Delta\boldsymbol{\varepsilon} dV = \int_{\partial\Omega^e} \mathbf{t}^{t+\Delta t}\Delta\boldsymbol{\psi}^{t+\Delta t} dS + \int_{\Omega^e} \rho\mathbf{q}^{t+\Delta t}\Delta\boldsymbol{\psi}^{t+\Delta t} dV - \int_{\Omega^e} \Delta\hat{\boldsymbol{\varepsilon}}\boldsymbol{\sigma}^t dV - \int_{\Omega^e} \Delta\hat{\boldsymbol{\varepsilon}}\Delta\boldsymbol{\sigma}^R dV \quad (4.20)$$

After some algebraic manipulations, the stiffness matrix, internal and external force vectors of the element can be derived as follows

$$\mathbf{f} = \int_{\Omega^e} \mathbf{B}^T\boldsymbol{\sigma}^t dV + \int_{\Omega^e} \mathbf{B}^T\Delta\boldsymbol{\sigma}^R dV; \quad \mathbf{K} = \int_{\Omega_e} \mathbf{B}^T\mathbf{E}'\mathbf{B}\, dV \quad (4.21)$$

By determining the stiffness and internal forces of an element of the substrate, the aforementioned CRFE formulations in the previous chapter are used in the same way as for the elastic case in Chapter 3 in order to derive the stiffness tensor and force vector for the entire domain. The solution procedure and the iterative algorithm used here are also the same as the one described in Chapter 3.

4-4 Boundary value problems

In this section, through some boundary value problems time-dependent deformations of smart shells subjected to electric stimuli are shown. The relaxation function of the isotropic substrate is expressed as

$$E_s(t) = 0.4 + 1.6e^{-t} \text{ GPa} \tag{4.22}$$

The Poisson's ratio of the viscoelastic substrate is assumed time-independent and the same as for elastic shell. The materials properties for the patches and thickness of the components are the same as before presented in Table 4.1. Again, nonlinear response of piezoelectric material in terms of electric field is taken into account.

The electric field stimulus is assume to be a time dependent function defined as follows, which has continuous time derivative during [0 t] so that Laplace transformation can be used easily for the convolution integrals.

$$E^e(t) = E_m^e(1 - e^{-t/t_r}) \tag{4.23}$$

A small viscoelastic shell with one pair of elastic piezoelectric patches is subjected to time-dependent electric field as described in Eq. (4.23) with $E_m^e = 1.1\text{MV/m}$ and $t_r = 0.02\text{sec}$ for total actuation time T. Thus, the load almost reaches to E_m^e and remains constant in less than 0.1 sec. The configuration of the shell for different times is shown in Figure 4.3. As seen, the curvature of the shell increases gradually at early time but it almost remain unchanged after T=0.5sec and so the configuration of the structure remains constant although the relaxation modulus of the viscoelastic shell decreases over time, Eq. (4.22).

The reason is similar the one described in Chapter 2 for smart beams; during stress relaxation within the substrate, interaction between the substrate and the patch also decreases under constant stimulus and because the induced moment from the activated patch also depends to the relaxation function thus, induced moment from the activated patch to the substrate decreases which makes up for rigidity reduction of the structure and so the shape remains constant. Figure 15 shows the induced moments to the substrate under the aforementioned electric stimulus, Eq. (56). When the electric stimulus increases from zero to nearly its maximum value, the induced moment increases at first and later it decreases with time because as the electric stimulus remains constant and the modulus decreases with time.

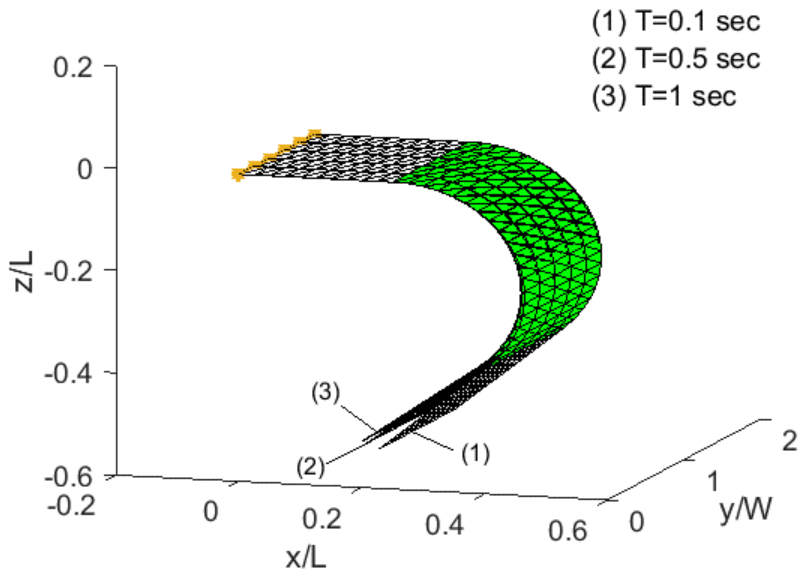

Figure 4.3. Configuration of the smart viscoelastic shell under actuation of one pair of elastic piezoelectric patches at different actuation time, *T*.

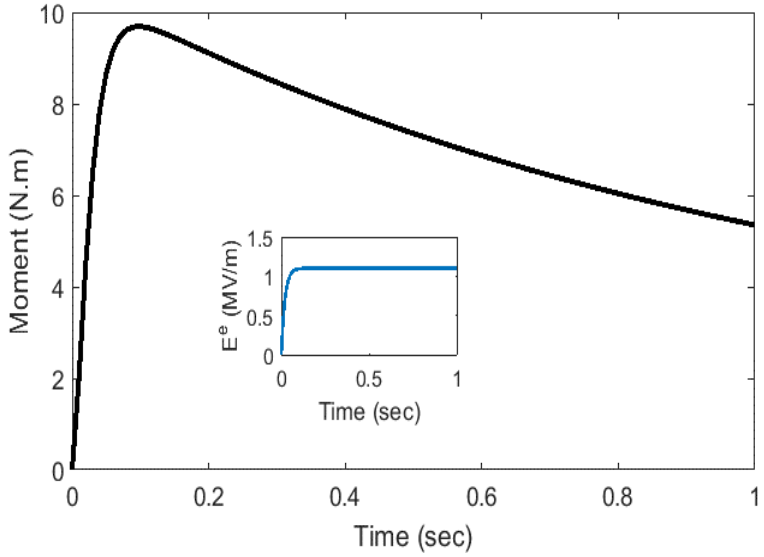

Figure 4.4. Induced moment by the elastic actuator to the viscoelastic substrate under shown electric stimulus E^e

Figure 4.5b shows numerical simulation of lateral deformation of another wing concept for mini UAVs (Figure 4.5a) by considering elastic piezoelectric actuators and

viscoelastic substrate. Similar to the previous case, it is seen deformation of the structure increase fast for $0<T<0.5$sec due to increase of applied electric field but then remains almost constant for $T>0.05$ sec.

(a)

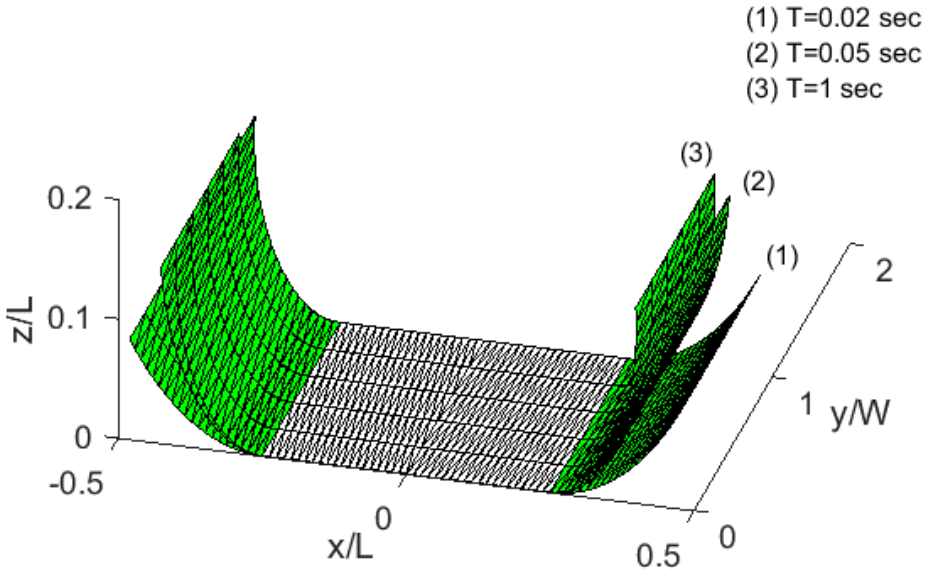

(b)

Figure 4.5. (a) A UAV concept and (b) configuration of the smart viscoelastic shell under actuation of two pairs of elastic piezoelectric patches at different actuation time, T.

The fact that under a constant electric stimulus to the elastic piezoelectric actuators, configuration of the viscoelastic structure is almost time-independent or stable over time is important in practice. Because it enables engineers to use polymers in designing for example lightweight structures with desired shape changes under certain stimulus magnitudes without being concerned about time effect on their configurations.

In the following examples, we consider the actuators made of AFCs with viscoelastic effects. The material properties of the AFCs are the ones presented in section (4-2-2-1). A slender viscoelastic shell with one pair of AFC patches is subjected to time-dependent electric field

as described in Eq. (4.23) with $E_m^e = 0.5\,\mathrm{MV/m}$ and $t_r = 0.02\,\mathrm{sec}$. The configurations of the shell for different times are shown in Figure 4.6. As seen, the curvature of the shell increases over time but its rate of increase reduced gradually. For large enough *T*, the configuration of the structure almost does not change, which is at the relaxed conditions for both the actuator and substrate. So here, unlike for the elastic patch, the viscoelastic effect on the deformation is observed. In this case the significant time-dependent effect is due to the piezoelectric coefficient of the AFC that change with time (Eq. (4.8)). The piezoelectric effect of the AFC leads to increase of the induced moment to the substrate over time. As time increases, reduction of the rate of the piezoelectric effect is seen until it becomes almost constant and thus, the deformation of the structure does not increase noticeably after some time.

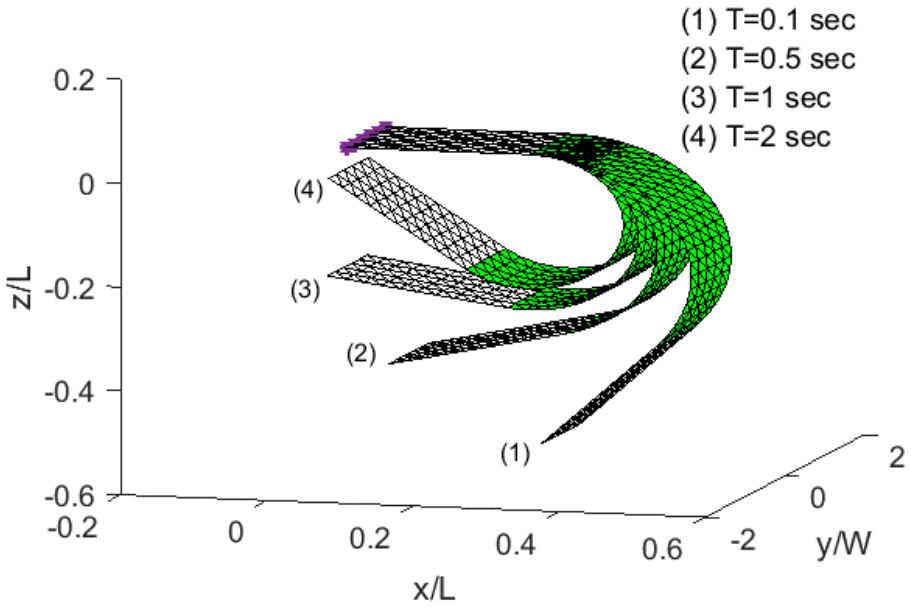

Figure 4.6. Configuration of the smart viscoelastic shell under actuation of one pair of AFC patches at different actuation time, *T*

In Figure 4.7a and b, a viscoelastic shell with non-uniform width actuated by four active pairs of AFC patches with $E_m^e = 0.5\,\mathrm{MV/m}$ for the time-dependent stimulus is shown. Over time the four arms along four edges of the square shape base fold gradually which can resemble a self-folding actuated box.

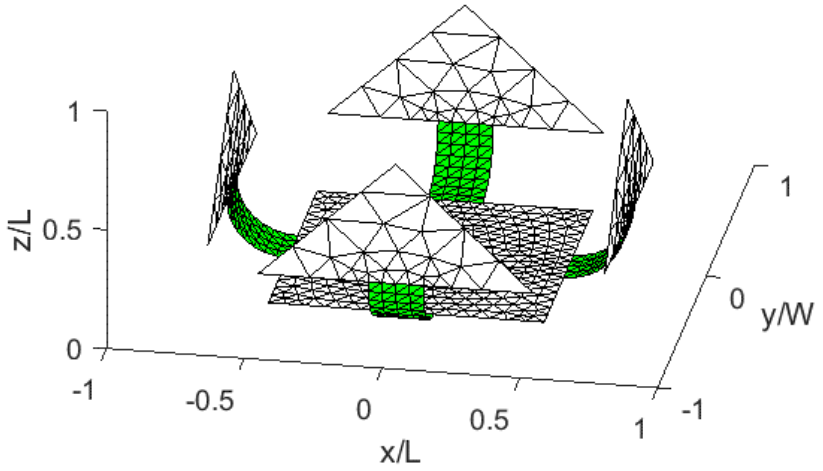

(a)

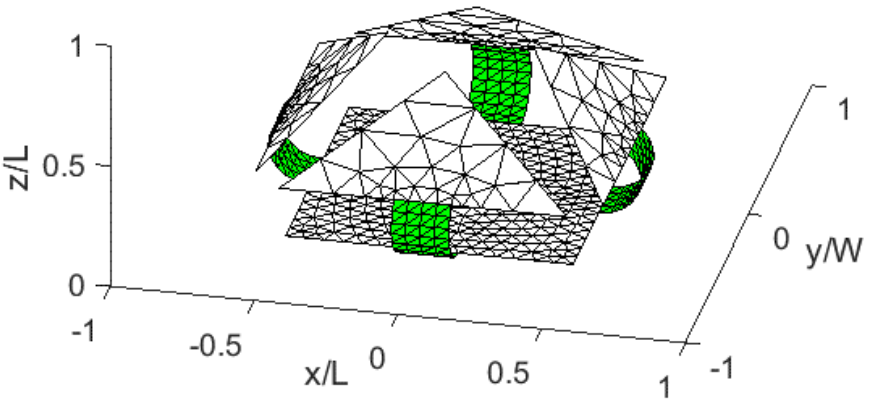

(b)

Figure 4.7. Configuration of the smart viscoelastic shell under actuation of four pairs of AFC patches at (a) T=0.1 sec and (b) T=1 sec

In next two examples, twisting configurations of two smart viscoelastic plate after *T*=0.1 sec and 1sec with two pairs of quadrilateral-shape patches stimulated in the same directions (Figure 4.8) and opposite directions (Figure 4.9) are shown from different view angles.

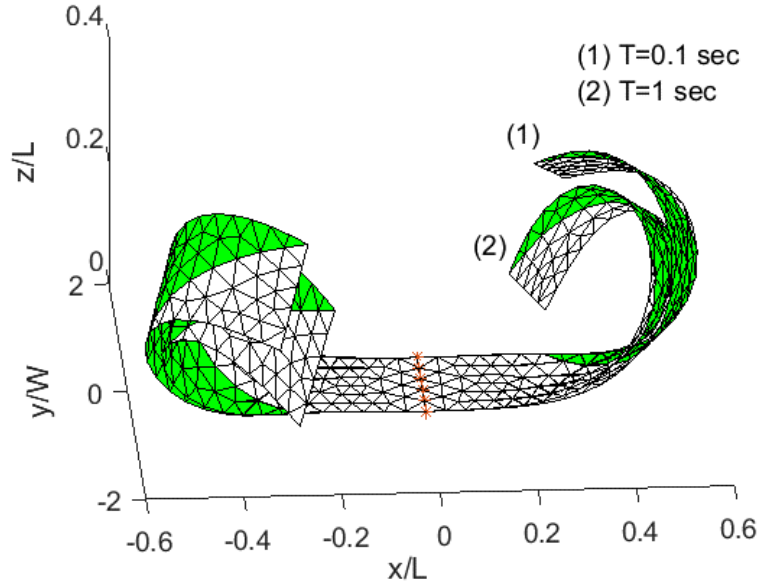

(a)

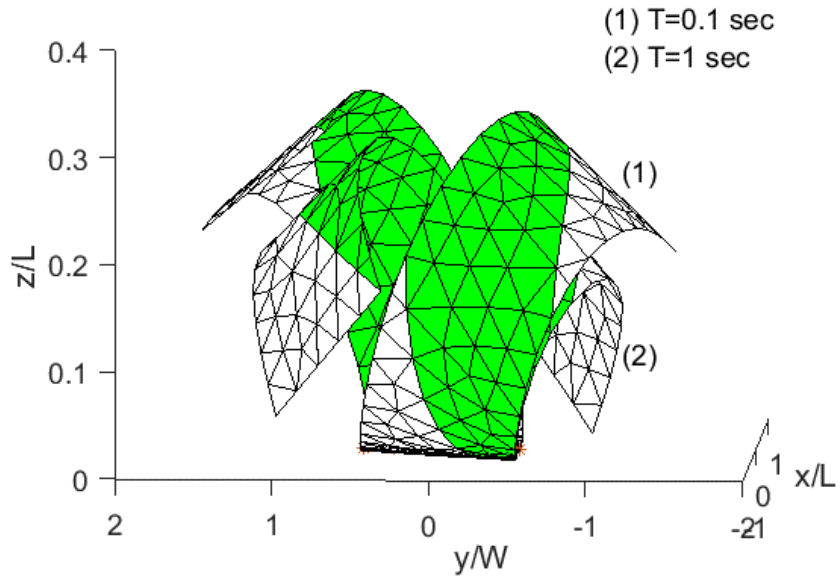

(b)

Figure 4.8. Configuration of the smart viscoelastic shell under actuation of two pairs of AFC patches at T=0.1 sec and 1 sec form two view angles (a,b)

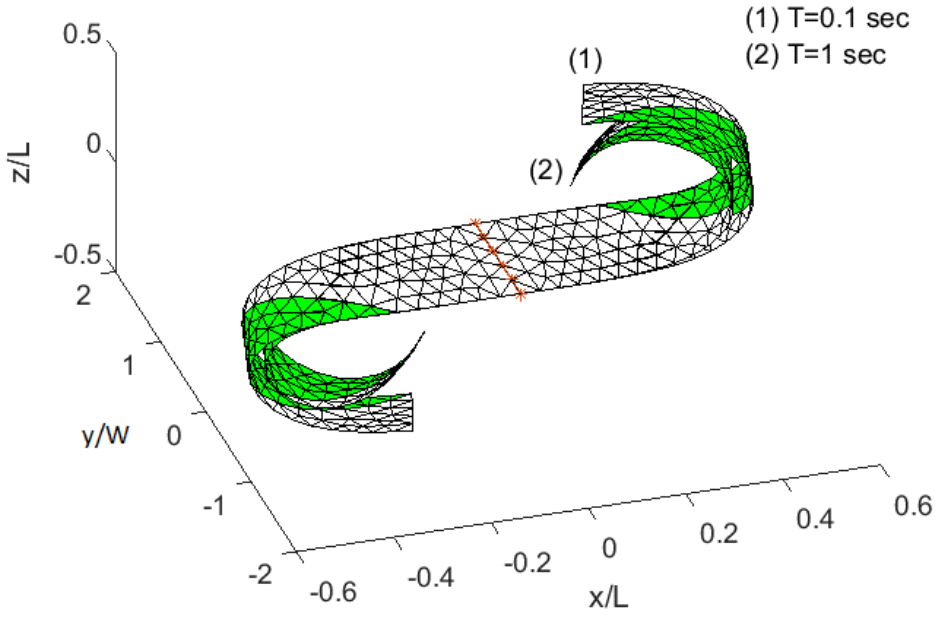

(a)

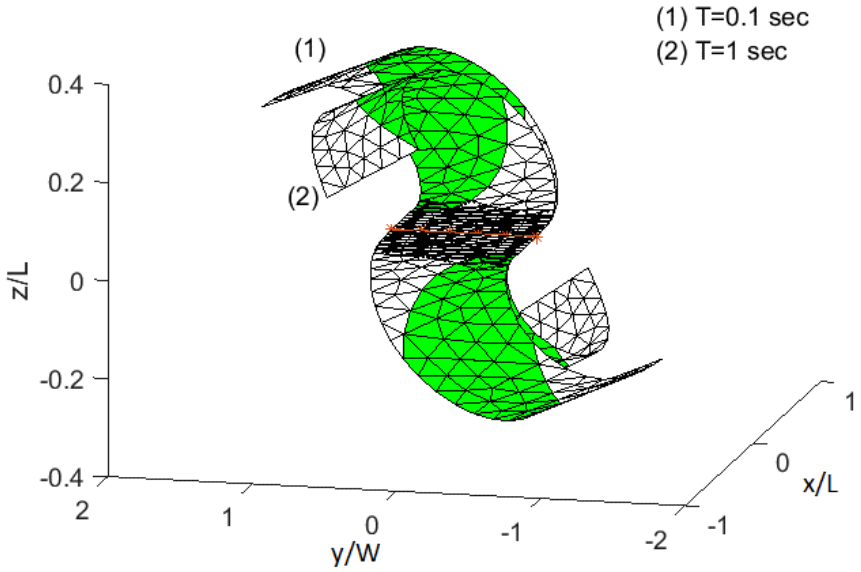

(b)

Figure 4.9. Configuration of the smart viscoelastic shell under actuation of two pairs of AFC patches in opposite directions at T=0.1 sec and 1 sec form two view angles (a,b)

In next analysis, the substrate is assumed to be elastic; Figure 4.10 shows configuration of a smart shell consisting of an elastic substrate actuated by one pair of AFC patches. For the electric field input $E_m^e = 0.5\,\mathrm{MV/m}$ and $t_r = 0.02\,\mathrm{sec}$. As seen the deformation increases relatively fast at early time due to manly an increase of electric stimulus magnitude and then increases slowly over time because of the viscoelastic effect of the actuator related to increase of the piezoelectric coefficients of the actuator.

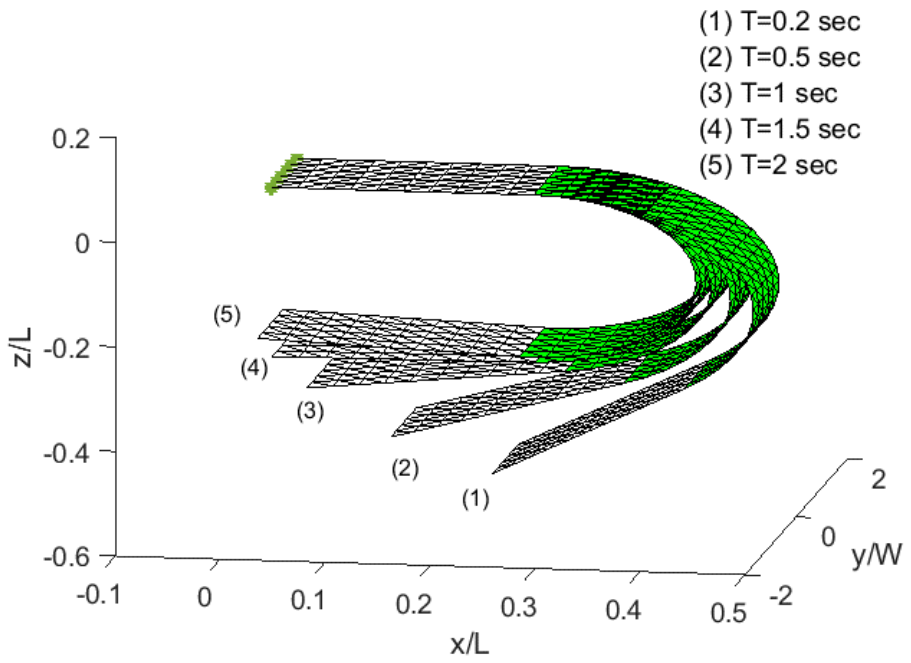

Figure 4.10. Configuration of the smart elastic shell under actuation of one pair of AFC patches at different actuation time, *T*

5. CONCLUSION

5-1 Summary of the work

In this research, structural analyses of flexible elements including beams, plates and shells under electro-mechanical actuations have been studied. The structures are undergoing large deformations, mainly due to large rotation, but strains remains relatively small under electric field actuation. Multiple piezoelectric patches attached on top and bottom surfaces of the substrate structure, symmetrical with respect to middle of the substrate in thickness direction, have been considered. By applying electric voltage, the patches were stimulated and consequently the substrate was actuated based on calculated interaction between the patch and the substrate. The calculation of the induced load from the actuated patches to the substrate was performed based on perfect bonding of patches to the substrate so that the stresses transmitted to the substrate almost along the edges of the patch. Large deformations like folding were desired for actuated structure which demands relatively large electric field stimulus. Therefore, nonlinear electro-mechanical coupling effects were considered for the behavior of the active piezoelectric patches. The thickness of the patch was considered much smaller than the thickness of the substrate to that extent that the structure can be assumed reasonably with uniform thickness equal to the thickness of the substrate. The nonlinear electro-mechanical constitutive model can also be used for other type electro-active materials such as electrostrictive materials, in which the even terms in the higher order electric field variables are considered.

For cantilever smart beams under the application of electric actuation, the governing equations based on the Reissner's theory were successfully solved analytically. On the other hand, under electro-mechanical actuation, 4^{th} –order Runge-Kutta method was used for modeling deformation of the actuated beam.

For numerical simulation of the structural response of smart plates and shells, co-rotational Lagrangian approach was adopted. This approach was especially beneficial for analyses dealing with small strain but large rotations and nonlinear geometry is mostly related to the rigid body rotations and translations. Incremental iterative process with

Newton-Raphson algorithm was used for the nonlinear analysis. At each incremental time step, linear finite element analysis was used to calculate the trial small deformational rotations and translations of each element of the discretized domain of the structure, and then by using some purely geometrical translation and rotation tensors and coordinate transformations, rigid body deformations and therefore the total large displacements of the structure were determined.

Polymers are common materials for manufacturing flexible foldable structures which may show time-dependent behavior; therefore, other than elastic analysis, viscoelastic analysis was also performed to count stress relaxation in the actuated polymeric structure over time. The viscoelastic characteristic was considered also for the AFCs actuator. AFCs with polymeric matrix have higher toughness and easier to use as actuators for reconfiguration of foldable structures. Thus, it is important to also consider time-dependent behavior of AFC patches which influence the shape changes in the foldable systems.

Through various simulations for elastic and viscoelastic beams and shells, different reconfigurations of the actuated structures have been presented. Three types of simulations were performed including elastic patches with elastic substrate, elastic patches with viscoelastic substrate and viscoelastic patches with viscoelastic substrate.

It was seen that stiffness of substrate does have notable effect on amount of deformation of the actuated structure as the change in rigidity of the structure neutralized by the change in induced load by the piezoelectric patches perfectly bonded to the substrate. Therefore, for instance, for viscoelastic substrate with elastic patches under constant stimulus, although relaxation function of the substrate decreases over time, reduction of induced moment prevents further deformation of the structure. This can gives elastic piezoelectric actuators advantage over viscoelastic actuators in applications where time-dependent deformation is undesirable.

Moreover, by manipulating some parameters such as locations and sizes of the patches and magnitude of electric stimulus, some interesting configuration with practical application were presented such as U-shape configuration promising for manufacturing soft robotic grippers, morphing shape change of wings of micro air vehicles and self folding of a box useful for packaging.

5-2 Future works

1- Taking into account large strains by modifying CRFE or using another method like updated Lagrangian FE method to analyze smart foldable structures to extend the application of the presented work to large strain situations where applied loads are much larger than one considered and/or other types of loads exist which may lead to other types of deformation, for example, large stretch.

2- Considering thermal loads and also performing viscoelastic analysis for different temperatures as temperature plays a significant role on the viscoelastic response of polymers, and flexible smart structures may be subjected to variation of temperatures in practical applications.

3- Omitting the assumption of patches being perfectly bonded which affects analysis of traction and induced loads between the piezoelectric patch and the substrate so that more realistic conditions are taken into account due to possible existing manufacturing defects.

4- Considering problems with the piezoelectric actuators are embedded inside the structure rather than only attached on its surface. Because in some cases, the actuators in shape of fibers or particles can also be used for reinforcing the structure stiffness similar to the AFC patches with piezoelectric fibers inside polymeric matrix. Also, manufacturing very thin patches to be bonded on surface of a thin flexible structure is difficult. Besides, foldable structures with surface bonded actuators with notable thickness compared to substrate thickness should be analyzed.

5- Performing parametric study in more depth for numbers, geometries and locations of distributed patches and electric field magnitude to establish a systematic way of predicting desired configurations for the actuated structures.

6- Considering energy dissipation and hysteresis of the piezoelectric material in the analysis to extend the feasibility of the work when for example the smart structure is subjected to periodic electric stimulus versus time. This can be done to assess the life performance of such foldable/flexible structures actuated by electric field inputs.

REFERENCES

[1] M. Santer and S. Pellegrino, *Topological optimization of compliant adaptive wing structure.* AIAA Journal, 2009. **47**: p. 523-534.

[2] K.W. Moored, T.H. Kemp and N. E. Houle, *Analytical predictions, optimization, and design of a tensegrity-based artificial pectoral fin.* International Journal of Solids and Structures, 2011. **48**(22): p. 3142–3159

[3] T. Yokozeki, Sh. Takeda, T. Ogasawara and T. Ishikawa, *Mechanical properties of corrugated composites for candidate materials of flexible wing structures.* Composites Part A: applied science and manufacturing, 2006. **37**(10): p. 1578-1586.

[4] S.L. dos Santos e Lucato, J. Wang, R. M. McMeeking and A. G. Evans, *Design and demonstartion of a high authority shape morphing structure.* International journal of Solids and Structures, 2004. **41**: p. 3521-3543.

[5] S. Kota, J.A. Hetrick, R. Osborn, D. Paul, E. Pendleton, P. Flick, and C. Tilmann. *Design and application of compliant mechanisms for morphing aircraft structures*. in *Proceedings of SPIE - The International Society for Optical Engineering*. 2003.

[6] G. Lanzara, J. Feng and F-K. Chang, *Design of micro-scaled highly expandable networks of polymer based substrates for macro-scale applications.* Smart Materials and Structures, 2010. **19**(4).

[7] E.J. Kramer, C.J. Hawker and M.L. Chabinyc, *Interdiffusion of PCBM and P3HT reveals miscibility in a photovoltaically active blend.* Advanced Energy Materials, 2011. **1**: p. 82-89.

[8] A.A. Bent and N.W. Hagood, *Piezoelectric fiber composites with interdigitated electrodes.* Journal of Intelligent Material Systems and Structures, 1997. **8**(11): p. 903-919.

[9] P.M. Naghdi and L. Vongsarnpigoon, *A theory of shells with small strain accompanied by moderate rotation.* Archive for Rational Mechanics and Analysis, 1983. **83**: p. 245-283.

[10] A.R Srinivasa, *On a class of Gibbs potential-based nonlinear elastic models with small strain.* Acta Mechanica, 2015. **226**: p. 571-583.

[11] D.G. Fertis, *Nonlinear structural engineering*. 2006: Springer.

[12] C. Kimball and L.-W. Tsai, *Modeling of flexible beams subjected to arbitrary end loads.* ASME Journal of Mechanical Design, 2002. **124**: p. 223-234

[13] L.L. Howell and A. Midha, *Parametric deflection approximations for end-loaded large deflection beams in compliant mechanisms.* ASME Journal of Mechanical Design, 1995. **117**: p. 156-165.

[14] Y. Tada and G. Lee, *Finite element solution of elastic problem of beams.* International Journal of Numerical Methods and Engineering, 1970. **2**: p. 229.

[15] T.Y. Yang, *Matrix displacement solution of elastica problems of beams.* International Journal of Solids and Structures, 1973. **9**: p. 829.

[16] A. Chajes, *Nonlinear frame analysis by finite element methods.* ASME Journal of Structural Engineering, 1987. **6**.

[17] E. Reissner, *On one-dimensional finite strain beam theory: the plane problem.* Journal of Applied Mathematics and Physics, 1972. **23**: p. 795- 804.

[18] H. Irschik and J. Gerstmayr, *A continuum mechanics based derivation of Reissner's large-displacement finite-strain beam theory: the case of plane deformations of originally straight Bernoulli-Euler beams.* Acta Mechanica, 2009. **206**: p. 1-21

[19] B.J. de Blonk and D.C. Lagoudas, *Actuation of elastomeric rods with embedded two-way shape memory alloy actuators.* Smart Materials and Structures, 1997. **7**: p. 771-783.

[20] I.G. Tadjbakhsh and D.C. Lagoudas, *Actuation of elastomeric rods with embedded two-way shape memory alloy actuators.* Smart Materials and Structures, 1993. **2**: p. 71-81.

[21] S.G. Shu, D.C. Lagoudas, D. Hughes and J. T. Wen, *Modeling of a flexible beam actuated by shape memory alloy wires.* Smart Materials and Structures, 1997. **6**: p. 265-277.

[22] A. Banerjee, B. Bhattacharya and A.K. Mallik, *Large deformation of cantilever beams with geometric non-linearity: Analytical and numerical approaches.* International Journal of Non-Linear Mechanics, 2008. **43**: p. 366-376.

[23] Ch.-F. Chen and J.-H. Chen, *Nonlinear study of large deflection of simply supported piezoelectric layered-plate under initial tension.* International Journal of Mechanical Sciences, 2011. **53**: p. 485-493.

[24] C.X. Xue, E. Pan, S.Y. Zhang and H.J. Chu, *Large deflection of a rectangular magnetoelectroelastic thin plate.* Mechanics Research Communications, 2011. **38**: p. 518-523.

[25] K. Jayakumar, D. Yadav and B.N. Rao, *Moderately large deflection analysis of simply supported piezo-laminated composite plates under uniformly distributed transverse load.* International Journal of Non-Linear Mechanics, 2013. **49**: p. 137-144.

[26] G.A. Wempner, *Finite elements, finite rotations and small strains of flexible shells.* International journal of solid structures, 1969. **5**: p. 117-153.

[27] T. Belytschko and B.J. Hsieh, *Non -linear transient finite element analysis with convected co-ordinates.* International journal of numerical methods in engineering, 1973. **7**: p. 255-271.

[28] B.M. Fraeijs de Veubeke, *The dynamics of flexible bodies.* International journal of engineering and science, 1976: p. 895-913.

[29] P.G . Bergan and G. Horrigmoe, *Incremental variational principles and finite element models for nonlinear problems.* Computational methods in applied mechanics, 1976. **7**: p. 201-217.

[30] J.H. Argyris, *An excursion into large rotations.* Computational methods in applied mechanics, 1985. **32**: p. 85-155.

[31] C.C. Rankin and F.A. Brogan, *An element-independent corotational procedure for the treatment of large rotations.* ASME journal of pressure vessel technology, 1986. **108**: p. 165-174.

[32] B . Nour-Omid and C.C. Rankin *Finite rotation analysis and consistent linearization using projectors.* Computational methods in applied mechanics, 1991. **93**: p. 353-384.

[33] A. Cardona, *An integrated approach to mechanism analysis,*. 1989, University of Liege Belgium.

[34] M.A. Crisfield, *A consistent corotational formulation for nonlinear three-dimensional beam element.* Computational methods in applied mechanics, 1990. **81**: p. 131-150.

[35] M.A. Crisfield, *Nonlinear Finite Element Analysis of Solids and Structures, Vol. 2, Advanced Topics*. 1997, Chichester: Wiley.

[36] M.A. Crisfield and G.F. Moita, *A unified co-rotational for solids, shells and beams.* International journal of solid structures, 1996. **33**: p. 2969-2992.

[37] C.A. Felippa and B.A. Hagen, *A unified formulation of small-strain corotational finite elements: I. Theory.* Computational methods in applied mechanics and Engineering, 2005. **194**: p. 2285-2335.

[38] S.B. Cai, P.S. Shen and B.X. Hu, *A field consistency based co-rotational finite element procedure for 2D quadrilateral element.* Engineering mechanics, 2009. **26**: p. 31-34.

[39] Z.X. Li, B.A. Izzuddin and L. Vu-Quo, *A 9-node co-rotational quadrilateral shell element.* Computational mechanics, 2008. **42**: p. 873-884.

[40] F.S. Almeida and A.M. Awrunch, *Corotational nonlinear dynamic analysis of laminated composite shells.* Finite Elements Analysis Design, 2011. **47**: p. 1131-1145.

[41] X.M. An and M. Xu, *An improved geometrically nonlinear algorithm and its application for nonlinear aeroelasticity.* Chinese journal of theoretical applied mechanics, 2011. **43**: p. 97-104.

[42] Y. JinSong and X. PinQi, *Finte element corotational formulation for geometric nonlinear analysis of thin shells with large rotation and small strain.* Science China, 2012. **55**: p. 3142-3152.

[43] Y.C. Cai, J.K. Paik and S.N. Atluri, *A triangular plate element with drilling degrees of freedom, for large rotation analyses of built-up plate/shell structures, based on the Reissner variational principle and the von Karman nonlinear theory in the co-rotational reference frame.* CMES: Computer modeling in engineering $ sciences, 2010. **61**: p. 273-312.

[44] Y.C. Cai and S.N. Atluri, *Large rotation analyses of plate/shell structures based on the primal variational principle and a fully nonlinear theory in the updated Lagrangian co-*

rotational reference frame. CMES: Computer modeling in engineering & sciences, 2012. **83**: p. 249-273.

[45] H.F. Tiersten, *Electroelastic equations for electroded thin plates subject to large driving voltages* Journal of Applied Physics 1993. **74**(5): p. 3389 - 3393.

[46] A. Muliana and Ch.-H. Lin, *A Multi-scale Formulation for Predicting Non-linear Thermo-electro-mechanical Response in Heterogeneous Bodies.* Journal of Intelligent Material Systems and Structures, 2011. **22**: p. 723-738.

[47] P. Tan and L. Tong, *Micro-electromechanics models for piezoelectric-fiber-reinforced composite materials.* Composites Science and Technology, 2001. **61**(5): p. 759-769.

[48] V. Tajeddini, Ch.H. Lin, A.H. Muliana and M. Levesque, *Average electro-mechanical properties and responses of active composites.* Computational Materials Science, 2014. **82**: p. 405-414.

[49] A.S. Mollayousef, *Nonlinear and rate dependent hysteresis electromechanical responses of ferro electric materials*. 2015, Texas A&M University.

[50] A.J. Brunner, B.M. Huber and P.H. Flüeler, *The potential of active fiber composites made from piezoelectric fibers for actuating and sensing applications in structural health monitoring.* Journal of Materials and Structures, 2005. **38**: p. 561-567.

[51] Smart Material Corporation. Available from: http://www.smart-material.com/13CompOverview.html.

[52] A.A. Bent, *Active fiber composites for structural actuation*. 1997, MIT.

[53] R. Gentilman, K. McNeal and G. Schmidt, *Enhanced performance active fiber composites.* Smart Structures and Materials 2003. **5054**.

[54] H.B. Atitallah, *Characterization and modeling of active fiber composites*. 2014, Pennsylvania State University.

[55] H.B. Atitallah, Z. Ounaies and A.H. Muliana, *Temperature and time dependence of the electro-mechanical properties of flexible active fiber composites.* Smart Materials and Structures, 2016.

[56] V. Tajeddini, H.B. Atitallah, A. Muliana and Z. Ounaies, *Nonlinear viscoelastic behavior of active fiber composites.* Journal of Engineering Materials and Technology, 2014. **136**(2).

[57] Sh. Ya-peng, P. Ya-fei., *Stress and fracture analyses of viscoelastic large strain plane problem by finite element method*, in *Proceeding of the international conference on nonlinear mechanics*. 1985: Shanghai. p. 1301-1306.

[58] J.T. Holden, *On the finite deflection of thin viscoelastic beams.* International Journal of Numerical methods in engineering, 1972. **5**: p. 271-275.

[59] V.A. Baranenko, *Large displacements of viscoelastic beams.* Mechanics of Composite Materials, 1980. **15**: p. 681-684.

[60] K. Lee, *Large deformation of visocelastic fiber beams.* Textile Research Journal, 2007. **77**: p. 47-51.

[61] M.A. Vaz and M. Caire, *On the large deflections of linear viscoelastic beams.* International Journal of Non-linear Mechanics, 2010. **45**: p. 75-81.

[62] N.N. Huang, *Viscoelastic analysis of von Karman laminated plates under in-plane compression with initial deflection.* International Journal of Non-linear Mechanics, 1997. **32**: p. 1065-1075.

[63] D. Touati and G. Cederbaum, *Postbuckling of non-linear viscoelastic imperfect laminated plates. part II: structural analysis.* Composite Structures, 1998. **42**: p. 43-51.

[64] D.C. Hammerand, *Geometrically-linear and nonlinear analysis of linear viscoelastic composites using the finite element method*. 1999, VIRGINIA POLYTECHNIC INSTITUTE AND STATE UNIVERSITY.

[65] C.E. Beldica and H.H. Hilton, *Nonlinear viscoelastic beam bending with piezoelectric control-Analytical and experimental simulations.* Composite Structures, 2001. **51**: p. 195-203.

[66] A. Muliana, *Large deformations of nonlinear viscoelastic and multi-responsive beams.* International Journal of Non-Linear Mechanics, 2015. **71**: p. 152-164.

[67] V. Tajeddini and A. Muliana, *Nonlinear deformations of piezoelectric composite beams.* Composite Structures, 2015. **132**: p. 1085-1093.

[68] J. Yang and P. Zhang, *Nonlinear bending of piezoelectric cylindrical shell reinforced with BNNTs under electro-thermo-mechanical Loadings.* Materials Sciences and Applications, 2015. **6**: p. 743-752.

[69] E.F. Crawley and J. de Luis, *Use of piezoelectric actuators as elements of intelligent structures.* AIAA Journal, 1987. **25**: p. 1373-1385.

[70] E.K. Dimitriadis and C.R. Fuller, *Investigation on active control of sound transmission through elastic plates using piezoelectric actuators.* AIAA Journal, 1989: p. 89-1062.

[71] B.-T. Wang, E.K. Dimitriadis and C.R. Fuller. *Active control of structurally radiated noise using multiple piezoelectric actuators*. in *AIAA/ASME/ASCE/AHS 31st Structures, Structural Dynamics and Materials Conference*. 1990. Long Beach, CA.

[72] S. Im and S.N. Atluri, *Effect of a piezo-actuator on a finitely deformed beam subjected to general loading.* AIAA Journal, 1989. **27**(12): p. 1801-1807.

[73] B.-T. Wang and C.A. Rogers, *Laminate plate theory for spatially distributed induced strain actuators.* Journal of Composite Materials, 1991. **25**: p. 433-452.

[74] E.K. Dimitriadis, C.R. Fuller and C.A. Rogers, *Piezoelectric actuators for distributed noise and vibration excitation of thin plates.* Journal of Vibrations and Acoustics, 1991. **113**: p. 100-107.

[75] J.L. Batoz, K.J. Bathe and L.W. Ho, *A study of three-node triangular plate bending elements.* International journal of numerical methods in engineering, 1980. **15**: p. 1771-1812.

[76] C.A. Felippa, *A study of optimal membrane triangles with drilling freedoms.* Computational methods in applied mechanics and Engineering, 2003. **192**: p. 2125-2168.

[77] P. Mohan, *Development and application of a flat triangular element for thin laminated shells* in *Aerospace Engineering*. 1997, Virgina Polytechnic Institute and State University: Blacksburg, Virginia.

[78] C.A. Felippa and C. Militello, *Membrane triangles with corner drilling freedoms. II. The ANDES element,.* Finite elements analysis and Design, 1992. **12**: p. 189-201.

[79] P.G. Bergan and C.A. Felippa, *A triangular membrane element with rotational degrees of freedom.* Computer methods in applied mechanics and engineering, 1985. **50**: p. 25-69.

[80] K.A. Khan, A. H. Muliana, H.B. Atitallah and Z. Ounaies, *Time-dependent and energy dissipation effects on the electro-mechanical response of PZTs.* Under preparation, 2016.

[81] Y.C. Fung, *Biomechanics: Mechancial properties of living tissues.* 1981, New York: Springe.

[82] H.B. Atitallah, Z. Ounaies and A. Muliana, *A parametric study on flexible electro-active composites: Importance of geometry and matrix properties.* Journal of Intelligent Material Systems and Structures, 2014.

[83] M.A. Zocher, E. Groves and D.H. Allen, *A three-dimensional finite element formulation for thermoviscoelastic orthotropic media.* International Journal for Numerical Methods in Engineering, 1997. **40**: p. 2267-2288.